NSK Technical Journal

Motion & Control

No. 31 June 2020

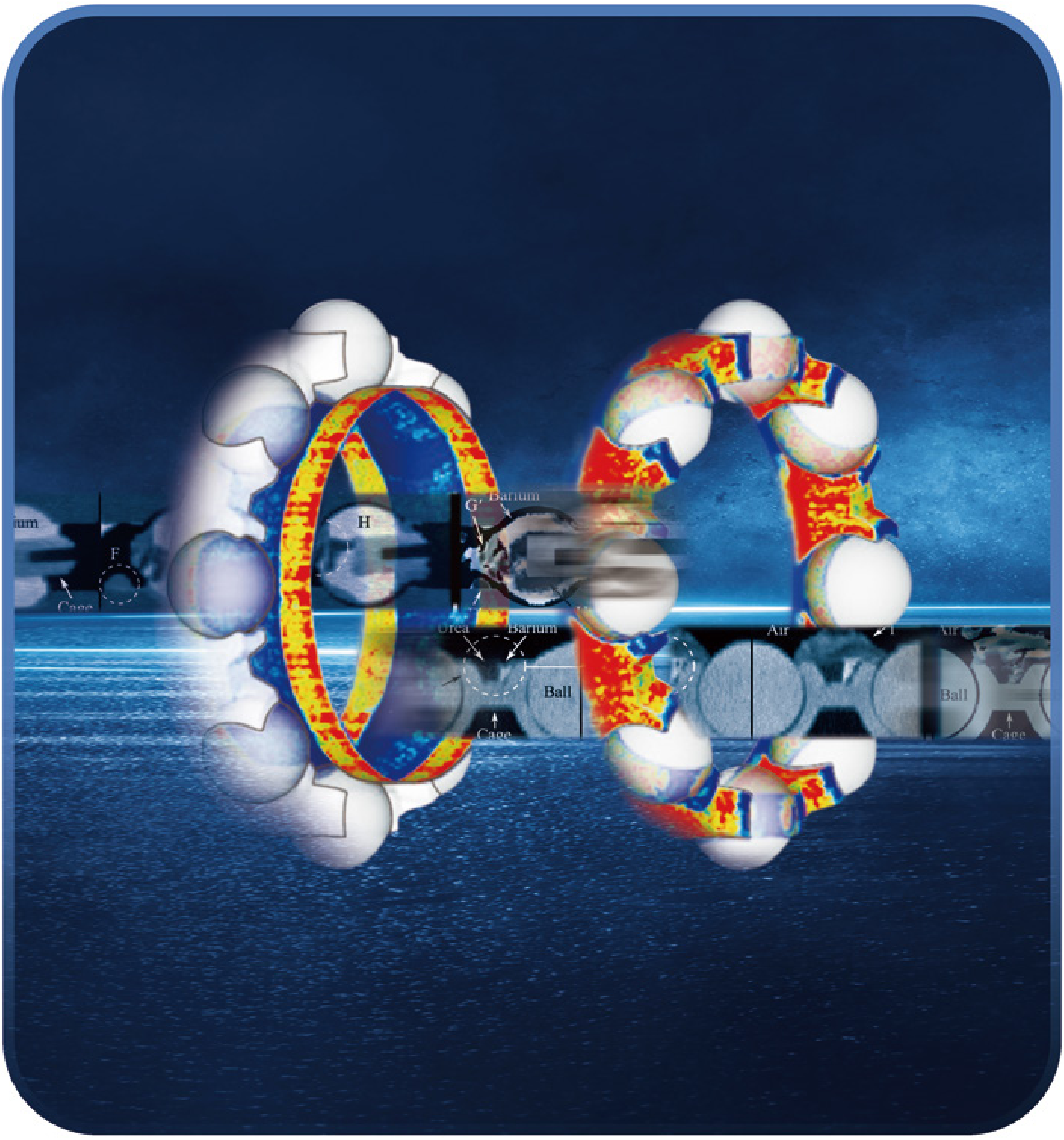

ISSN1342-3630

MOTION & CONTROL No. 31
NSK Technical Journal
Printed and Published: June 2020
ISSN1342-3630
Publisher: NSK Ltd., Ohsaki, Shinagawa, Tokyo, JAPAN
Public Relations Department
TEL +81-3-3779-7050
FAX +81-3-3779-7431
Editor: Nobuo GOTO
Managing Editor: Aya OKAMOTO
Design, Typesetting & Printing: Kuge Printing Co., Ltd.

NSK Technical Journal

Motion & Control

No. 31

June 2020

NSK

Contents

Technical Papers

New Products

Development of NSK LCube II™ Tapered Roller Bearings for Electric-Hybrid Vehicles

Masaki Chishima
Automotive Technology Development Center, Automotive Powertrain Bearing Technology Center, Powertrain Bearing Technology Department

Abstract

In line with increasing concern for the environment, consumers and businesses around the world demand better fuel economy from motor vehicles, which is leading to the rapid development of electric/hybrid vehicles.

In the field of gearboxes for these vehicles, development of low viscosity lubricant oil is required to reduce energy consumption.

As a result, requirements for tapered roller bearings used in gearboxes have become increasingly severe and countermeasures for surface damage and seizure in severe lubrication environments have become an important area of focus.

In the following article, we introduce NSK's LCube II tapered roller bearing (TRB), which has reduced surface damage in severe lubrication environments and improved seizure resistance.

NSK LCube II TRBs have eight times the durability and comparable seizure resistance of a conventional TRB in severe lubrication environments. Additionally, NSK LCube II TRBs have 10% reduced friction losses when compared to a conventional TRB under low speeds.

1. Introduction

The tightening of environmental regulations and depletion of fossil fuels in recent years have driven the need to boost the fuel efficiency of automobiles globally, thus accelerating the development of electric/hybrid vehicles.

In the gearboxes for these vehicles, the viscosity of the lubricant is being reduced to minimize unit losses in order to improve fuel efficiency and power consumption. As a result, the lubricated environments of tapered roller bearings used in the gearboxes are becoming harsher. Moreover, preventing surface damage and the seizure of bearings due to insufficient oil film has become a key issue in creating a highly reliable gearbox.

As automakers accelerate development of electric/hybrid vehicles, the solution of achieving gearbox efficiency will require the development of robust bearings. NSK has developed the NSK LCube as a technology for coping with surface damage and seizure caused by insufficient oil film of tappet rollers for automotive engines1), and this has contributed to improving engine reliability. This paper introduces the NSK LCube II, a developed product which is an improved and optimized version of LCube technology for tapered roller bearings.

2. Effects and Challenges of Bearings Due to Changes in Usage Environments

NSK has developed a variety of low-friction tapered roller bearings to contribute to improving gearbox efficiency2).

Aihara has reported the theory of the frictional resistance of tapered roller bearings3), and the contributing factors of tapered roller bearing friction can be classified into (1) to (4), as shown in Figures 1 and 2.

(1) Rolling friction between the inner and outer ring raceway surfaces and rolling element surfaces
(2) Sliding friction between the inner ring rib and roller end face
(3) Sliding friction between the roller and cage
(4) Agitation friction of the lubricant

Among these, (1) rolling friction between the inner and outer ring raceway surfaces and rolling element surfaces, (2) sliding friction between the inner ring rib and roller end face, and (4) agitation friction of the lubricant account for the majority of the friction in tapered roller bearings. NSK has developed and marketed various types of low-friction tapered roller bearings with the aim of reducing friction from these factors.

On the other hand, due to vehicle electrification, the viscosity of lubricants in the gearboxes has been significantly lowered in order to reduce agitation friction in recent years. As a result, bearings are exposed to severe lubrication environments and increased propensity for surface damage of the rolling contact portion and seizure of the sliding contact portion.

Achievement of both higher gearbox efficiencies with low-friction tapered roller bearings and the prevention of premature bearing failure requires the development of low-friction, robust bearings.

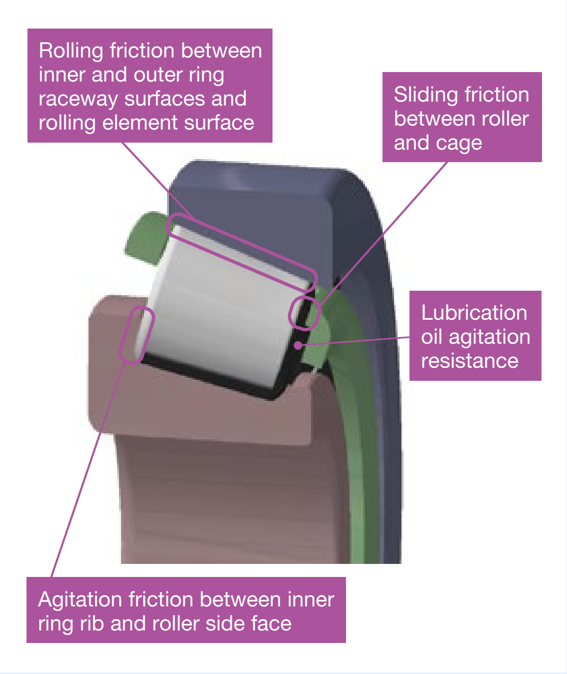

Fig. 1 Friction factors in a tapered roller bearing

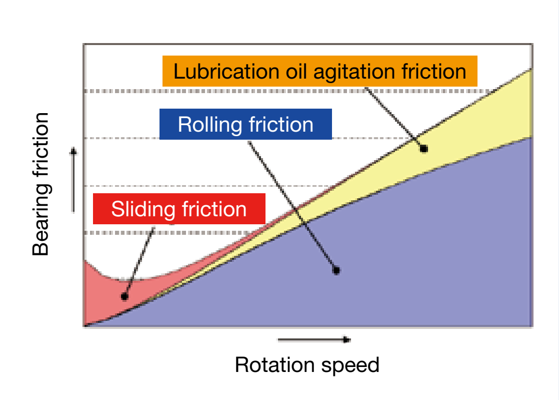

Fig. 2 Relationship between rolling and sliding friction

3. Characteristics and Effects of Developed Products

NSK's high durability tappet roller, the LCube series, can be applied to the surfaces of various mating components as a response to the harsh diluted lubrication environments of engine valve systems in order to achieve higher reliability.

The newly developed tapered roller bearings, LCube II, introduced in this paper further utilize the processing technologies cultivated in the LCube series for gearboxes with harsher lubricated environments. Their characteristics and effects are described below.

3.1 Formation of oil reservoirs

As shown in Figure 3, a great number of large and deep oil reservoirs are formed on the tappet roller outer ring surfaces through special machining, and lubricant is retained in the oil reservoir to prevent an insufficient oil film. The properties of the oil reservoir are optimized so that it can be applied to various materials, heat treatments, and surface finishing conditions on the mating surface.

Figure 4 shows examples of tapered roller bearing damage in under-lubricated environments. Due to sliding contact between the inner ring rib and roller end face, tapered roller bearings have a risk of seizure and the friction in this region is dependent on the operating environment and surface features as shown in Item 2. In the development process, a prototype comparable with LCube was produced and tested.

As a result, an improvement in durability in relation to surface damage was observed; however, an increase in friction at low speeds was also observed (Figure 5). The large and deep oil reservoirs processed using LCube special machining (Figure 3) were optimized for tappet rollers, as previously described. This same process, when applied to the sliding contact portion in case of tapered roller bearings, may result in an increase in friction.

In light of this phenomenon, the newly developed LCube II forms a number of shallow and small oil reservoirs (Figure 6) and improves the processing method, making it suitable for tapered roller bearings. As a result, we have established an optimized surface feature for tapered roller bearings, which both suppresses the increase in sliding friction by improving the surface roughness and further reduces rolling friction due to the oil reservoir effect.

In order to confirm the effects of the application of LCube II on the functions of bearings, we conducted tests on the durability to surface damage, seizure resistance to sliding friction, and the effect on friction.

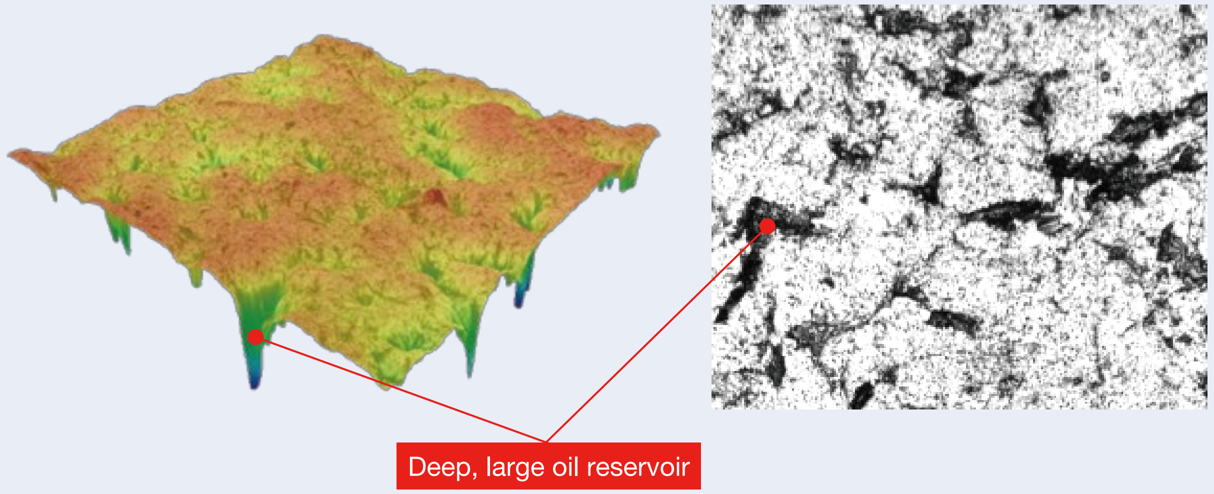

Fig. 3 NSK LCube™ 3D surface and enlarged surface photograph

Seizure examples on roller head/inner ring rib surfaces

Surface damage examples for roller rolling surface (peeling)

Fig. 4 Surface damage on the tapered roller bearing

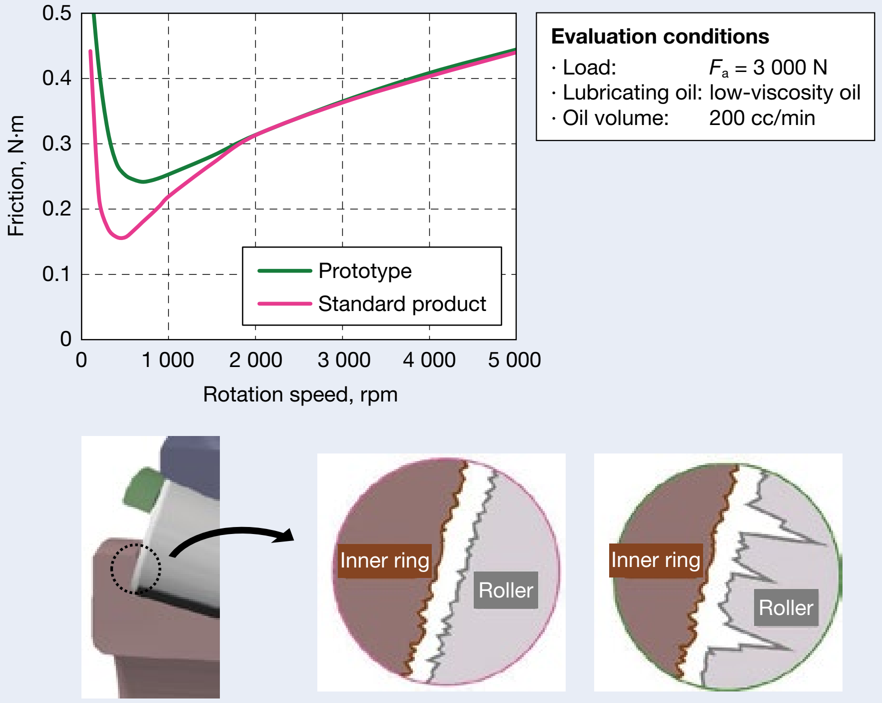

Fig. 5 Bearing friction measurement results for the test product

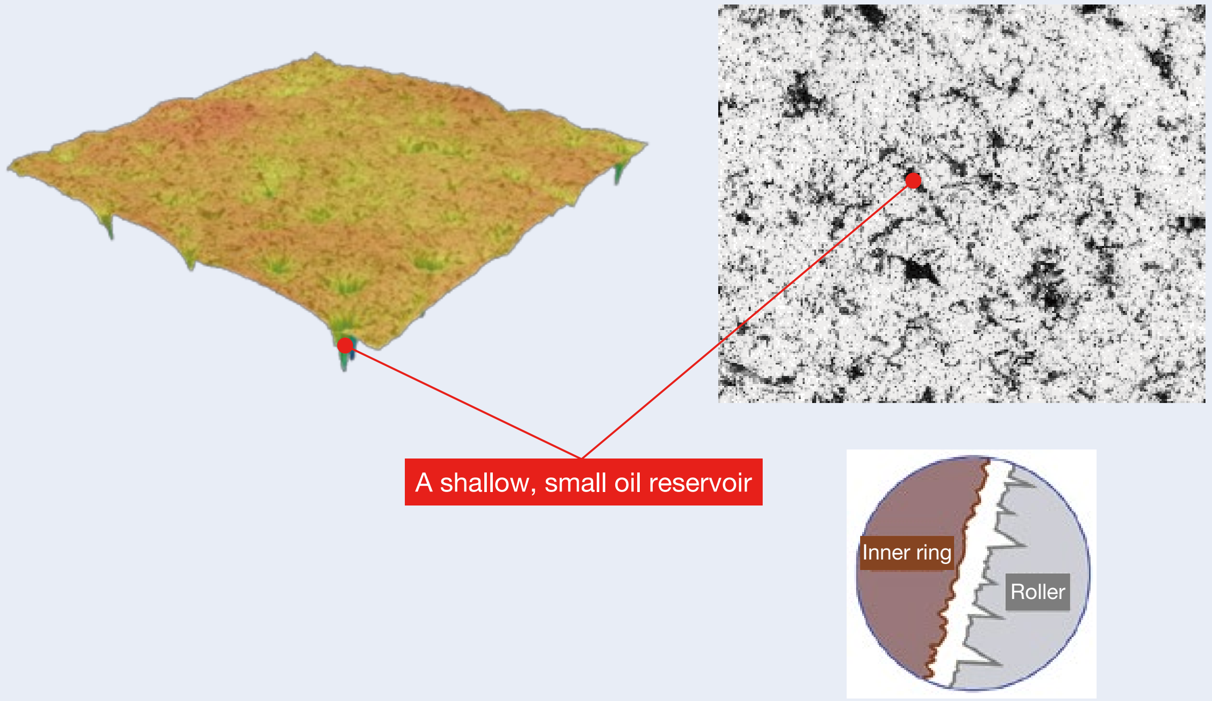

Fig. 6 NSK LCube II™ 3D surface and enlarged surface photograph

3.2 Surface damage resistance

The hardness of the outermost layer of LCube II can be increased by the effects of a special processing optimized for the tapered roller (about 1.2 times that of the standard tapered roller).

Figure 7 shows the results of a durability test conducted under diluted lubrication and low-viscosity oil conditions in order to confirm the effects of minute oil reservoirs on the roller rolling surfaces and the effects on surface damage. The evaluation results show that LCube II has achieved improved durability resulting in a life more than eight times longer in terms of surface damage when compared to the standard product.

Figure 8 shows the appearance of the tapered roller rolling surface before and after the test, confirming that the surface of the standard product is rough due to continued use in severe operating environments, and a small amount of flaking (peeling) occurred. The test also confirmed that LCube II retains the surface feature evidenced by oil reservoirs remaining post-test. Even at eight times the test duration, oil reservoirs still remained and no progression of surface damage occurred although the surfaces were rough due to the harsh conditions. This indicates that the hardness improvement effect of the outermost layer and the oil film retention effect due to the oil reservoir are effective against surface damage.

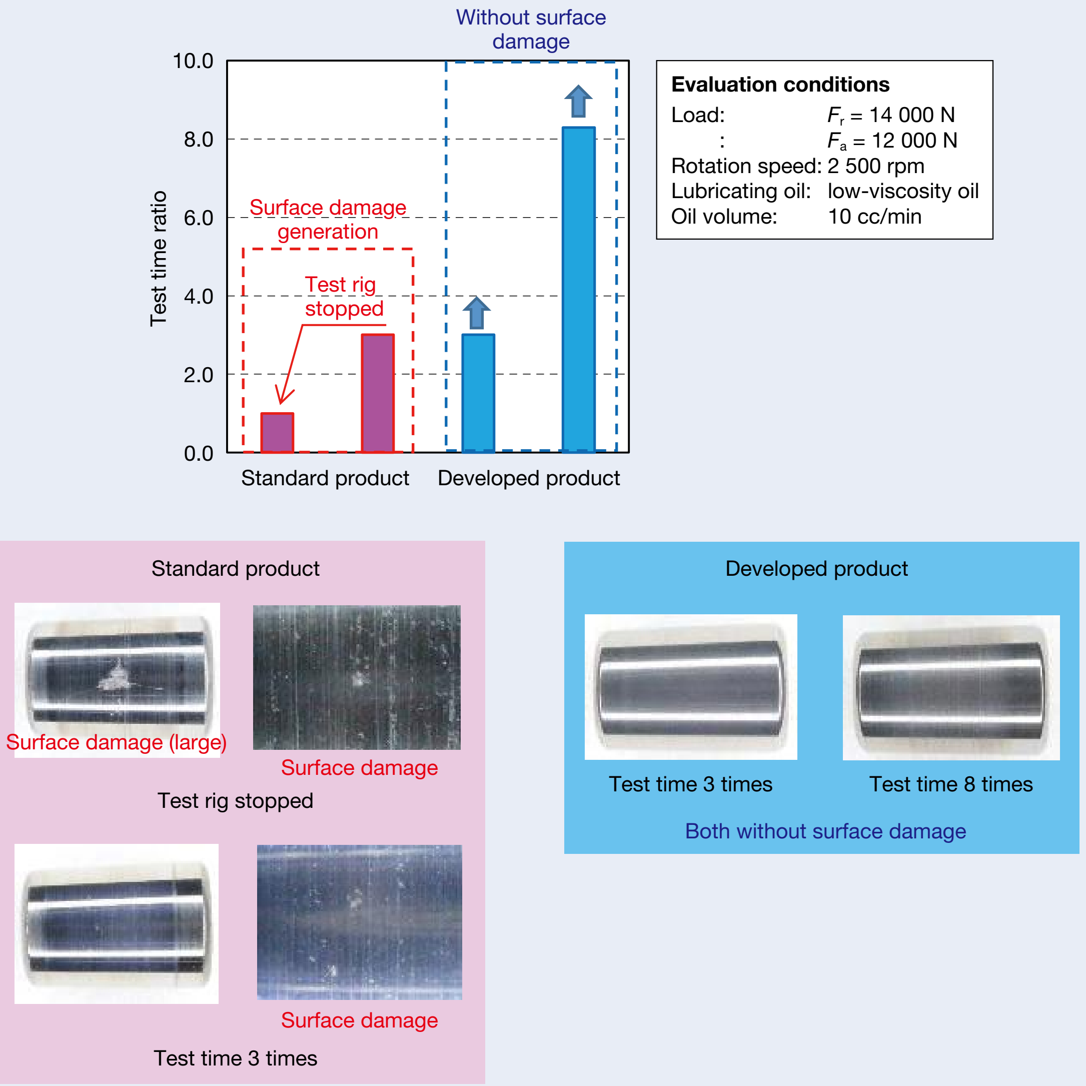

Fig. 7 Bearing endurance test results

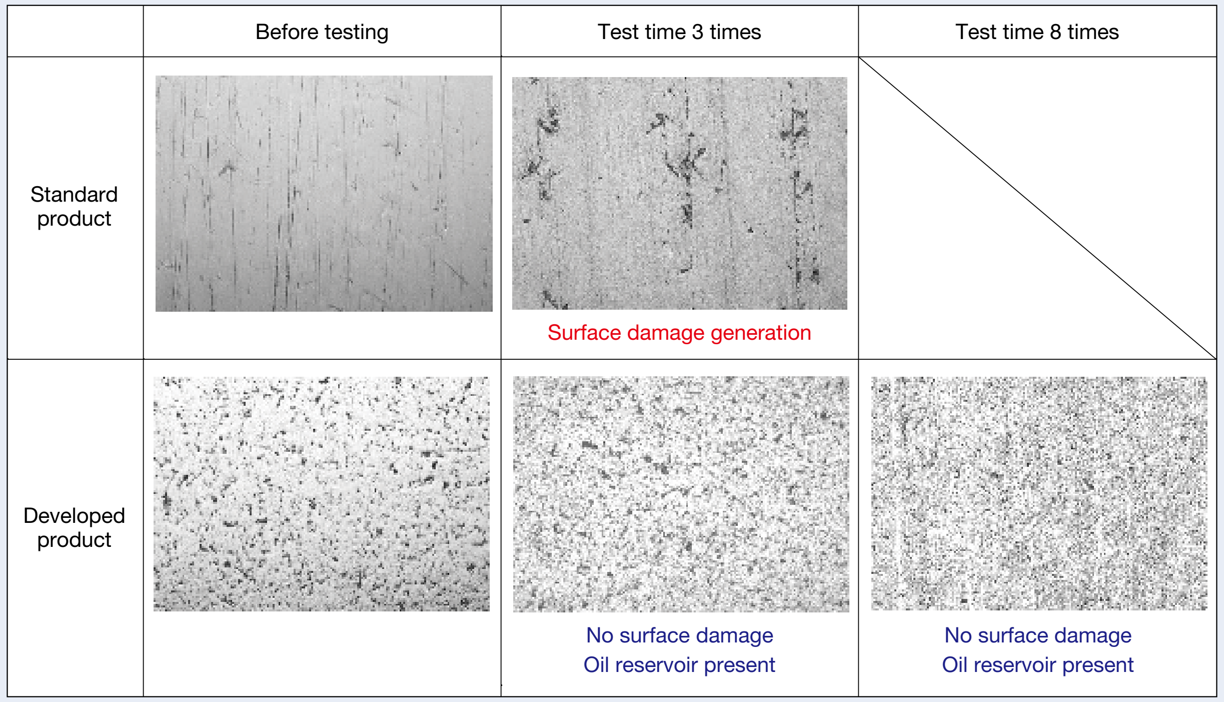

Fig. 8 Comparison of enlarged surface photographs

3.3 Seizure suppression effect and low friction effect

In order to confirm the effects of LCube II on seizure and friction characteristics of tapered roller bearings, tests were conducted using low-viscosity oils.

Measurements were carried out with load applied only in the axial direction, focusing on the characteristic effects of sliding friction due to the application of LCube II.

Figure 9 shows the change in temperatures of the developed product and the standard product at the inner ring rib surface in seizure tests. Before the start of the test, several drops of lubricant were added to the sliding surface. The test compared the times just before seizure occurred on this sliding surface in a non-lubricated environment. Considering the temperature transition until seizure occurred (the point at which the temperature curve changed sharply), the seizure resistance of the developed product is equal to or better than that of the standard product.

Figure 10 shows the friction measurement results of the developed product and standard product. The low friction effect of up to 10% was confirmed for the standard product under low speeds (up to 1 000 rpm). This is a result of the effect of the oil reservoirs in LCube II, which retains lubrication even under low speeds where oil film formation is typically low.

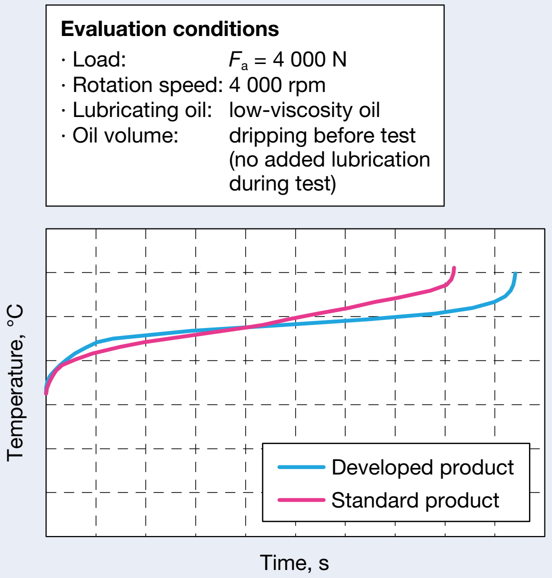
Evaluation conditions
· Load: F_a = 4 000 N
· Rotation speed: 4 000 rpm
· Lubricating oil: low-viscosity oil
· Oil volume: dripping before test (no added lubrication during test)

Fig. 9 Bearing seizure test results

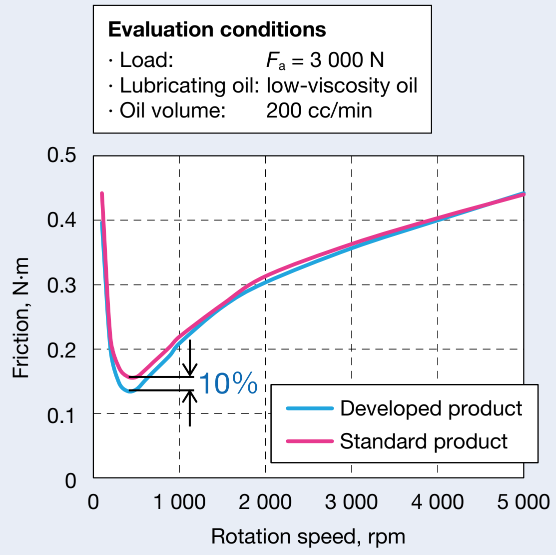
Evaluation conditions
· Load: F_a = 3 000 N
· Lubricating oil: low-viscosity oil
· Oil volume: 200 cc/min

Fig. 10 Bearing friction measurement results

4. Postscript

NSK has developed first-generation to sixth-generation low-friction tapered roller bearings and has been contributing to improvements in the gearbox efficiency and fuel efficiency of automobiles through high durability and reliability.

However, accelerated development of electric/hybrid vehicles in recent years prompted NSK to develop a highly robust bearing designed for use in harsh lubricating environments, the motivation behind the development of LCube II.

LCube II tapered roller bearings can be applied to gearboxes with harsh operating environments and can replace the standard products without the need for changing the internal specifications of the bearings. We are currently in the midst of an automotive technology revolution, said to occur only once every 100 years. We will continue to develop highly reliable, low-friction bearings that meet the needs of the marketplace while also continuing to contribute to improvements in electric/hybrid vehicle fuel efficiency, power consumption, and reliability.

References

1) "NSK LCube Series of Highly Durable Tappet Rollers," *NSK Technical Journal*, 677 (2004) 66–67.
2) "Low-Friction Technology for Tapered Roller Bearings," *NSK Technical Journal*, 690 (2018) 51–59.
3) S. Aihara, "Friction of Roller Bearings and EHL Viscous Rolling Resistance," *NSK Technical Journal*, 649 (1988) 1–5.

Masaki Chishima

Technologies of NV Measurement and Analysis for Steering Systems

Masayuki Kanatsu
Steering & Actuator Technology Center, Steering R&D Center, Steering Performance & NVH Engineering Group

Abstract

In recent years, demand for quiet automobiles has been increasing, which results in higher demand for quieter steering systems. The difficulties of NV (= noise and vibration) technologies for steering systems are caused by various kinds of NV phenomena, which change depending on the vehicle and environment. This report shows examples of NV measurement and analysis and a mechanism of rattle noise and operating noise, which are particularly problematic among NV phenomena related to steering systems. Currently, the simulation model that qualitatively reproduces rattle phenomena has been built based on previous investigation and used to predict and improve NV performance of column-type EPS systems.

1. Introduction

In recent years, reduction of CO_2 emissions is required for worldwide global environment protection. Particularly in Europe, the trend toward electrification has been accelerated due to severe fuel mileage regulations. Along with electrification, advances in autonomous driving technologies are also remarkable, and a worldwide revolution is in progress. Under this background, demand for quiet automobiles has been increasing, resulting in higher demand for quiet steering systems.

For NSK, ideal steering systems give the drivers a sense of unity with the vehicle. In addition to the basic performance required for a steering system “turning,” NSK’s steering system with NV performance provides comfort as key performance.

The difficulties related to NV technologies in steering systems are caused by various kinds of NV phenomena, which change depending on the vehicle and environment. Therefore, what is required is the establishment of technologies for NV measurement and analysis that are suitable for NV phenomena of steering systems.

In this report, examples of applying various types of NV measurement and analysis technologies to NV phenomena of steering systems are provided.

2. Overview of NV Technologies for Steering Systems

2.1 Typical examples of NV problems with steering systems

Typical examples of NV phenomena of steering systems are shown in Table 1. Table 1 summarizes NV phenomena of column-type EPS systems.

As shown in Table 1, NV phenomena of steering systems are classified into “abnormal noise during driving,” “operating noise,” “noise when holding steering wheel,” “noise from reverse steering,” “tilt/telescopic operating noise,” etc. Among these, “abnormal noise during driving” includes “rattle noise” generated by hitting at the looseness of each part of the steering system, which is caused by reverse inputs from the road surface and “steering wheel vibration” due to mechanical resonance of the steering system. Regarding “operating noise,” there are “floor vibration” caused by assist torque fluctuation due to resonance of the mechanical part or insufficient control stability and “operating noise of the motor” generated by the order components of the motor. Since “operating noise” is caused by not only mechanical (reduction gear) factors but also hardware (motor) and software (control) factors, it occurs over a very wide range of steering speed and frequency band.

As described above, there are a wide variety of NV phenomena of steering systems. In this report, rattle noise and operating noise, which are particularly problematic in steering systems, are focused on.

Table 1 Typical NV phenomena in steering systems

Occurrence Status		Typical Examples	Causes of Occurrence
Abnormal noise while driving	Abnormal noise generated when driving on rough roads	Rattle noise	A hitting noise generated at the backlash of each part of the steering due to reverse input from the road surface
	Steering wheel vibration when driving	Steering wheel vibration	Vibration generated by the mechanical resonance of the steering system
Operating noise	Abnormal noise generated during stationary steering	Floor vibration	Vibration caused by assist torque fluctuation due to mechanical resonance or insufficient control stability
		Motor operating noise	NV generated by the order component of the motor
Noise when holding steering wheel	Noise generated when holding the steering wheel	NV felt on the steering wheel	NV due to the high frequency assist torque fluctuation of the motor
Noise from reverse steering	Abnormal noise generated when reversing the steering wheel	NV felt on the steering wheel	NV generated from the steering components due to the input when the steering wheel is reversed
Tilt/telescopic operating noise	Abnormal noise generated during tilt/telescopic adjustment	Tilt/telescopic lever operation sound	NV due to poor lubrication of sliding parts, etc.

2.2 Goals of steering NV technologies

2.2.1 Standardized approach for NV investigation

One reason for the wide variety of NV phenomena of steering systems is the presence of various NV sources and complicated mechanisms. Therefore, it is essential to establish an investigation flow to understand the phenomena quickly and identify the cause of NV problems with steering systems. NSK has established a standardized investigation flow, as shown in Figure 1, and is dealing with various NV problems.

Technologies required at each stage of the standardized investigation flow are shown in Figure 1. "Specify mechanism," which covers impact source → transfer path → radiation surface, is crucial for planning effective countermeasures. In particular, the need for building technologies of impact source identification with parts level has increased in recent years, as it can be basis to specify mechanism.

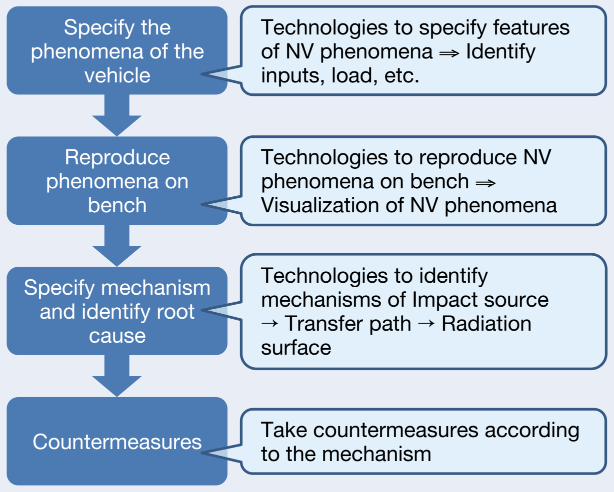

Fig. 1 Standardized approach for investigating NV problems

2.2.2 Measures to prevent NV problems

On the other hand, in order to prevent NV problems in steering systems, a model-based development method, commonly referred to as the V-process of development, is effective. As shown in Figure 2, a technique for designing NV performance at the system level, unit level, and component level by 1D or 3D simulation at the design stage has to be built. Here, 1D simulation is often used to examine NV performance with system-level and 3D simulation to examine NV performance at the unit and component levels. NSK will build simulation techniques to design NV performance by repeating a small V-shape at an early stage of steering system design (i.e., the left side of the V-shape).

Furthermore, as for validation of NV performance conducted on the right side of the V-process, NSK will define an original evaluation method and target value for NV and conduct an evaluation at each level in order to perform appropriate evaluation at each level of components, units, system, and vehicle.

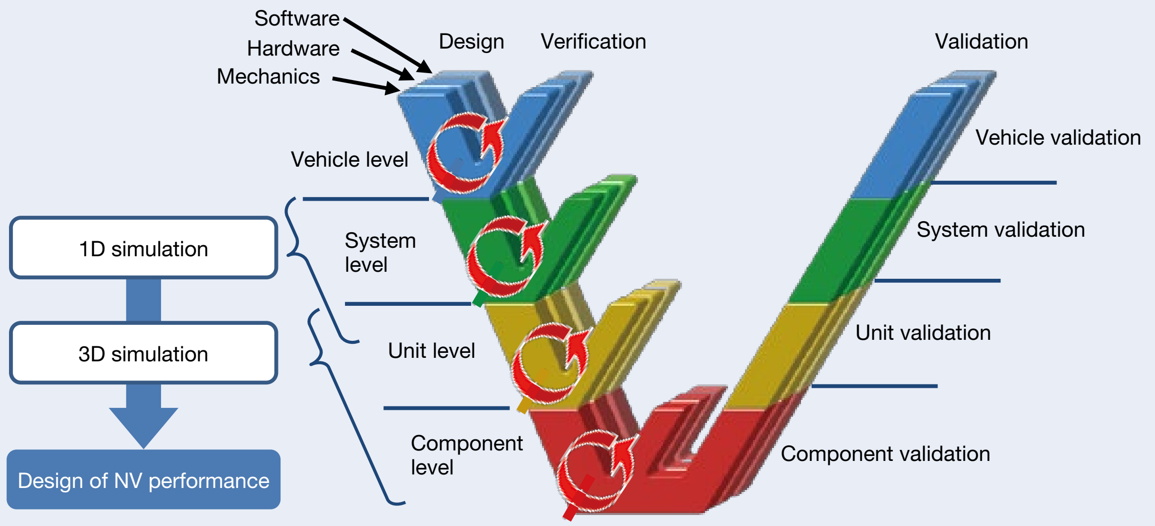

Fig. 2 V-shaped process for preventing NV problems

2.3 Challenges for realizing the goal to be achieved

As described in the previous section, it is essential to establish an investigation flow for specifying phenomena quickly and identifying causes for NV problems with steering systems. In particular, building an impact source identification technology with components level is required. At NSK, there are some cases where impact source identification was attempted with the unit level using the time difference of vibration transmission obtained by multi-point measurements for non-stationary noise such as rattle noise. However, since it is difficult to directly measure impact phenomena inside steering systems, impact source identification with component level (element level) has not reached the practical level, and no case has been found outside of NSK, either.

For building technologies to predict NV performance at the design stage in order to prevent NV problems with steering systems, it is necessary to specify the mechanism for building simulation models based on physical phenomena and to build measurement and analysis technologies to validate the model. In order to address these issues, NV measurement and analysis technologies for steering systems will be improved continuously.

3. Technologies of NV Measurement and Analysis for Steering Systems

3.1 Standardized method for NV measurement and analysis

3.1.1 Standardized measurement method

For NV measurement of steering systems in the early stage of various NV investigations, collection of time-domain data by multi-point measurement is often required in order to understand phenomena quickly and lead to cause analysis. NSK has defined standardized measurement positions of NV, which are considered to be important for specifying differences between OK and NG products, based on past experiences. One example is shown in Figure 3.

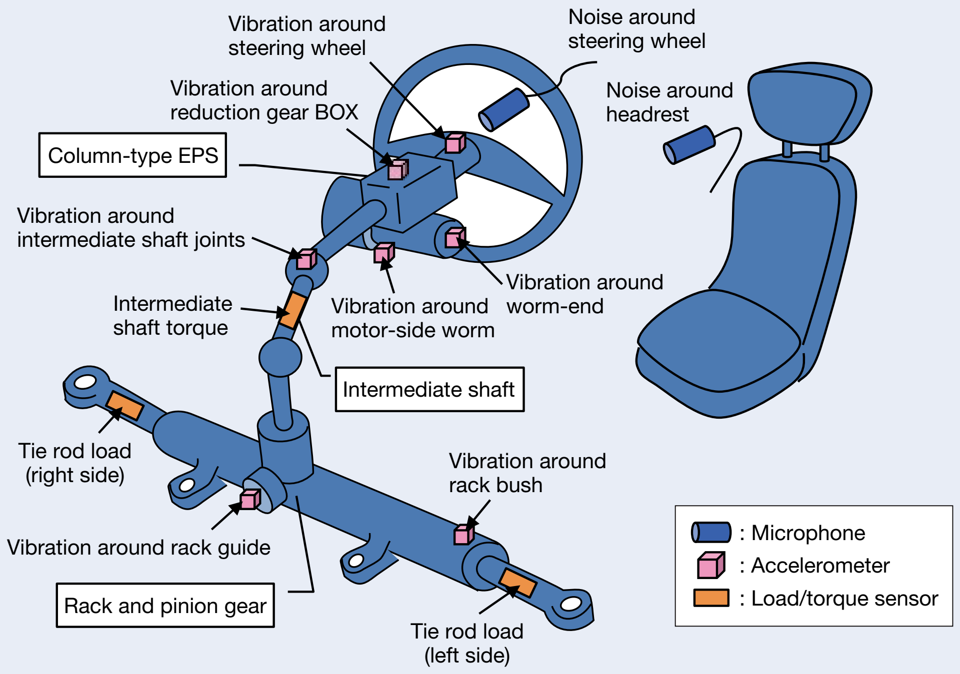

Fig. 3 Example of NV measurement positions on a steering system

As shown in the example of the measurement system in Figure 4, in addition to NV at each part, inputs to the steering system (load, torque, rotating speed, etc.) and physical behaviors (displacements, etc.) of each component of the steering system are also measured synchronously as required and used for specifying phenomena more in detail and analyzing causes. As part of specifying phenomena, various types of information obtained from the vehicle, where NV phenomena are occurring, are used as input information for tests reproducing the phenomena of vehicle on bench at NSK, thereby leading to reproduce the phenomena and specify the mechanism.

3.1.2 Standardized analysis method

The methods shown in Table 2 can be used to analyze the various NV phenomena of steering systems. The main analysis methods[1] and their scope of application are shown in the table. Features of NV phenomena can be specified by selecting an appropriate analysis method or by performing analysis in combination with various methods depending on NV phenomena to be analyzed.

In recent years, there are more cases where large-volume time-domain data is collected by performing large-scale, multi-point measurement in order to perform sensitivity analysis for NV, etc., and NV analysis tools, which allow for more efficient processing of time-domain data, are in higher demand.

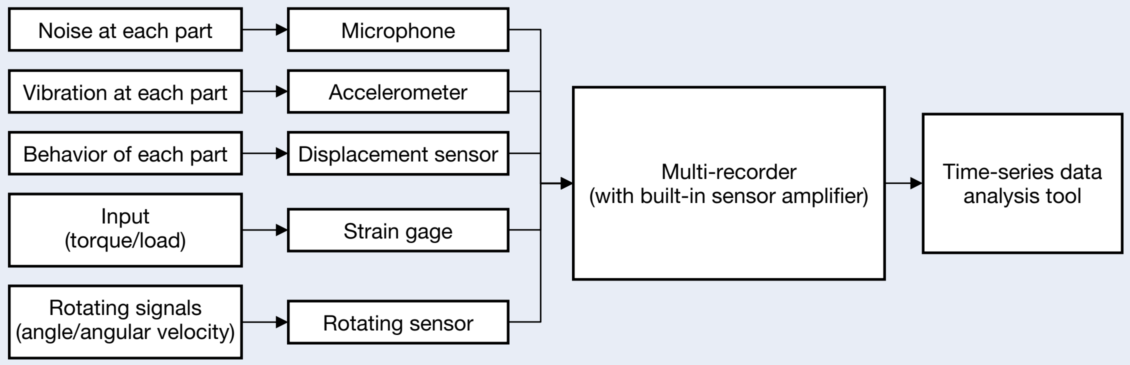

Fig. 4 Example of NV measurement system

Table 2 Methods for NV analysis

Method	Time Waveform	FFT Analysis	STFT Analysis (Short-time FFT)	Tracking Analysis
Features	Possible to specify the temporal change of the vibration phenomena, their magnitude, and features of the periodically repeated phenomena	Frequency component of the time waveform can be specified	Possible to capture temporal changes of the frequency components in non-stationary signals[1]	Possible to identify the cause of stationary noise and vibration of a rotating machine
Issues	When the time waveform becomes complicated, specifying the features becomes difficult	Not suitable for analysis of intermittent or non-stationary signals	Both time resolution and frequency resolution are relatively low[1]	Not suitable for analysis of non-stationary noise and vibration
Fields of Application	NV phenomena in general Observe time waveforms of NV, input, and behavior in combination with various filters	Stationary NV phenomena Examples: steering wheel vibration, noise when holding steering wheel, etc.	Non-stationary NV phenomena Examples: rattle noise, noise from reverse steering	Stationary NV phenomena (rotation-dependent component) Example: operating noise

3.2 Methods for investigating impact and transfer mechanism of NV

3.2.1 Current status of impact source identification

Until now, when various types of NV problems occur, the strategies of investigation, where the parts and units that are estimated to be impact sources are replaced with new ones (or normal ones) and the impact source is narrowed down by checking the change of the status (i.e., reduction or elimination of NV level). However, this method often depends on the operator's experience and sense to decide the priorities of disassembly/parts replacement, and it takes a long time to identify the impact source. Therefore, what is needed is the establishment of a method for impact source identification for specifying phenomena, identifying mechanisms, and taking countermeasures quickly.

As an alternative to specifying the impact source by exchanging components and units as described above, the time difference analysis method using NV time domain data by multi-point measurement and the MT (Mahalanobis-Taguchi) method[2], for pattern recognition, are considered to be effective at present. Table 3 shows the outline and technical issues of both methods.

In the future, a method, where the impact source is identified directly without restriction of the sample to be compared, will be built at NSK.

3.2.2 Transfer Path Analysis

Transfer Path Analysis (TPA) is a technique for specifying the paths and their contribution quantitatively, where vibration and force generated at the impact source propagate through the transfer path, including the vehicle, and the noise is radiated from the radiating surface to reach the driver's ear. Figure 5 shows an example of conducting a transfer path analysis for rattle noise on a steering system. Here, the analysis was carried out for structure-borne where the noise is transferred from the mounting point of the steering to the vehicle, through the vehicle, and to the driver's ear, and airborne where the noise is radiated directly from the steering surface. As shown in Figure 5 (a), structure-borne is dominant basically below 1 kHz, whereas air-borne is dominant above 1 kHz. At around 1 kHz, both contributions can be confirmed. In order to specify the major transfer paths for the main peaks observed here, contribution of each path to the noise reaching the driver's ear has been evaluated as shown in Figure 5 (b). As a result, the transfer paths with high contribution are as follows: around 530 Hz, structure-borne through the mounting point of column-type EPS, around 1 250 Hz, air-borne radiating from the steering wheel, and around 1 750 Hz, air-borne radiating from the ECU cover.

Transfer path analysis can be used to reduce the noise transferred to the driver's ear by improving the characteristics of the transfer path with high contribution, even when it is difficult to take measures for the impact source in the event of an NV problem caused by the steering system. For example, it is possible in this case to reduce the radiated noise with 1 750 Hz by taking such measures as attaching a vibration insulating sheet on the ECU cover.

Table 3 Methods for impact source identification

Method	Time Difference Analysis Method	MT Method
Summary	Method for estimating the impact source, in which the rising timing of the pulse-like components that appear on the vibration time waveform at each measurement point are compared and the earliest point is identified as the impact source	Method for quantifying the feature (amplitude and cycle) of the vibration waveforms of good and defective products by pattern recognition and estimating the location with a large difference as the impact source
Issues	Know-how such as filtering of time waveform, selection of vibration measurement position, and judgment of the rising timing must be accumulated	Samples to be compared and data for both are required Examples: good products, defective products
Fields of application	NV phenomena that generate pulse-like components Examples: rattle noise, noise from reverse steering	NV phenomena in general (when the comparison target exists)

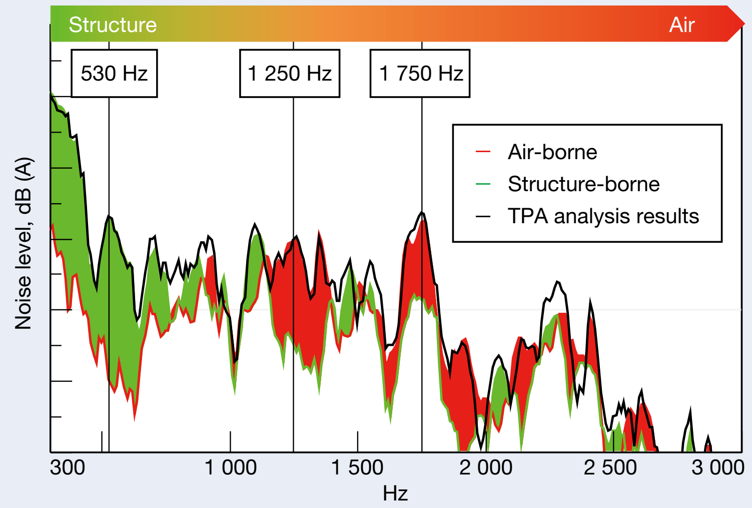

(a) Contribution of structure-borne and air-borne

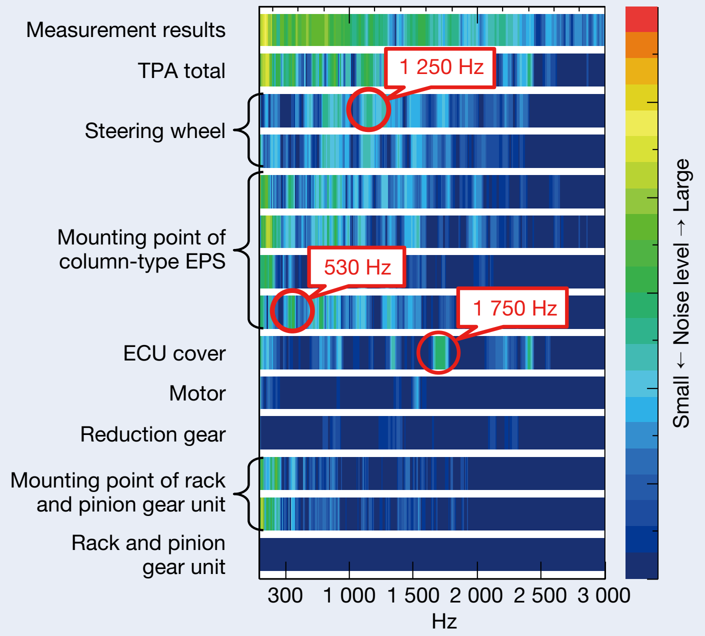

(b) Contribution of each path

Fig. 5 Results of transfer path analysis (rattle noise)

3.2.3 Noise source identification

In the field of visualization techniques for the sound field, the beamforming and acoustic holography methods are popular, and the sound field can be visualized by microphone array, etc., commercially available from many companies. In recent years, various companies have released equipment capable of visualizing noise sources in real time, and along with the expansion of analysis functions by software, performance in low-frequency bands is being improved. As a result, transient noise such as rattle noise and noise source in the low-frequency range can be localized with relatively high accuracy. Thus, it is essential to use appropriate equipment and analysis functions depending on the purpose.

Figure 6 shows an example of noise source identification for a steering system. Figure 6 is an example of visualizing the noise source of rattle noise. It shows the radiation from the ECU cover, which was identified as one of the air-borne paths from the results of the transfer path analysis in the previous section. In such cases, it is effective to take countermeasure to reduce the radiation of noise from the ECU cover. In this way, by combining noise source identification with other NV measurement and analysis techniques, the mechanism of abnormal noise can be identified and effective countermeasures can be taken.

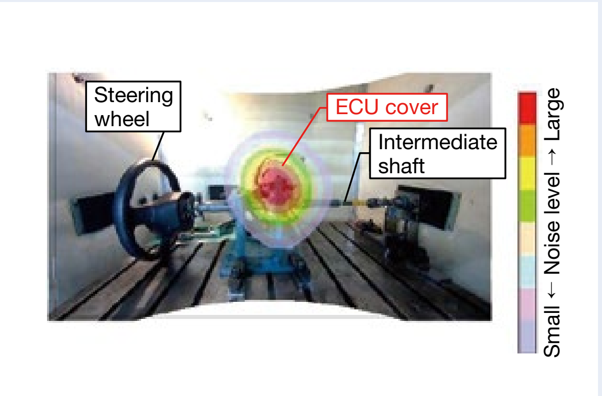

Fig. 6 Result of noise source identification (rattle noise)

Table 4 Driving conditions and measurement conditions for rattle noise evaluation

Driving conditions	Driving surface	Rough road (cobble road)
	Driving speed	20 km/h
	Driving pattern	Straight ahead
Measurement conditions	Sampling frequency	20 kHz or more
	Recording time	10 sec

4. Examples of Investigation of NV Phenomena

4.1 Example of investigation of rattle noise

In this section, examples of specifying phenomena and the mechanism of rattle noise, which is generated due to reverse input from the road surface to the steering system and tends to be problematic, are introduced.

First, in order to understand the phenomena of rattle noise on the vehicle, noise, vibration, and inputs at each part during rough road driving were measured according to the standardized measurement technique shown in the previous section. Examples of driving conditions and measurement conditions are shown in Table 4.

An example of the results is shown in Figure 7, including a time waveform of the noise at the steering wheel and intermediate shaft torque when rattle noise is generated. In order to easily observe rattle phenomena, A-weighting and bandpass filtering are applied to the noise at the steering wheel. Figure 7 shows that pulsed components are generated when intermediate shaft torque

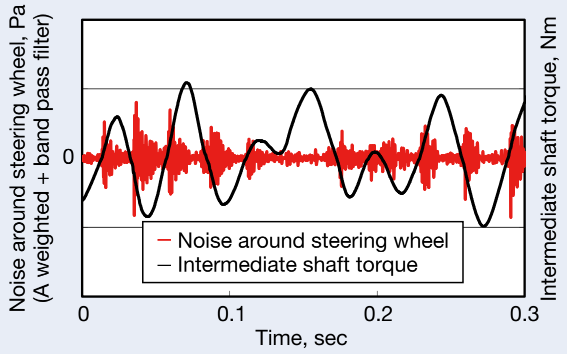

Fig. 7 Time waveform of rattle noise and intermediate shaft torque

is reversed.

Next, frequency analysis of tie-rod load and intermediate shaft torque was conducted in order to understand the vibration inputs to the steering system, which causes rattle noise. An example of the results is shown in Figure 8. In the figure, the frequency spectrum of tie-rod load and intermediate shaft torque shows the common low-frequency components (f1 and f2 in the figure). When these low-frequency components are large, the rattle noise level is high. Therefore, these low-frequency components are considered to be the main vibration inputs to the steering system.

In order to further investigate the relation between the main vibration inputs and rattle noise for the steering system, operational analysis was conducted, as shown in Figure 9. The figure shows an example of operational analysis on the frequency axis. The vibration behavior in the rotating direction of the intermediate shaft at the low-frequency component of f1 is almost synchronized with the vibration behavior in the tie rod axial direction. The results confirmed that the low-frequency vibration generated in the intermediate shaft was caused by vibration components along the tie-rod axis (Y: vehicle lateral direction).

Although the frequencies of the low-frequency components (f1 and f2) in Figure 8 vary depending on the type of vehicle, driving speed on rough roads does not have much effect. Therefore, these low-frequency components should be caused by resonance around the suspension.

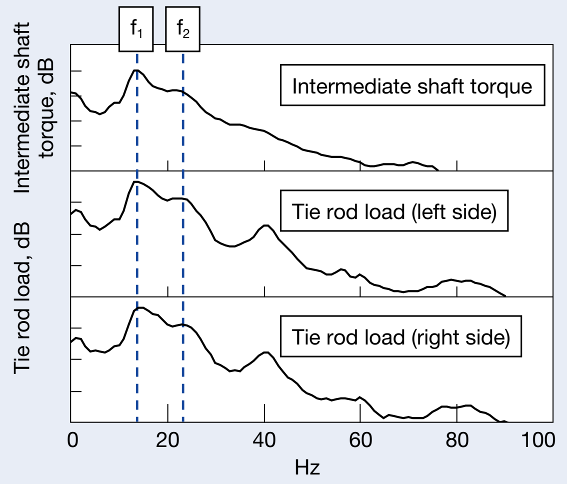

Fig. 8 Vibration input applied to steering system causing rattle noise

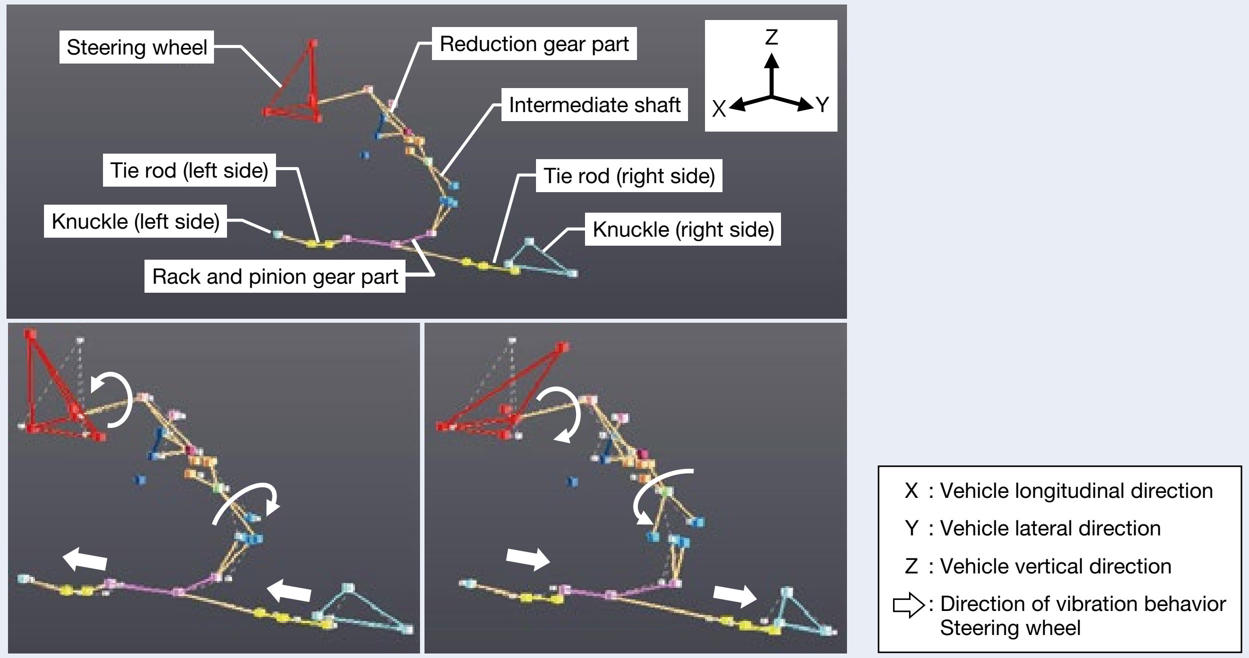

Fig. 9 Operational deflection shape and animation of vibration causing rattle noise (focusing on the frequency component of f1 in Fig. 8)

From the results, the mechanism of rattle noise is summarized in Figure 10. Resonance of the suspension excites the rack in the axial direction, causing the torsional vibration of the rotating shaft through the intermediate shaft to the steering wheel, which causes hitting at the part having a looseness in synchronization with the vibration, which in turn results in rattle noise.

4.2 Examples of investigation of operating noise

In this section, examples of specifying phenomena and the investigating mechanism of operating noise are introduced. It is known that operating noise is caused by the mechanism (reduction gear, etc.) of each part operating with steering inputs to the steering system and the hardware (motor) and software (control), which assist their operation, and it is generated over a very wide range of steering speeds and frequency bands. The operating noise introduced here is remarkable due to resonance between the natural frequency of the components or units in the steering system and the order of components depending on steering speed.

In measuring operating noise, it is necessary to specify steering speed, where the noise and vibration increase, its feature, and its cause. Therefore, in the measurement of operating noise, rotating speed has to be measured in synchronization with the NV of each part. Figure 11 shows a schematic of operating noise measurement. Examples of steering conditions and measuring conditions are shown in Table 5.

Figure 12 shows an example of tracking analysis based on the vibration time-series data obtained in this way. The vertical axis in the diagram is obtained by converting the steering speed of the steering wheel to the rotating speed of the motor (worm) while considering the gear ratio of the reduction gear. In the figure, order component A synchronized with the rotation of the motor and its N times order components (order components 2 × A, 3 × A…N × A in the figure) are shown. In this example, since order component A matches the number of segments of the brush motor, it can be seen that vibration is caused by torque fluctuation generated in the motor per each rotation. N times order component of order component A should be generated by the phase shift of the brushes and

Table 5 Operating conditions and measurement conditions for operating noise evaluation

Steering conditions	Steering speed (steering wheel)	0–1.5 rps
	Steering pattern	Sweep (up)
	Rotating load	Constant
Measurement conditions	Sampling frequency	10 kHz or more
	Recording time	60 sec

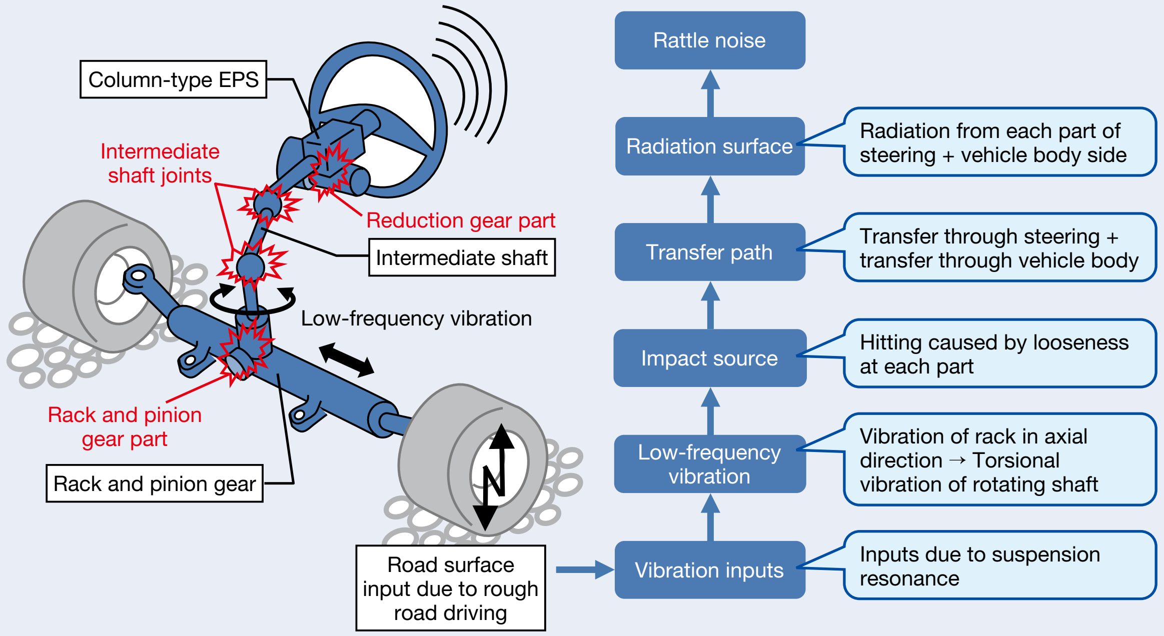

Fig. 10 Mechanism of rattle noise

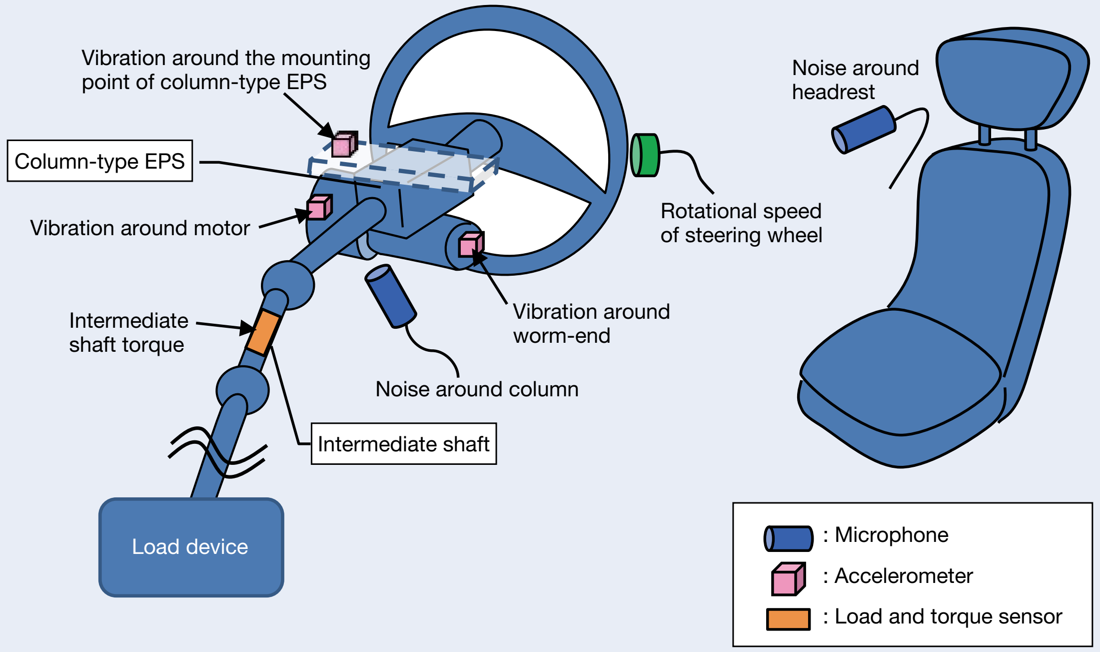

Fig. 11 Example of measurement positions for operating noise on a steering system

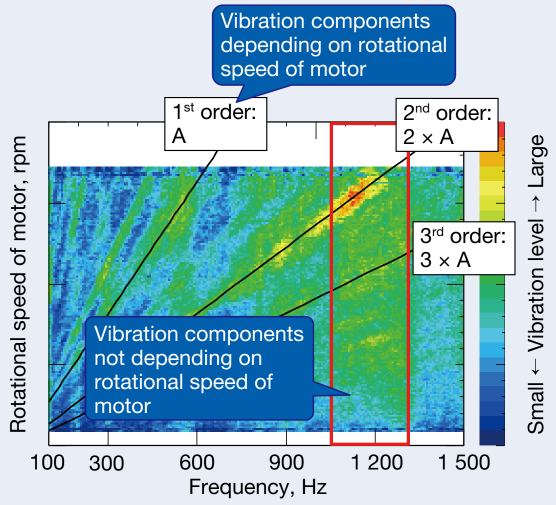

Fig. 12 Result of tracking analysis for operating noise

segments.

In addition, when focusing on the frequency band (red frame part in the figure) where the level of order component A becomes the highest in the figure, the vibration level is relatively high regardless of the motor's rotating speed. In this frequency band, it is considered that a natural frequency of a part or unit that comprises the steering system is observed. In order to confirm this experimentally, operational analysis of the steering system, when the operating noise was generated, was performed, and the vibration behavior of each component was measured. The results are shown in Figure 13. From the figure, it was found that the part where the most remarkable vibration behavior appears in the focused frequency band is the ECU cover and that the ECU cover produces pumping behavior in the out-of-plane direction (the direction indicated by the red arrow in the figure).

From the results described above, the generation mechanism of the operating noise in this example is summarized as follows. The EPS motor generates assist torque according to load by steering inputs. At that time, torque fluctuation should occur due to the number of segments of the motor and the phase shift of brushes, causing vibration force to vibrate the ECU cover, which is easily excited among the components in the steering system, causing the operating noise.

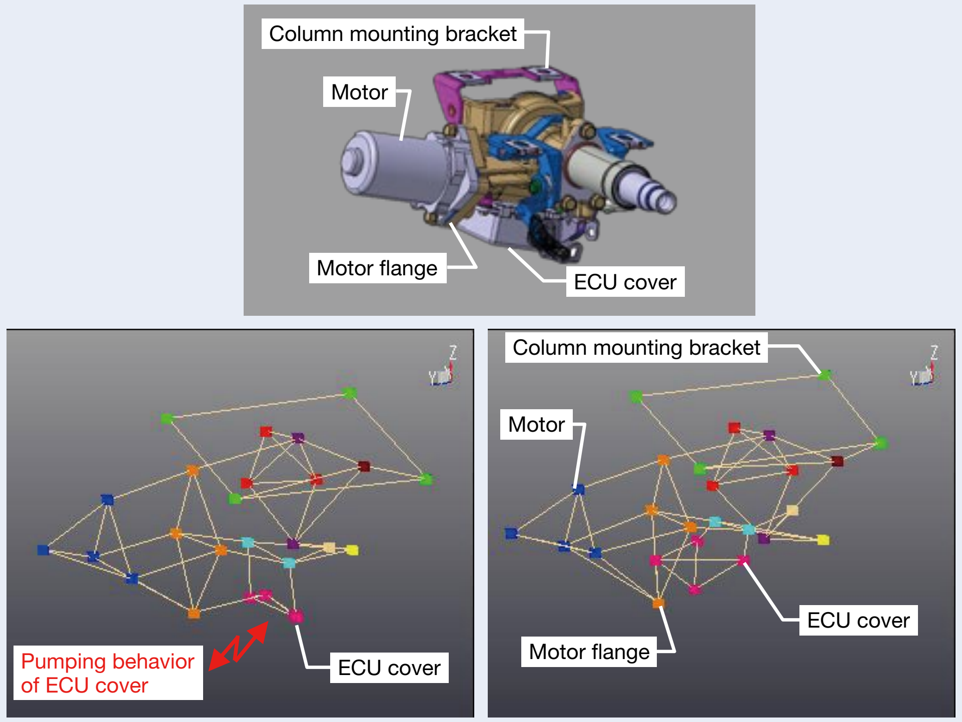

Fig. 13 Operational deflection shape and animation for operating noise

5. NV Simulation Techniques

Examples of simulation to reproduce the rattle phenomena using three-dimensional multi-body simulation software are introduced in this section. As shown in Figure 14, the steering system from R&P to the steering wheel was modeled, including the control system. In addition, the tie-rod load measured on the vehicle was applied to the steering system, and the resulting low-frequency vibration, impact source (impact force at looseness), and transfer path (vibration of the steering wheel) were reproduced.

5.1 Reproduction of low-frequency vibration that causes rattle noise

First, the low-frequency vibration, which causes rattle noise, was simulated and compared with the vehicle test results. An example of the results is shown in Figure 15. In (a) of the figure, the time waveform of the low-frequency vibration of each part of the steering system is shown, and in (b) the measuring positions of the low-frequency vibration of each part of the steering system is shown. From Figure 15, it can be seen that the low-frequency vibration of each part obtained by simulation, including the control using the tie-rod load measured on the vehicle as input, almost quantitatively coincides with the results measured on the vehicle. The results show that the low-

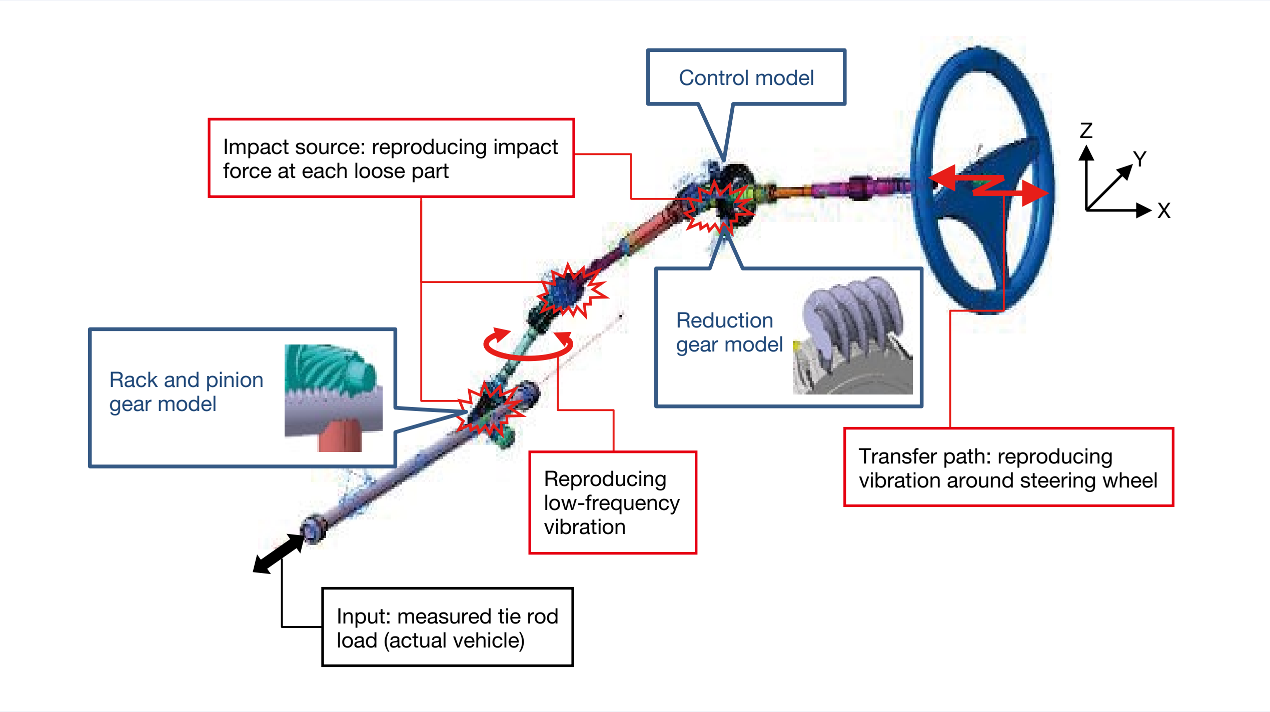

Fig. 14 3D-simulation model for rattle noise

frequency vibration, which is the source of rattle noise in column-type EPS systems, can be reproduced.

Next, using the developed simulation model, the impact force at each looseness, which is the impact source of the rattle phenomena of the column-type EPS system and also the effect of the impact force on vibration of the steering wheel generated by the transmission of the impact force were investigated. In this study, the simulated rattle vibration levels of the steering wheel were compared with the test results for the samples with the normal backlash size as ① standard and with backlash sizes as ② to ⑦. An example of the results is shown in Figure 16. Figure 16 shows that the impact of the backlash measured on the vehicle is qualitatively consistent in simulation results as well. From the results, it was confirmed that the rattle phenomena of the column-type EPS system is reproduced with the system level.

5.2 Reproduction of rattle phenomena at the unit and component levels

5.2.1 Improvement of simulation model

In Section 5.1, it was confirmed that the rattle phenomena of the column-type EPS system are reproduced with the system level. However, as shown in the V-model (see Section 2.2.2), to prevent NV problems, it is essential to develop a technique for designing NV performance at the unit and component levels. Therefore, the accuracy of the simulation model shown in Figure 14 was improved to reproduce the rattle phenomenon in more detail at the unit and component levels. In this attempt, as shown in Figure 17, the simulation model was improved by 3D modeling of the reduction gear in detail and setting the friction and damping parameters of each part based on measured data.

5.2.2 Comparison of bench test and simulation results of rattle phenomena

Using the simulation models improved as described in Section 5.2.1, vibration of the steering wheel and behavior of the worm were simulated, and the results were compared with the results of bench tests. An example of the results is shown in Figure 18. Intermediate shaft torque measured in bench tests were applied as input to the simulation models. Figure 18 (a) shows the time waveform of vibration of the steering wheel, and Figure 18 (b) shows the behavior (displacements) of the worm on the X-Y plane. In addition to the worm trajectory, the figure of the worm behavior shows noise levels (bench test results) and vibration levels (simulation results) at the same time with the size and color of the circle (the larger and the redder the circle, the higher the level). From (a) in the figure, it can be seen that the timing of the pulsed components, which is the feature of rattle phenomena, are observed when intermediate shaft torque is reversed in both bench tests and simulation results,

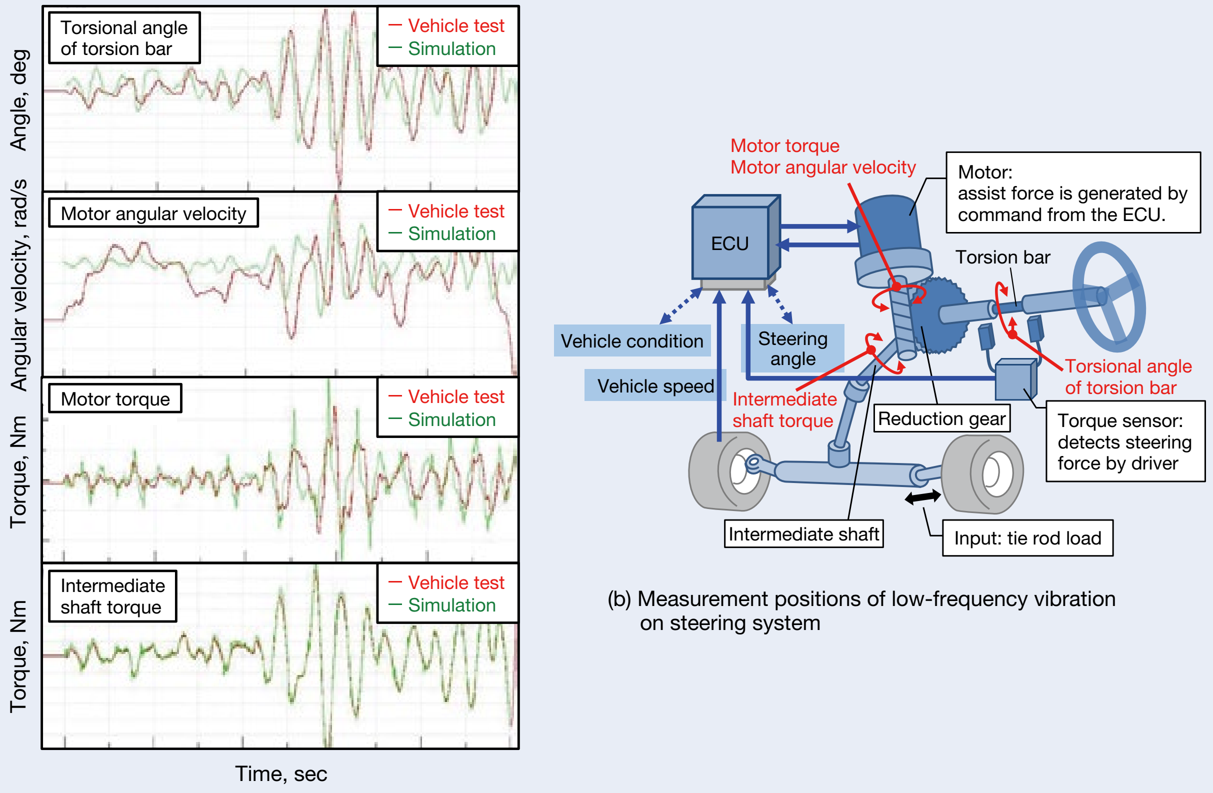

(b) Measurement positions of low-frequency vibration on steering system

(a) Time waveform of low-frequency vibration on steering system

Fig. 15 Comparison of low-frequency vibration between measured data on vehicle and simulation

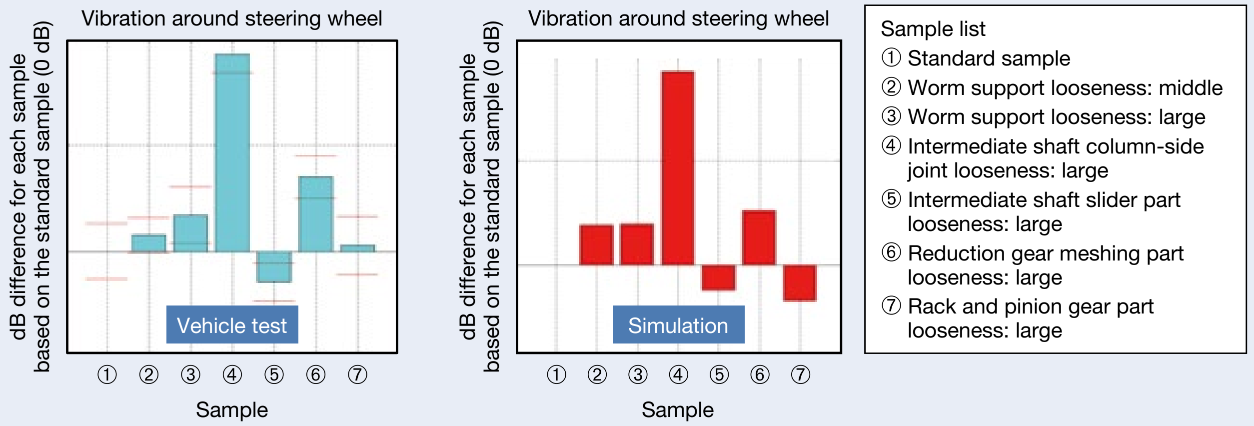

Fig. 16 Comparison of rattle vibration caused by looseness between measured data on vehicle and simulation

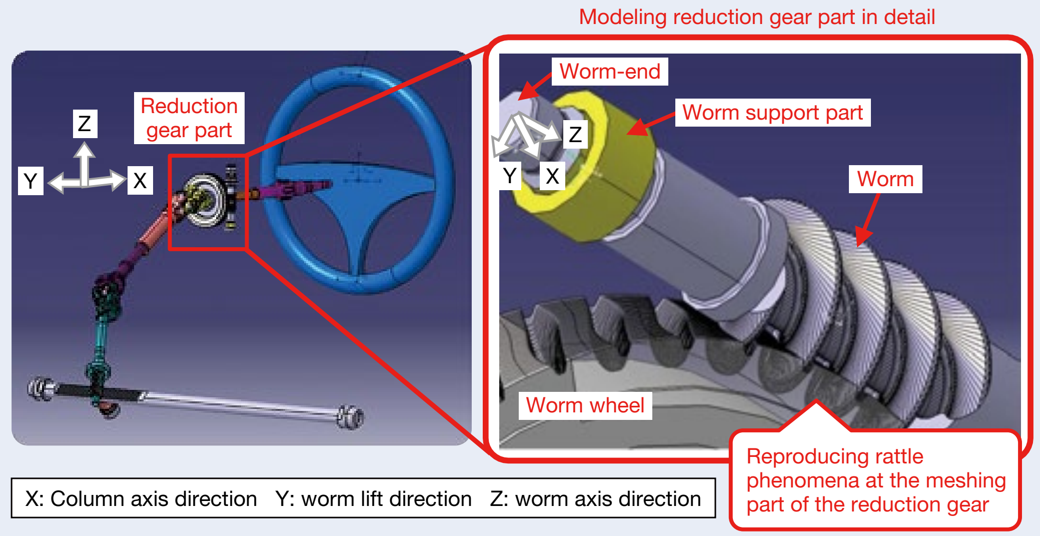

Fig. 17 Detailed 3D modeling of reduction gear

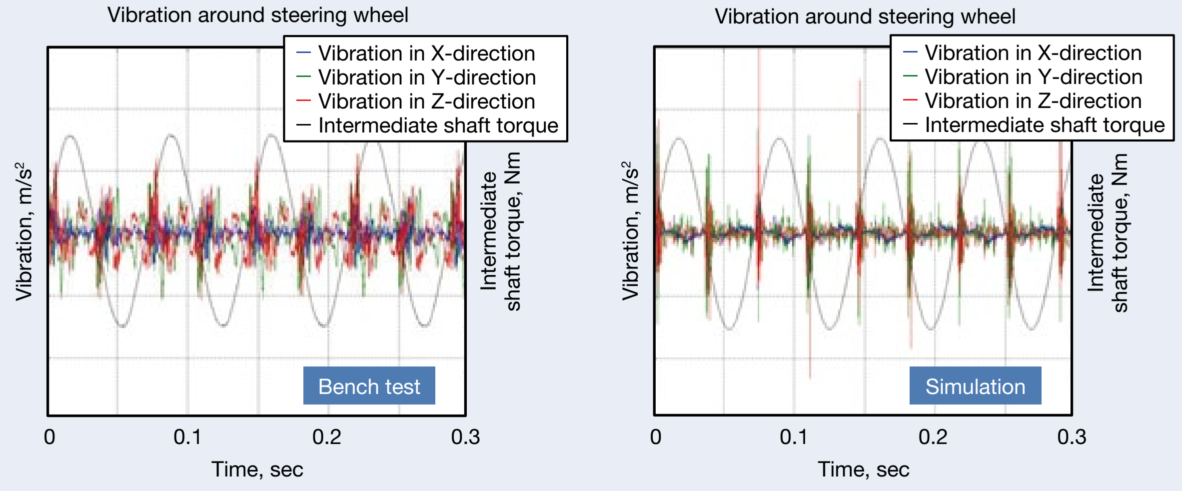

(a) Time waveform of vibration around steering wheel

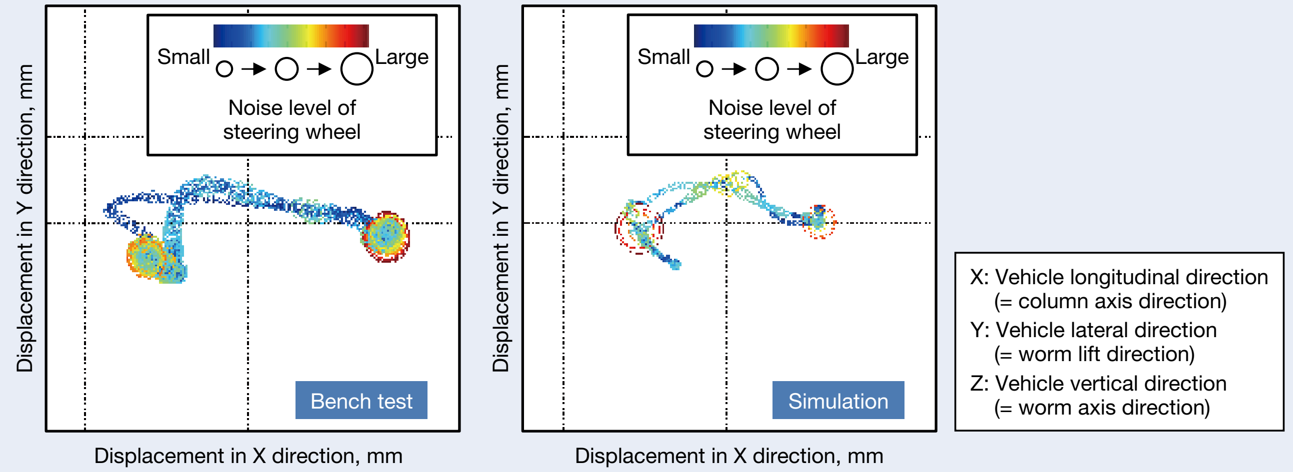

(b) Vibration behavior of worm and NV levels

Fig. 18 Comparison between measured data on bench and simulation for rattle phenomena

and also the magnitude of the pulsed components of each almost coincides. From (b) in the figure, it can be seen that the behavior of the worm has a similar trajectory in the bench test and simulation results. Both bench tests and simulation results show that noise levels and vibration levels are higher at both ends in the X-direction (column axial direction) on the trajectory of the worm behavior. From the above results, it was confirmed that the rattle phenomena at the unit and component levels have been reproduced.

As described above, using a simulation that reproduces the phenomena of the steering system makes it possible to estimate the impact force in each rattling section from the low-frequency vibration, which causes rattle noise. It also makes it possible to estimate the effects of the size of each looseness on the rattle phenomena and to examine the direction of countermeasures. For example, in this case, the magnitude of rattle vibration is found to be correlated with the X-direction speed of the worm, and improvement of support stiffness of the worm to control its X-direction velocity is effective as a countermeasure for the rattle phenomena.

In the future, a simulation technique that can predict actual rattle noise including radiating surface in addition to the low-frequency vibration, impact source, and transfer path for inputs, will be built.

6. Summary

In this paper, examples of measurement and analysis for rattle noise and operating noise, which are particularly problematic among various NV phenomena of steering systems, have been introduced. In order to take appropriate countermeasures for NV phenomena of steering systems quickly, it is essential to specify the mechanisms of impact source, transmission, and radiation accurately. Moreover, it is essential to build and apply suitable measurement and analysis methods for each case. In order to predict NV performance at the design stage to prevent NV problems, a simulation model must be built based on physical phenomena with its validity assured by experimental verification.

For these issues, further study will be performed to improve NV measurement and analysis technologies for steering systems.

References

1) Onosokki, "Analysis Function Option (Time Frequency Analyzer) OS-0263 Instruction Manual (2.10), 5–11.
2) K. Tatebayashi, S. Teshima, and Y. Hasegawa, "Introductory MT system," (2014) 109–125, JUSE Press.

Masayuki Kanatsu

Development of Long Life Ball Screw using Material with High Retained Austenite Amount γ_R for High-Load Drive

Masahiro Ueda
Industrial Machinery Linear Technology Center, NSK Ltd.
Naruaki Abe
Industrial Machinery Bearing Technology Center, NSK Ltd.
Naoki Kawata
Industrial Machinery Linear Technology Center, NSK Ltd.
Hideyuki Hidaka
Core Technology R&D Center, NSK Ltd.

Abstract

Service life of ball screws for high-load drive is typically determined by rolling fatigue failure of screw shaft and/or nut raceways. For well lubricated, properly installed ball screws, failure usually results from damage originating on raceway surfaces due to sliding friction in ball-raceway contact because of the structure of ball screws (*e.g.*, helical raceway and ball recirculation system), eventually forming “peeling” or “flaking” damage structures on raceway surfaces. The authors investigated failures of conventional ball screws using life test data. As a result, the authors developed guidelines for improving durability considering the mode of failure of the ball screw. To extend the life of the ball screw, it is effective to increase the retained austenite amount γ_R of the material. It can be estimated how much to increase γ_R for each part of the ball screw by considering ball load distribution and number of stress cycles. Based on the above, new ball screws were fabricated and durability testing was conducted under high load conditions. The rated life L_{10}, indicating the estimated time at which 10% of a population of ball screws made with high-γ_R materials will have failed, was more than three times that of the conventional products.

Keywords

ball screw, retained austenite, long life, injection molding machine, press machine

Partially revised and reprinted from the *Journal of the Japan Society for Precision Engineering*, Vol. 85, No. 10, M. Ueda, N. Abe, N. Kawata, and H. Hidaka, Development of long life ball screw using material with high retained austenite amount γ_R for high-load drive, 896–903, Copyright (2019), with permission from the Japan Society for Precision Engineering.

1. Introduction

Ball screws have been used since the 1960’s as linear actuators of high-precision positioning tables in machine tools and semiconductor manufacturing equipment. Today, ball screws are also used to provide driving force for applications that require high thrust, capitalizing on the high power conversion efficiency of the ball screw. A representative high-thrust application is the electric injection molding machine. Ball screws are used to actuate an injection unit to feed molten resin into the mold and to actuate a clamping unit to tighten the mold. The ball screw for the injection unit is subject to high-load drive of up to about 100–150 tons.

In recent years, electric injection molding machines with injection speed exceeding 1 000 [mm/s] have been developed in order to be capable of molding thin-walled precision parts such as liquid crystal panel light guide plates and battery cases for smart phones and small tablet PCs. However, recently, development leading to improvement in injection speed has been stagnating, and resin molding of automotive parts has attracted attention as a technique to facilitate electrification and weight reduction of automobiles. Also, in the field of daily necessities such as food containers, from the perspective of cost reduction, high cycle rate is actively being pursued to improve productivity[1].

In response to technological trends toward productivity improvement and diversification of molded parts produced in electric injection molding machines, it is important to improve the load carrying capacity and extend the rated life of the ball screw for high-load drive. Conventionally, in order to extend the life and to improve the load carrying capacity of the ball screw, designs were optimized by increasing ball diameter, increasing the number of loaded balls, and making the radius of raceway groove close to ball radius. However, when the ball screw is operated at high speed, the kinetic energy of the ball is significantly increased because the mass and the velocity simultaneously increase. As a result, the impact on ball circulation parts becomes more severe and the noise level increases[2]. Moreover, abnormal heat generation due to increased sliding friction and early failure due to overriding the contact ellipse to the raceway groove shoulder are concerned. Inaba et al[3]. and Miyaguchi et al[4]. have optimized the arrangement of the ball recirculation circuit in order to equalize the ball load distribution and reduce maximum load born by any single ball, thereby achieving an extension of fatigue life. However, in consideration of modern development trends of injection molding machines, attempting to achieve long life through such conventional design methods will result in the size of the ball screw becoming too large for typical machine size.

By contrast, in order to extend the rolling fatigue life and to improve the load carrying capacity of the rolling bearing, optimization and advancement of the bearing material and its heat treatment technology have been achieved[5–11]. The above has been contributed from distinguished analyzing the characteristics and forms of rolling failure under various conditions of use, such as applied load, operating speed, lubrication and temperature. Shimoda et al[12–15]. clarified the characteristics and form of rolling fatigue failure in ball screw based on the life test. However, the applied load, operating speed, and ball screw specifications in this life test are different from those in today’s electric injection molding machines.

Therefore, in order to develop the ball screw for high-load drive with long life and improved load carrying capacity by the advancement of materials and heat treatment technology, we conducted the life tests under the conditions equivalent to the actual molding machine. From the analysis of the life test results, the development guideline was to increase the amount of retained austenite γ_R while keeping the surface hardness suitable for ball screw material. We also investigated which part of the ball screw should be strengthened in order to improve durability with considering ball load distribution and number of stress cycles. Finally, we produced full-scale prototypes of our newly developed ball screw for high-load drive, and conducted durability tests under high load conditions.

2. Durability Test of Ball Screw for High Load Drive

In ball screws used in machine tools, it has been reported that positioning accuracy declines due to wear of the raceway surface and ball surface caused by severe poor lubrication conditions or contamination with foreign matter. On the other hand, in ball screws used for high-load drive applications, such as electric injection molding machines, failures due to surface wear rarely occur. Failures usually occur due to peeling or flaking of the raceway or ball surfaces after prolonged use. Once peeling or flaking occurs on a part of the raceway surface, the damage rapidly propagates along the raceway surface even during shorter operation periods, ultimately resulting in the ball screw breaking down.

In this paper, failure mechanisms of ball screws for high-load drive are evaluated based on the analysis of rolling fatigue failure of rolling bearings. In addition, the influence of ball load distribution and number of stress cycles on rolling fatigue failure was analyzed using conventional ball screw fatigue life tests.

2.1 Failure analysis of ball screw

Fig. 1 shows a summary of modes of rolling fatigue failure in rolling bearings based on the origin of rolling contact fatigue. It is well known that failure mode depends on lubrication condition and is classified into “subsurface originated type” and “surface originated type”[16, 17]. The subsurface originated type usually occurs under sufficient lubrication condition. Maximum shear stress generated by rolling contact exists at a given depth below the surface. The material inevitably contains faults such as non-metallic inclusions. Non-metallic inclusions located in highly stressed regions enhance the metal fatigue process and become the origin of flaking. On the other hand, the surface originated type usually occurs in conditions with insufficient oil film thickness due to poor lubrication condition or contamination with debris. In this case, higher tangential force acts on the raceway surface due to sliding between rolling element and raceway surface. As a result, metal fatigue progresses on the material surface and cracks are generated. Especially, in the case where a dent is present on the raceway surface, metal fatigue is accelerated locally at the edge of the dent due to stress concentration at that site.

Analysis of a large number of ball screw life tests reveals that the high load life testing of conventional ball screws frequently results in surface originated type flaking as shown in Fig. 2 (a) and (b). Fig. 2 also shows the test conditions of the ball screw. In Fig. 2 (a), many small flaking damage structures are observed on the surface of raceway similar to the peeling shown in Fig. 1. Near the site of small flaking damage structures, grinding marks disappear due to wear. We confirmed that resin spacer pieces were not inserted between the balls in the broken ball screws from the life tests. These results suggest that a large tangential force is acting on the raceway surface due to relatively lower roughness of ball and sliding friction between the adjacent balls, and this results in promoting fatigue of the surface of raceway. In general, the raceway surface roughness of the ball screw is inferior to that of ordinary rolling bearings, so this phenomenon is thought to occur easily in ball screws.

In the case of Fig. 2 (b), typical flaking is occurring adjacent to the dent. This is quite similar to ball bearing flaking. The dent also affects the site of stress localization and fatigue is promoted at the edge of dent. Compared with ball bearings, lubricant of ball screws is easily contaminated by debris due to the sliding motion of the nut. In addition, the helical raceway structure of shaft and nut forces the balls to move perpendicular to the grinding marks. Moreover, it is known that, in general, ball screws suffering from surface originated type flaking have shorter life than balls screws suffering from subsurface originated type flaking. Accordingly, due the characteristics of ball screws, damage typically realizes as surface originated type flaking on the raceway.

2.2 Failure Location in Ball Screw

In the previous section, the mode of failure of high load drive ball screw was investigated. As a result, it was found that primary mode of failure was peeling originated from the surface. It was also estimated that this phenomenon is due to ball sliding and abrasive particle contamination along with the structural characteristics of the ball screw. Therefore, in this section, the authors analytically investigated the influence of load stress and number of stress cycles on rolling fatigue failure of the raceway surface in ball screws for high-load drive.

In ordinary ball screws, because of the presence of a ball recirculation circuit, the effective thread turns ratio is often a fraction such as $\zeta = 2.5$ or $\zeta = 3.5$. As a result, when thread turns ζ_1 on the same phase side as the ball recirculation circuit is compared with thread turns ζ_2 on the opposite phase side, there is a difference of $\zeta_2 - \zeta_1 = 1.0$ turns. With the difference in the number of thread turns between the upper and lower phases, as shown in Fig. 3, ball load distribution in the case of $\zeta = 2.5$ is locally maximal at the location of $x = \pm\, l/2 = \pm\, 5$ [mm] which is shifted by half lead from the center of the load zone. When life tests were conducted under the load condition shown in Fig. 3, the number of test samples on which the first rolling fatigue failure occurred on the nut raceway was $N = 12$. As a result of investigating these nut raceway surfaces, as shown in Fig. 4, the location of flaking failure was biased to the region including the location of $x = \pm\, 5$ [mm] where the load distribution was maximal. Therefore, it is found that rolling fatigue failure of the ball screw correlates with the magnitude of load stress.

Fig. 5 shows the relation between the number of stress cycles on the raceway surfaces of the screw shaft and the nut, and the length of the stressed raceway in one-way strokes of the ball screw. In the ball screw, the number of stress cycles u_N on the nut raceway surface increases

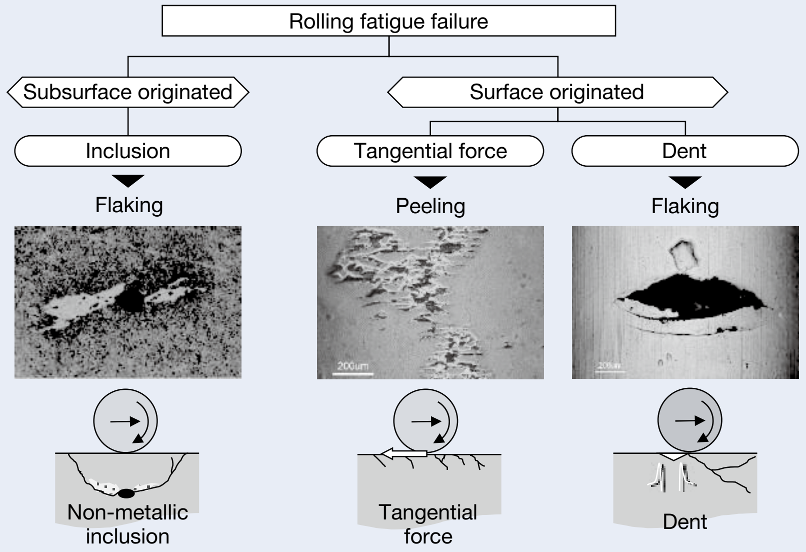

Fig. 1 Failure type of rolling fatigue in rolling bearing

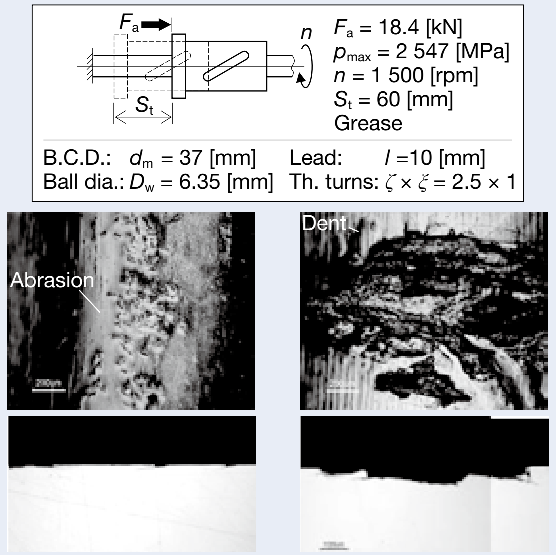

(a) Peeling due to tangential force (b) Flaking due to dent

Fig. 2 Rolling fatigue failure in ball screw for high-load drive

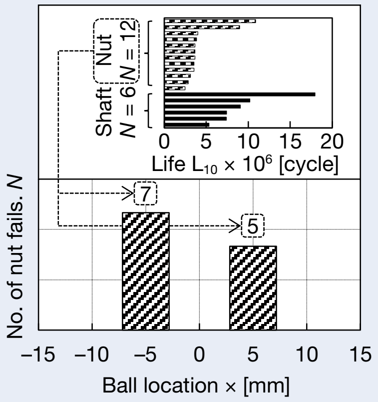

Fig. 4 Relation between number of nut failures and ball location

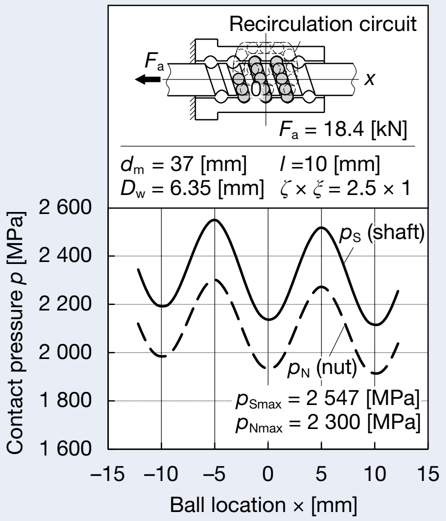

Fig. 3 Ball load distribution

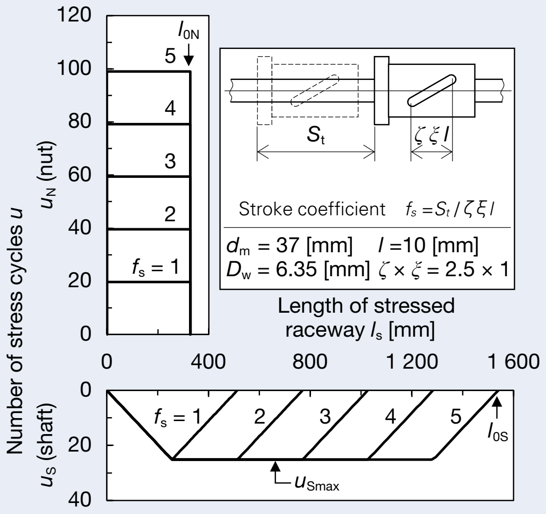

Fig. 5 Relation between number of stress cycles and length of stressed raceway

in proportion to the stroke S_t, and the length of stressed raceway l_{0N} becomes constant. On the other hand, in the screw shaft, the length of stressed raceway l_{0S} increases in proportion to the stroke S_t, but when the S_t is larger than the effective nut length $\zeta\xi l$, the maximum number of stress cycles u_{Smax} is kept constant. Calculating u_S and u_N with $f_s = S_t/\zeta\xi l = 2.4$ in the life test resulted in $u_S = 25.2$ and $u_N = 45.7$, respectively. Thus, the raceway of the nut is stressed about twice as much as that of the screw shaft.

Among the life test data, the number of samples which experienced failure at the screw shaft raceway is $N = 6$, and at the nut raceway is $N = 12$. Therefore, it is found that the failure location correlates with the number of stress cycles, although the influence due to fluctuation of quality cannot be excluded.

Note that, u_{Smax} and u_N are expressed as the following equations, respectively[15).

$$\left.\begin{aligned} u_{\mathrm{Smax}} &= Z\frac{S_t}{\zeta\xi l}\left(1-\frac{d_S\cos\gamma_m\cos\gamma_{\Sigma S}}{2d_m\cos\gamma_S}\right)\\ S_t &= \begin{cases} S_t & (f_s<1)\\ \zeta\xi l & (f_s\geq 1)\end{cases}\end{aligned}\right\} \quad \cdots\cdots\cdots\cdots (1)$$

$$u_N = Z\frac{S_t}{\zeta\xi l}\frac{d_S\cos\gamma_m\cos\gamma_{\Sigma S}}{2d_m\cos\gamma_S} \quad \cdots\cdots\cdots\cdots (2)$$

Also, l_{0S} and l_{0N} are obtained as follows.

$$\left.\begin{aligned} l_{0S} &= \frac{\pi d_S}{\cos\gamma_S}\left(\zeta+\frac{S_t}{l}\right)\\ l_{0N} &= \frac{\pi d_N}{\cos\gamma_N}\zeta\end{aligned}\right\} \quad \cdots\cdots\cdots\cdots (3)$$

Where, Z is the number of loaded balls, γ_m is the lead angle of ball center, d_S and d_N are the diameters of helix passing through the contact point between the ball and the screw shaft and the nut raceways respectively, γ_{RS} and γ_{RN} are the lead angles of the contact points respectively, and $\gamma_{\Sigma S}$ is the angle between the ball revolution direction and the direction of the screw shaft raceway.

3. Improvement of Durability for Ball Screw Material

In order to improve the durability of the material surface, it is effective to increase the retained austenite amount γ_R in the material surface layer. Murakami et al[18). developed a technology that greatly improves the rolling fatigue life in rolling bearings under contaminated conditions by increasing γ_R of the material surface. This is because the plastic deformation capability of the metal structure is improved by the high-γ_R, so that the local progress of surface fatigue can be delayed due to the decrease in stress concentration at the edge of dents. Furthermore, in the material with high-γ_R, the phase transformation of microstructure occurs in the process of surface and subsurface fatigue, so the fatigue progress can be delayed.

3.1 Extension of rolling fatigue life by an increase in γ_R

The increase in γ_R of the material is effective to delay rolling fatigue due to tangential force across the entire surface and delay rolling fatigue due to local stress concentration at the surface around dent edges. Factors in both fatigue mechanisms can be attributed to stress acting on the material surface[19). However, when the γ_R of the material is excessively increased, the surface hardness is lowered, and the durability conversely deteriorates. Therefore, in order to improve the durability of material surface by balancing high-γ_R and appropriate hardness, rolling fatigue life and surface hardness for the specimens with various γ_R were tested.

For the evaluation of rolling fatigue life of material surface, the authors conducted a "ball-rod life test" on various γ_R specimens. The test diagram and results are as shown in Fig. 6. By using balls without surface finish polishing inserted between the rod and the outer ring, the tangential force between the balls and the rod surface is increased. By this test method, peeling failure due to rolling fatigue on the material surface can be reproduced. Fig. 6 indicates that the material surface durability improves in proportion to the ratio γ_R/γ_{R0} to the average amount γ_{R0} of retained austenite amount in the materials of conventional ball screws. For instance, in the case of $\gamma_R/\gamma_{R0} = 2$, the rated life L_{10}, at 10% probability of failure, is three times as long or longer compared with the conventional material.

Then, the relationship between γ_R and the hardness of the material surface is shown in Fig. 7. From Fig. 7, it is found that while satisfactory surface hardness of Vickers hardness $H_v = 700$ or more can be obtained in the region of $1 < \gamma_R/\gamma_{R0} < 3.5$, the hardness decreases in other regions. Therefore, in order to achieve a longer life of the ball screw by increasing the γ_R of its material, it is necessary to design the quality of the heat treatment such that $1 < \gamma_R/\gamma_{R0} < 3.5$. However, since the quality characteristics of the heat treatment in conventional products are different from the test specimens, the hardness is appropriate in the region of $\gamma_R/\gamma_{R0} < 1$.

In addition, the effect on the rolling fatigue due to stress concentration at the edges of dents in the high-γ_R material was analytically evaluated. Chiu et al[20). studied a flaking mechanism originating from surface cracks caused by defects such as scratches and dents, and revealed that the rolling fatigue life due to surface cracks depends on stress concentration around the defect. According to this study, the relationship between the contact pressure p_0 and the maximum shear stress τ_c on the raceway surface is expressed as follows:

$$\frac{\tau_c}{p_0} = a_1 C_0^{a_2} \quad \cdots\cdots\cdots\cdots (4)$$

where, $a_1 = 0.22$, $a_2 = -0.24$. Also, C_0 is the furrow severity parameter, which is determined by the following equation using the radius r of the dent edge and the distance $2c$ between the edges.

$$C_0 = \frac{\pi^2 p_0 r}{E' c} \quad \cdots\cdots\cdots\cdots (5)$$

And E' is the reduced Young's modulus of elasticity, for steels, $E = 20\ 600$ [MPa] and $\nu = 0.3$, then $E' = 35\ 560$ [MPa].

Therefore, the relationship between τ_c and p_0 for the high-γ_R material and the conventional material is as shown in Fig. 8. From Fig. 8, it is confirmed that the τ_c of $\gamma_R/\gamma_{R0} = 2$ is decreased by 23% as compared with the conventional material, since the edge of dent becomes smooth when the γ_R increases[21). In other words, rolling fatigue life due to stress concentration at edge of dent can be extended by increasing the γ_R on the material surface.

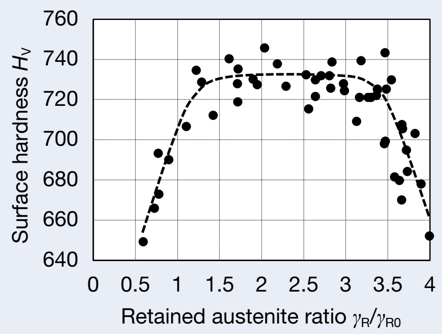

Fig. 7 Relation between amount of retained austenite and surface hardness for ball screw materials

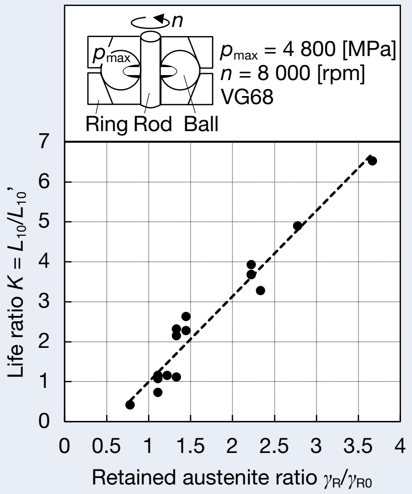

Fig. 6 Relation between amount of retained austenite and L10 life for ball screw materials

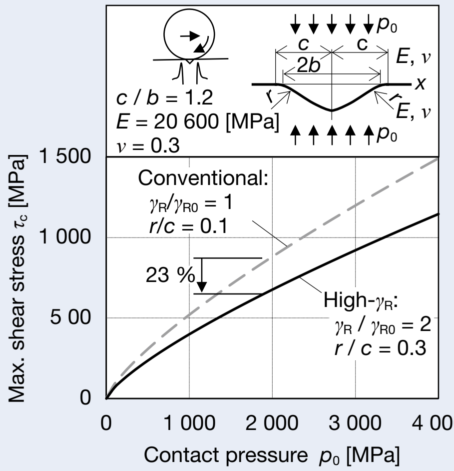

Fig. 8 Maximum share stress at dent edge to contact pressure for ball screw materials

3.2 Evaluation of optimal γ_R to ball screw parts

In Section 3.1, the following was revealed by increasing the γ_R of the material. (1) Since the phase transformation occurs in the fatigue process of surface and subsurface, the fatigue progress can be delayed. (2) Since stress concentration at dent edges decreases due to the improvement of plastic deformability of the metal structure, the fast fatigue progress at dent edge can be delayed. As using the above effects, we attempted to improve durability of the ball screws for high-load drive.

In order to obtain high-γ_R and appropriate hardness for the long size material of a ball screw, advanced heat treatment control technique is required. For example, when performing carburizing quenching for heat treatment of a ball screw, productivity is more advantageous if screw shaft and nut are simultaneously introduced into a carburizing furnace and processed. However, since the screw shaft and the nut are greatly different in size and shape, it is not easy to control the heat treatment to achieve both an increase in γ_R and appropriate hardness. Therefore, from the viewpoint of productivity, it is considered to be most reasonable to separately perform the heat treatment so that each of the screw shaft and the nut becomes the optimum quality in terms of higher γ_R and appropriate hardness. Therefore, in this section, as in Section 2.2, we attempted to estimate the optimum γ_R for the screw shaft and nut based on the analysis results of the contact pressure and the number of stress cycles.

From the linear regression for the plotted data in Fig. 6, the changing ratio K of rolling fatigue life of the surface originated failure due to the increase in γ_R is expressed as follows.

$$K = 2.14\,\frac{\gamma_{R}}{\gamma_{R0}} - 1.14 \qquad \cdots\cdots\cdots\cdots (6)$$

Taking into consideration the failure location of the nut due to the ball load distribution, the rolling fatigue life of the raceway surface is proportional to the ninth power of the contact pressure. Further, the frequency of failure occurrence in the screw shaft and the nut to be made is proportional to the number of stress cycles. Therefore, the changing ratios K_S and K_N for the raceway surfaces of the screw shaft and the nut can be expressed by the following equation.

$$\frac{K_N}{K_S} \propto \left(\frac{p_N}{p_S}\right)^9 \frac{u_N}{u_S} \qquad \cdots\cdots\cdots\cdots (7)$$

From the above equation, the relation between the life ratio K_N/K_S and the stroke coefficient f_s is shown in Fig. 9. The dots in Fig. 9 were obtained from 20 models of ball screws actually used on the electric injection molding machine. Also, the plots in the region of $f_s < 2$ represent the injection unit application, and the plots in $f_s > 2$ represent the mold clamping unit application. In the injection unit application, the number of stress cycles on the nut raceway is smaller than on the screw shaft. As a result, the influence of the contact pressure is dominant to the rolling fatigue life and then K_N/K_S becomes large. On the other hand, in the clamping unit application, K_N/K_S decreases as the number of stress cycles increases on the nut raceway. Furthermore, when f_s exceeds 4.8, K_N/K_S is less than 1.

According to the equation (6) and Fig. 9, the life change rates (K_S and K_N) can be estimated from the amounts of retained austenite (γ_{RS} and γ_{RN}) of the screw shaft and the nut by the following formulas.

$$\left.\begin{aligned} \frac{\gamma_{RS}}{\gamma_{R0}} &= \frac{K_S + 1.14}{2.14} \quad (\text{for shaft}) \\ \frac{\gamma_{RN}}{\gamma_{R0}} &= \frac{K_N + 3.74\,f_s^{-0.8}}{7.02\,f_s^{-0.8}} \quad (\text{for nut}) \end{aligned}\right\} \qquad \cdots\cdots\cdots\cdots (8)$$

Fig. 10 shows the retained austenite amounts on raceway surfaces of the screw shaft and the nut at various life change rates. As shown Fig. 10, the required amount of screw shaft γ_{RS} is constant with respect to f_s. However, the required amount of nut γ_{RN} increases as f_s increases. For instance, in the case of $f_s = 2$, if the screw shaft γ_{RS} is increased to about 1.5 times the conventional γ_{R0}, the screw shaft life becomes $K_S = 2$. On the other hand, even though the nut γ_{RN} is equivalent to the γ_{R0}, the nut life is $K_N = 2$. In other words, if it is assumed to be used only for injection unit where $f_s < 2$, only γ_{RS} needs to be increased compared with γ_{R0}. But, assuming the use in a mold clamping unit where $f_s > 2$, γ_{RN} can be lower than γ_{RS}, but it needs to be higher than γ_{R0}.

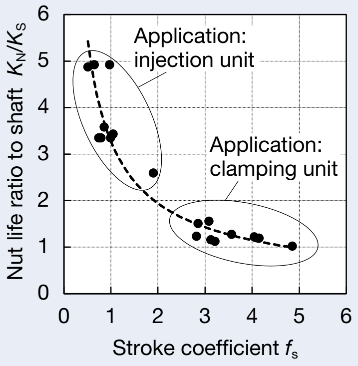

Fig. 9 Relation between nut life ratio to shaft and stroke coefficient (for 20 models)

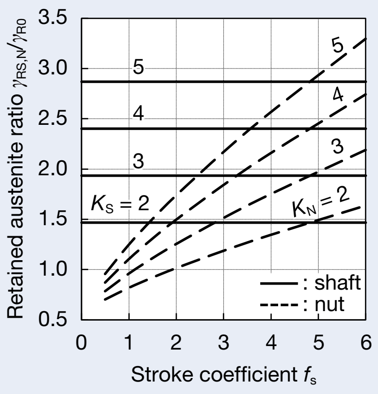

Fig. 10 Retained austenite amount of ball screw material required according to nut stroke

4. Evaluation of Rated Life of Ball Screw using High-γ_R Materials

In order to evaluate the rated life of a ball screw using high-γ_R materials, ball screws were fabricated with a model and size used in real-world applications and assuming mass production. Fig. 11 shows the specifications of the ball screw for the high-load durability test. The retained austenite amounts on the raceway surfaces of the screw shaft and the nut were $\gamma_{RS}/\gamma_{R0} = 2.6$ and $\gamma_{RN}/\gamma_{R0} = 2.2$, respectively. From equation (8), the life change rate K_S of fatigue life for the screw shaft becomes 4.4 times larger than the conventional product. On the other hand, for the nut, the life change rate K_N becomes 6.7 times when $f_s = 2$, and K_N becomes 3.3 times when $f_s = 4.8$.

Test conditions are shown in Table 1. Given development trends such as increasing thrust in electric injection molding machines to cope with diversification of molded parts, there is a high possibility that the driving load of ball screws will increase. In the newly developed product, durability is improved by using the high-γ_R material. Accordingly, the axial load when evaluating the rolling fatigue life was set to $F_a = 300$ [kN], which is the allowable axial load of ball screws of the chosen model one size larger than the high-γ_R material test ball screws. The contact pressure distribution between the balls and the raceway surface of the screw shaft in the test ball screw is as shown in Fig. 12. From Fig. 12, the maximum contact pressure between the balls and the raceway surface is $p_{Smax} = 2\,820$ [MPa]. Fig. 13 shows a high-load durability test machine used for fatigue life evaluation. Two ball screws for testing and loading are arranged opposite to each other. Then, when the load torque T_L is applied to the screw shaft of the load ball screw, the axial load F_a is generated against the nut moving direction of the test ball screw.

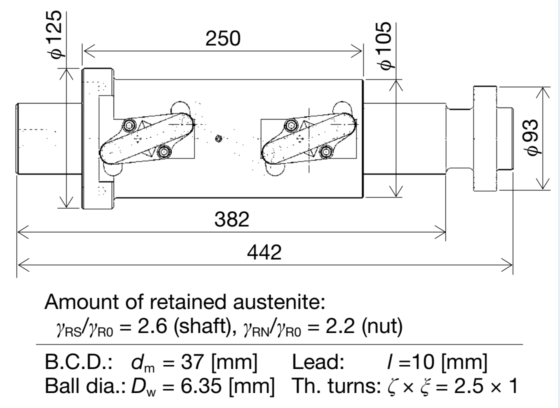

Fig. 11 Specifications of ball screw for high load durability test

Table 1 Operating conditions for high load durability test

Axial load, F_a	300, kN
Shaft rotation speed, n	500, rpm
Stroke S_t	80, mm
Lubrication · Thickener · Consistency · Base oil kinematic viscosity (40°C)	Grease · Lithium soap base · 303 · 99, mm²/s
Nut temperature	≤ 80°C

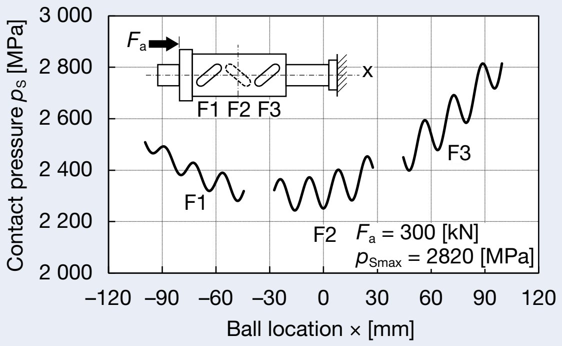

Fig. 12 Ball load distribution for high load durability test

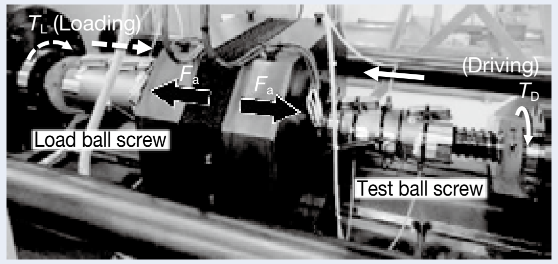

Fig. 13 Testing machine for high load durability test

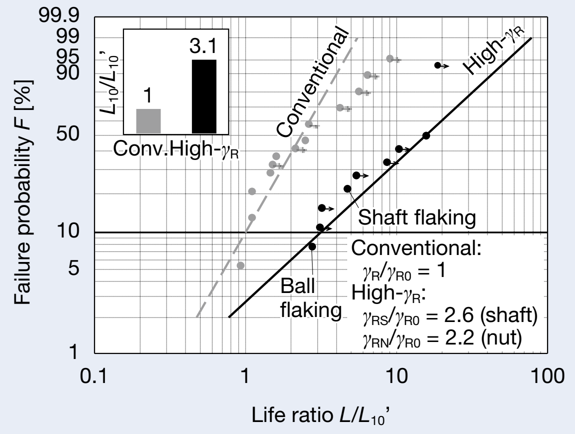

Fig. 14 Weibull distribution for high load durability test

The Weibull distribution for the fatigue life data of the nine ball screws with the material of the screw shaft and the nut increased to γ_R is as shown in Fig. 14. In Fig. 14, the horizontal unit represents the ratio of the rated life L_{10}' with 10% probability of failure estimated from the Weibull distribution for the fatigue life data of the thirteen conventional ball screws. Therefore, it is confirmed that the rated life L_{10} of the ball screw using high-γ_R materials is improved 3.1 times as compared with the conventional rated life L_{10}'. The minimum life (L/L_{10}' = 2.9) in the ball screw using the high-γ_R materials was due to fatigue failure of the ball surface. On the other hand, in the conventional ball screws, the initial failure in the region of $L/L_{10}' \leq 2.9$ was due to rolling fatigue on the raceway surface of the screw shaft or of the nut. In conventional ball screws, since the durability of the raceway surface is lower than that of the ball surface, the initial failure portion is biased toward the raceway surface. The reason is assumed to be that the number of stress cycles on the ball surface is fewer than the raceway surface due to the evacuation of balls to the ball recirculation circuit away from the load zone. Therefore, it can be estimated that the service life of the ball screws with high-γ_R materials is determined by the fatigue failure of the ball surface due to relatively lower ball durability, because the durability of the raceway surface is improved by increasing the γ_R.

In the ball screw with high-γ_R materials, the minimum life due to rolling fatigue failure on the raceway surface of the screw shaft was L/L_{10}' = 4.9. This result is reasonable compared to the change ratio of change K_S of fatigue life for the screw shaft estimated by substituting the amount of retained austenite γ_{RS} into the equation (8). In addition, in the ball screw with high-γ_R materials, initial fatigue failure did not occur on raceway surface of the nut. Therefore, although the amount of data is not quite large enough, it can be indicated that the relationship between the amount of retained austenite γ_R and the change ratios of fatigue life K_S or K_N shown in this report is appropriate.

5. Summary

In response to trends toward productivity improvement and diversification of molded parts in modern electric injection molding machines, we developed a new long life ball screw for high-load drive. By analyzing the mode of failure of rolling fatigue on the raceway surface in high-load life tests, it was concluded that increasing γ_R on the material surface was effective to relieve metal fatigue and delay occurrence of cracks from the surface. Fatigue life test and hardness test were conducted on specimens with various γ_R. Furthermore ball load distribution and number of stress cycles on the raceway surface of the screw shaft and the nut were investigated analytically. As a result, we derived an estimation method of γ_R in raceway surfaces of the screw shaft and the nut necessary for maximizing ball screw life and heat treatment efficiency. In addition, according to the life test at a load higher than the conventional level, we confirmed that the rated life L_{10} at 10% probability of failure of the ball screws using high-γ_R materials is more than three times longer than the conventional products.

NSK has commercialized the S-HTF Series of long-life ball screws for high-load drive by applying the technology described in this paper, and which many of our customers are now using. We hope that the S-HTF Series will be well received throughout the market and contribute to the further development of industrial machinery.

References

1) H. Saito, "Technical Trend of Ball Screws for Electric Injection Molding Machine," Bearing&Motion-Tech, 9 (2017) 21–23. [in Japanese]
2) H. Shimoda, "Technical Trends in Ball Screws," Proc. 2009 JSPE Spring Meeting, (2009) 417–418. [in Japanese]
3) Y. Inaba and S. Ito, "A Study on the Life of the Ball Screw for Electric Injection Molding Machines," Journal of the JSPE, 65, 6 (1999) 805–809. [in Japanese]
4) K. Miyaguchi, M. Ninomiya, S. Nakamura, D. Maruyama, and Y. Kakino, "Life Extension of Ball Screws by Even Load Distribution in Heavy Duty Drive System," Journal of the JSPE, 67, 2 (2001) 217–221. [in Japanese]
5) K. Furumura, Y Murakami, and T. Abe, "The Development of Bearing Steels for Long Life Rolling Bearings Under Clean Lubrication and Contaminated Lubrication," in Creative Use of Bearing Steels, ed. J. Hoo, ASTM International, STP1195 (1993) 199–210.
6) K. Ohkuma and M. Koshigaya, "High-performance Ball Bearings for Automotive Alternator Applications," NSK Technical Journal, No.4 (1998) 30–36."
7) K. Furumura, T. Abe, and Y. Murakami, "Progress in Through-Hardening Bearing Steels: User's Experience," in Bearing Steels, ed. J. Hoo and W. Green, ASTM International, STP1327 (1998) 249–264.
8) K. Furumura, Y. Murakami, and T. Abe, "Case-hardening Medium Carbon Steel for Tough and Long Life Bearing under Severe Lubrication Conditions," in Bearing Steels, ed. J. Hoo and W. Green, ASTM International, STP1327 (1998) 293–306.
9) S. Tanaka, K. Ueda, N. Mitamura, and M. Oohori, "The Development of an Austenitic Stainless Steel Bearing with High Corrosion Resistance and High Nonmagnetic Property," Journal of the ASTM International, 3, 9 (2006) 1–7.
10) H. Komata, Y. Iwanaga, T. Ueda, K. Ueda, and N. Mitamura, "Enhanced Performance of Rolling Bearings by Improving the Resistance of Rolling Elements to Surface Degradation," in Bearing Steel Technologies, ed. J. Beswick, ASTM International, STP1580 (2015) 272–290.
11) P. Xiangduo, Y. Shimizu, and N. Mitamura, "Long Life Bearing Technologies on Material Aspect," Proc. CIST2008 & ITS-IFToMM2008, (2009) 932–933.
12) H. Shimoda and M. Izawa, "Study of Fatigue Life of Ball Screw (1st Report): Trial Construction of Life Testing Apparatus and Fatigue Life," Journal of the JSPE, 52, 2 (1986) 326–331. [in Japanese]
13) H. Shimoda and M. Izawa, "Study of Fatigue Life of Ball Screw (2nd Report): Fatigue Life and Growing Characteristics of Fatigue Failure of Preloaded Ball Screw with Double Nut," Journal of the JSPE, 52, 8 (1986) 1431–1436. [in Japanese]
14) H. Shimoda and M. Izawa, "Study of Fatigue Life of Ball Screw (3rd Report): The Influence of Use of Spacer Ball and Raceway Hardness on Fatigue Life," Journal of the JSPE, 53, 1 (1987) 59–64. [in Japanese]
15) H. Shimoda and M. Izawa, "Study of Fatigue Life of Ball Screw (4th Report): Theory of Ball Screw Life," Journal of the JSPE, 53, 8 (1987) 1195–1202. [in Japanese]
16) T. Ueda and N. Mitamura, "Mechanism of Dent Initiated Flaking and Bearing Life Enhancement Technology under Contaminated Lubrication Condition Part I: Effect of Tangential Force on Dent Initiated Flaking", Tribology International, 41, (2008) 965–974.
17) T. Ueda and N. Mitamura, "Mechanism of Dent Initiated Flaking and Bearing Life Enhancement Technology under Contaminated Lubrication Condition Part II: Effect of Rolling Element Surface Roughness on Flaking Resulting from Dents", Tribology International, 42 (2009), 1832–837.
18) Y. Murakami, N. Mitamura, and A. Maeda, "Study on Improvement of Material Properties under Debris Contaminated Lubrication," Proc. International Tribology Conference, (1995) 1393–1398.
19) H. Hidaka, K. Ueda, and N. Mitamura, "Rolling Contact Fatigue Type Analysis of Rolling Bearing by XRD and TEM," Materials Science Forum, 706–709 (2012) 1679–1684.
20) Y. P. Chiu and J. Y. Liu, "An Analytical Study of the Stress Concentration Around a Furrow Shaped Surface Defect in Rolling Contact," Transaction of the ASME, 92, (1970) 258–263.
21) Y. Murakami, Y. Matsumoto, and K. Furumura, "Study of Long Life Bearing Materials," Proc. Tribology Conference, (1988) 297–300.

Masahiro Ueda

Naruaki Abe

Naoki Kawata

Hideyuki Hidaka

Improved Reliability of Roller Guides for Machine Tools

Kenta Nakano
NSK Ltd.

Abstract

Roller guides are used for machine tools due to their higher rigidity and durability over ball guides. Moreover, the operating environment for roller guides in machine tools is becoming more severe every year due to the improved productivity of machines, which increases the need for roller guides that are highly reliable.

Here we will explain some technologies that improve reliability in the RA/RB Series roller guides. By considering deformation of the slider and load distribution for the roller contact, we confirmed the actual durability above the calculated fatigue life. Additionally, we applied abrasion-resistant material to the seal lip along with high resistance to intrusion of foreign particles, allowing for long-term performance free of dust.

1. Introduction

Until the 1970s, many machine tools, such as those in machining centers and NC lathes, used sliding guides. Ball-type linear guides, which have a small dynamic friction force and can be used in a wide range of speeds from high to low, became popular in the 1980s mainly in machining centers. Since 2000, the requirements of long life and high rigidity on linear guides have increased with the trend of high performance and high efficiency of machine tools such as multi-axis machining and combined machining. Therefore, the adoption of roller guides using rollers for a rolling element is increasing year by year (Figure 1). NSK released the LY Series in 1983 and the LA Series in 1997 as linear guides for machine tools. Both are the ball type. The roller guide RA Series, however, was released in 2004 because the use of roller guides started to spread in 2000. In 2010 we released the RB Series, which realizes assembly dimensions smaller than those specified in ISO/DIS12090-1.2 and enables low-center-of-gravity designs for feed mechanisms. Currently, we are expanding our line of highly dust-resistant seals for the RA/RB Series (Photo 1). This article introduces the RA/RB Series advantage and technology to improve reliability.

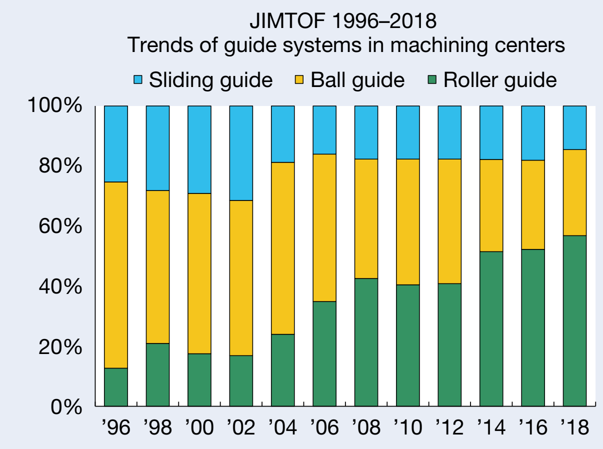

Fig. 1 Trends of guide systems on machining centers (NSK research)

Photo 1 Roller guides with highly dust-resistant V1 seals (right: RA35, left: RB35)

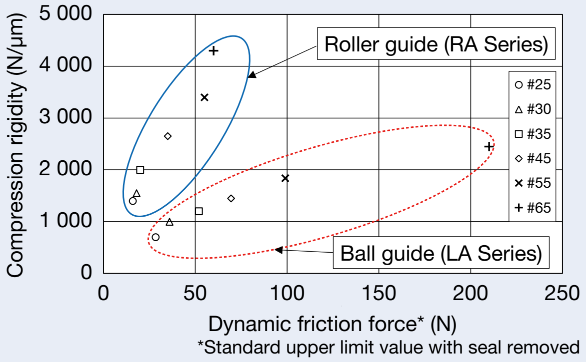

Fig. 2 Relationship between dynamic friction force and rigidity

2. RA/RB Series Advantage

For ball guides, dynamic friction force due to differential sliding caused by rotating radius differences with respect to the ball groove of the ball is unavoidable. On the other hand, since roller guides use a roller for a rolling element to form a line contact with a raceway surface, this differential sliding hardly occurs, and dynamic friction force can be reduced. Further, rigidity and load capacity are higher because of the large contact area of the line contact compared to a ball guide that forms point contacts between the ball and raceway surface. However, if load distributions in the contact portion between the roller and raceway surface are not uniform, skew may occur. Also, if the inclined part (crowning) provided on the roller end face is not appropriately shaped, local edge load may occur, resulting in an increase in dynamic friction force and a decrease in rigidity and load capacity.

In the RA/RB Series, the analytical technology of the roller and raceway surface cultivated by rolling bearing was applied to realize equalization of load distribution with consideration of the deformation of the main body of the roller guide by preload. As a result, more than 1.5 times more rigidity and less than 60% dynamic friction force than the ball guides for machine tools were achieved (Figure 2). In a machine tool, improvements such as in positioning accuracy are expected due to improvements in controllability.

3. Issues for Improvement of Reliability

The function of roller guides required by a machine tool is to maintain a predetermined motion accuracy over a long period. Therefore, to improve the reliability of roller guides, it is essential to minimize the circulation failure of a roller caused by accuracy deterioration by abrasion, fatigue by flaking, or contamination with foreign matter or coolant.

As described above, the RA/RB Series suppresses the slippery component and edge load by equalizing the load distributions of the roller and raceway surface, and they also have excellent high abrasion resistance. For example, in ball guides, when versatile lithium-based grease is used, it is known that fretting abrasion occurs in a relatively short time when a small-stroke motion equivalent to the ball diameter is performed. Therefore, anti-fretting grease, or the like, is recommended. The RA Series has been confirmed to have high abrasion resistance even in small-stroke motions equivalent to the roller diameter (Figure 3). Therefore, in an application with many small-stroke motions, such as mold processing machine, accuracy deterioration due to abrasion is less likely to occur, providing high reliability.

Also, for fatigue life, the RA Series has a higher load capacity than the ball guide, and through using a high load endurance test with a 50% load as per the dynamic load rating, calculated using international standard ISO 14728-1, an actual lifetime exceeding the rated fatigue life is confirmed (Figure 4). In addition, foreign matter such as processing powder and coolant may infiltrate into the slider in a machine tool, causing improper lubrication or abrasion and eventually damaging the recirculating parts.

In many machine tools, although the linear guide is protected by covers, such as bellows and telescopes, it is difficult to prevent coolant in the form of mist and fine processing powder such as graphite powder from intruding into the slider of a linear guide. Therefore, dust-resistant performance of the linear guides itself is the key to reliability of products.

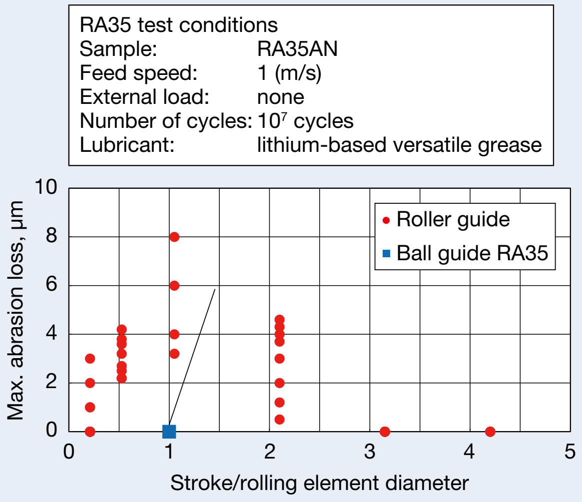

Fig. 3 Fretting performance

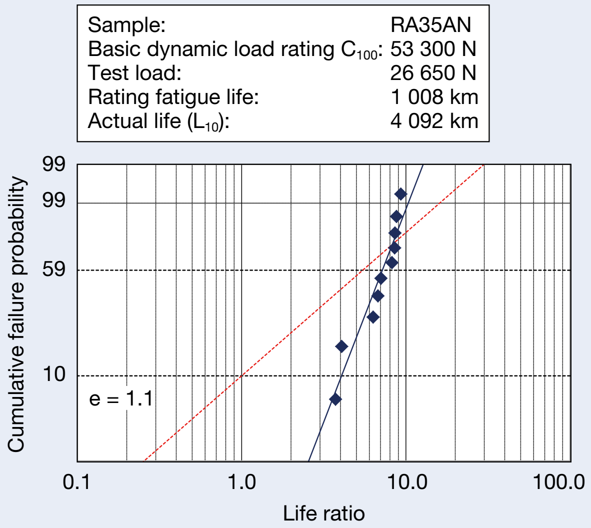

Fig. 4 High-load durability test results

4. RA/RB Series Seal Configuration

The main directions in which foreign matter infiltrate into roller guides are the two directions from the end face and the bottom of a slider (Photo 2). A typical seal configuration for the RA/RB Series includes end seals and inner seals for foreign matter infiltration from the slider end face (Figure 5). There are bottom seals for foreign matter infiltration from the slider bottom. In a roller guide, processing powder may accumulate in the mounting holes of the rail and infiltrate into the slider. The RA/RB Series are equipped with caps that close the mounting holes and a rail top cover over the entire upper surface of the rail (Photo 3).

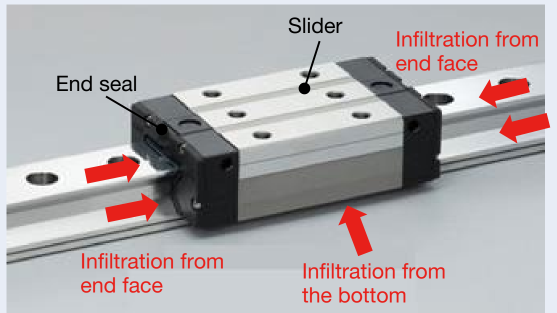

Photo 2 Infiltration of foreign particles

5. Developing a Highly Dust-Resistant V1 Seal and V1 Bottom Seal

In JIMTOF2018, many hybrid multifunction machines have been exhibited that combine metallic lamination molding or laser hardening that have evolved from conventional multifunction machines. In addition, machine tools for the aerospace industry are promoting technological development of high-speed cutting of difficult-to-machine materials, such as titanium alloys and nickel-based superalloys, by high-pressure coolant. In such new technologies, more foreign matter such as coolant, processing powder, or fumes may be dispersed, and so enhancing the dust resistance of roller guides is becoming increasingly important. NSK has thus developed the highly dust-resistant V1 seal and V1 bottom seal used in the RA/RB Series. This section introduces their configurations, designs, and related evaluation tests.

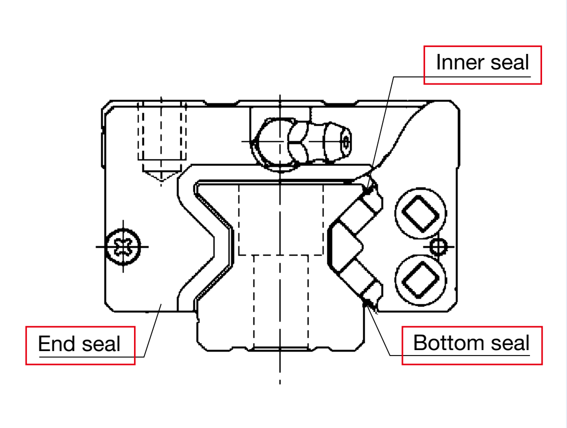

Fig. 5 Standard seals for the RA/RB Series


Cap for rail mounting hole

Rail top cover

Photo 3 Dust-resistant parts for the rail

5.1. Configuration of the seal

A highly dust-resistant V1 seal is affixed to the slider end face together with the lubrication unit NSK K1, a part that supports lubrication (Figure 6). The V1 bottom seal is a double seal structure mounted on the outside of the bottom seal and reinforces dust resistance (Figure 7).

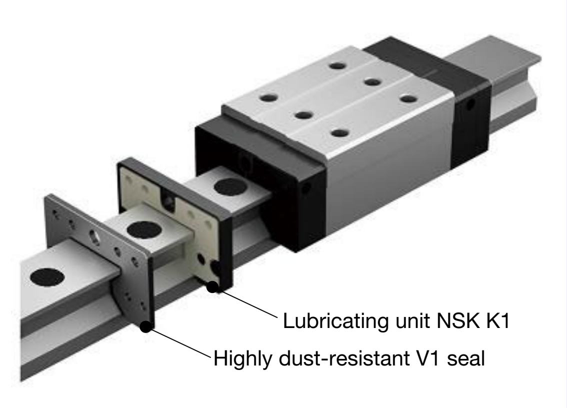

Fig. 6 Highly dust-resistant V1 seal

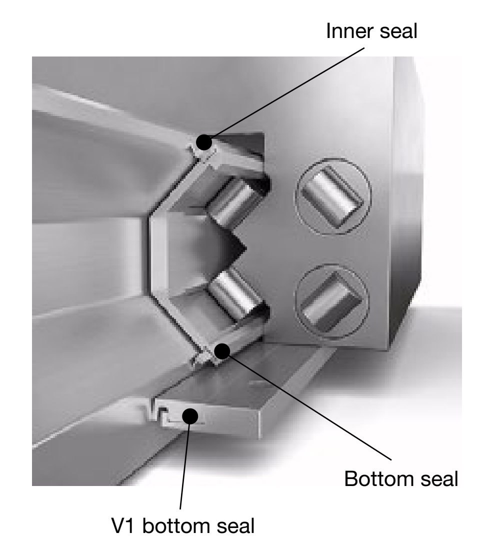

Fig. 7 V1 bottom seal

5.2. Designing the seal

Most of the highly dust-resistant seals used in roller guides initially exhibit high dust resistance, but with use over time, the sliding surface with the rails will become abraded and dust resistance will decrease. Therefore, the highly dust-resistant V1 seal and V1 bottom seal require materials with an excellent abrasion resistance of about 1/5 of the abrasion loss compared to a conventional rubber seal (Figure 8). Since linear guides come into contact with lubricant greases, rust-preventing oils used in packing, coolants used in machine tools, and other oils and greases, the resin components must be oil resistant. Particularly for seal components, dimensional changes with respect to oils and greases must be reduced. The materials adopted for the highly dust-resistant V1 seal and V1 bottom seal have been confirmed to exhibit small dimensional changes even under conditions immersed in oil and grease, providing an excellent feature as seal materials (Figure 9).

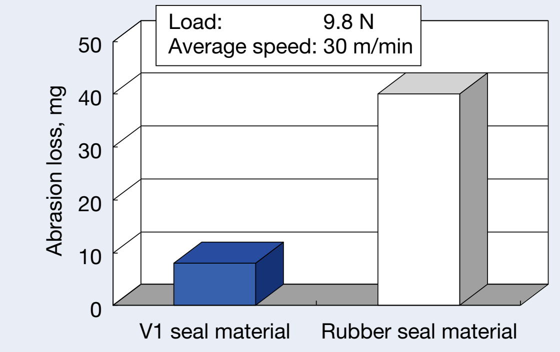

Fig. 8 Material abrasion test (ASTM D1044)

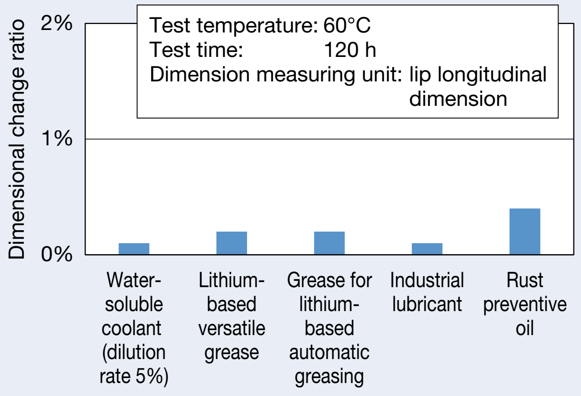

Fig. 9 Oil resistance of V1 seal material

To suppress abrasion in the sliding surface of the seal, it is essential to consider the contacting shape with the rails as well as the materials. This is also because reduction of the sliding resistance generated between the seal and the rail would suppress abrasion. To reduce the sliding resistance of the seal, it is generally sufficient to reduce interference between the seal and the rail and decrease the contact pressure. Reduction of the contact pressure, however, would make it easier for foreign matter such as processing powder to infiltrate, thereby diminishing dust resistance. In highly dust-resistant V1 seals and V1 bottom seals, in order to suppress the sliding resistance of the seal while maintaining a high dust resistance, the seal shape of the part that contacts the rail, called the lip, is slightly inclined toward the intruding direction of foreign matter to increase rigidity, and the shape provides elasticity in the perpendicular direction while also reducing contact pressure (Figure 10). The highly dust-resistant V1 seal and V1 bottom seal allow interference between the seal and the rail to be tripled, compared to a conventional rubber seal. As a result, high dust resistance is achieved for the intruding direction of foreign matter.

The highly dust-resistant V1 seal consists of a lip part that contacts the rail and a seal cover attached to the slider as a separate part (Figure 11). A seal cover shall be made of stainless steel and protect the inner resin components. In addition, the lip part is capable of changing to a component with different specifications depending on the application, with an expanded degree of freedom of the design. Further, for the V1 bottom seal, the outer surface is protected by a stainless steel cover and fastened to the slider body with screws. This structure ensures seal fixing force.

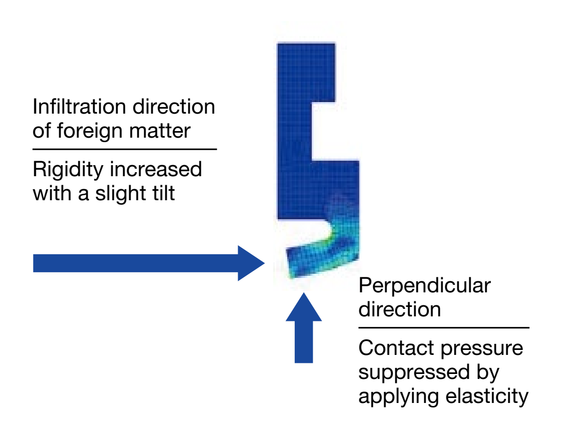

Fig. 10 Seal lip shape

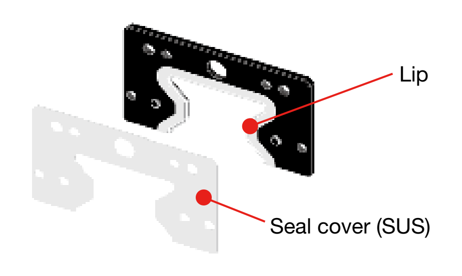

Fig. 11 Design of a highly dust-resistant V1 seal

5.3. Evaluation test of the seal

To evaluate the abrasion resistance of the highly dust-resistant V1 seal, a running test was performed with the seal sliding surface set to no lubrication state, and the sliding surface was observed (Photo 4). The test confirmed that the conventional rubber seal, which is the comparative object, showed a significant abrasion in the sliding surface and a slight tearing in the lip. However, the highly dust-resistant V1 seal only showed a slight abrasion and performed well in terms of abrasion resistance.

Sample:	RA35AN (medium preload)	Feed speed:	0.5 m/s
External load:	none	Stroke length:	200 mm
Lubricant:	none	Number of cycles:	10^5 cycles

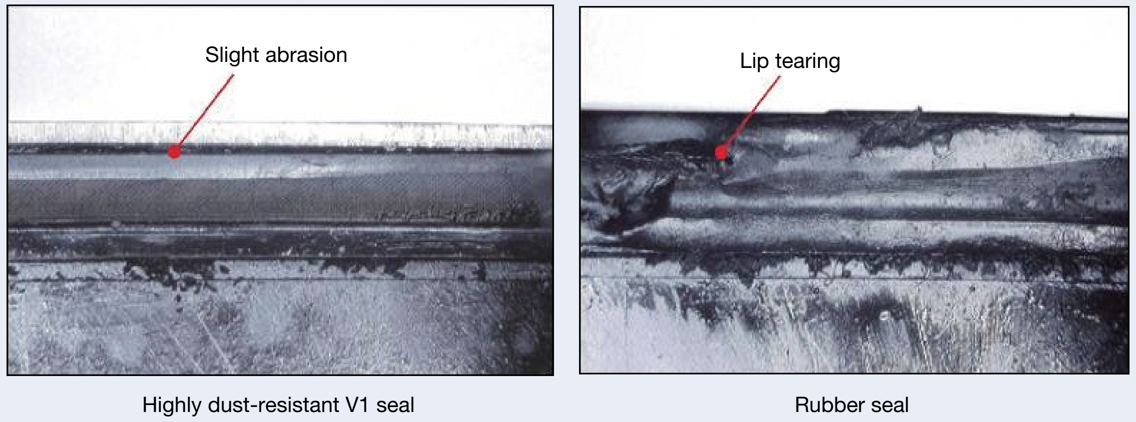

Highly dust-resistant V1 seal

Rubber seal

Photo. 4 Seal contact after non-lubricated running

Furthermore, to evaluate the durability of a roller guide assembled with the highly dust-resistant V1 seals, a running test (Figure 12) was conducted in an environment where casting powder as foreign matter was scattered around the sample, and the raceway surface shape was measured.

As a result, the sample assembled with the conventional rubber seals for the comparison was abraded by approximately 2.5 μm along the slider raceway surface, whereas the sample assembled with the highly dust-resistant V1 seals was abraded by approximately 1 μm (Figure 13). In addition, although an abrasion of the rail raceway surface of approximately 2.5 μm was observed in the sample assembled with the rubber seals, no abrasion was observed in the sample assembled with the highly dust-resistant V1 seals. The highly dust-resistant V1 seal was confirmed to be effective in improving the durability of the roller guides in an environment surrounded by foreign objects.

In order to evaluate whether infiltration of foreign matter was actually suppressed by the V1 bottom seal, a running test was performed under an environment in which coolant, iron powder, and casting powder were dispersed (Figure 14), and the status of foreign matter infiltration inside the slider was observed. In the test, roller guides were placed upside down, facilitating infiltration of the coolant, iron powder, and casting powder from the slider bottom.

As a result, it was confirmed that the sample without the V1 bottom seals, which is the comparative object, was infiltrated by iron powder and casting powder inside the slider, whereas in the sample assembled with the V1 bottom seals, almost no infiltration of foreign matter was observed. Moreover, the inside of the slider remained clean (Photo 5), confirming that the V1 bottom seal suppresses the infiltration of foreign matter.

The above evaluation confirmed that assembling roller guides with highly dust-resistant V1 seals and V1 bottom seals improved the reliability of products in an environment where processing powder and coolant are dispersed. Machine tools in machining centers, which are forced to frequently replace linear guides due to infiltration of foreign matter, would be expected to extend their replacement cycles.

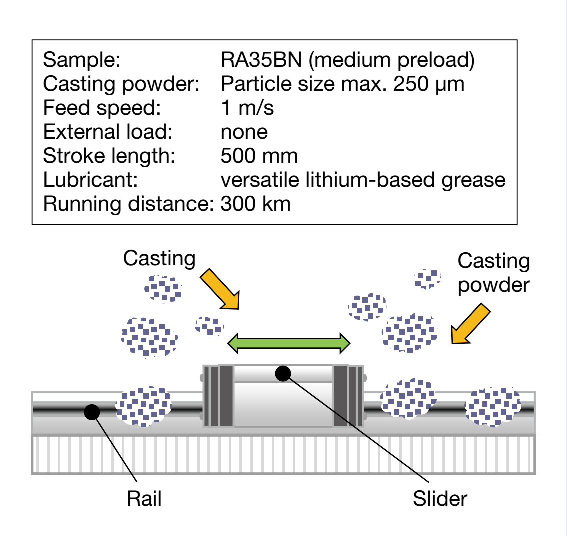
Sample: RA35BN (medium preload)
Casting powder: Particle size max. 250 μm
Feed speed: 1 m/s
External load: none
Stroke length: 500 mm
Lubricant: versatile lithium-based grease
Running distance: 300 km

Fig. 12 Test conditions

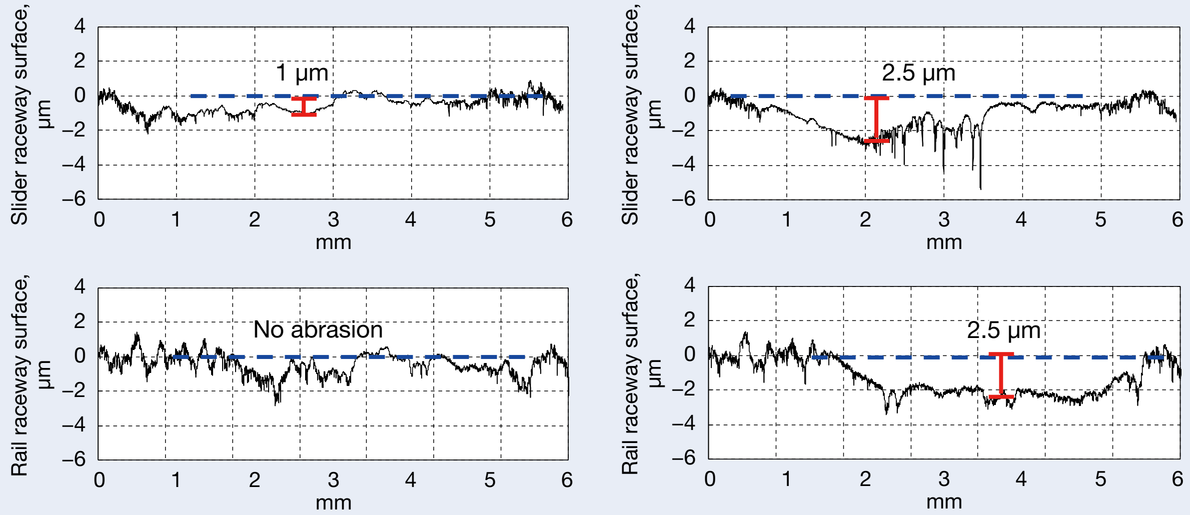

With highly dust-resistant V1 seal

With rubber seal

Fig. 13 Abrasion of raceway surfaces

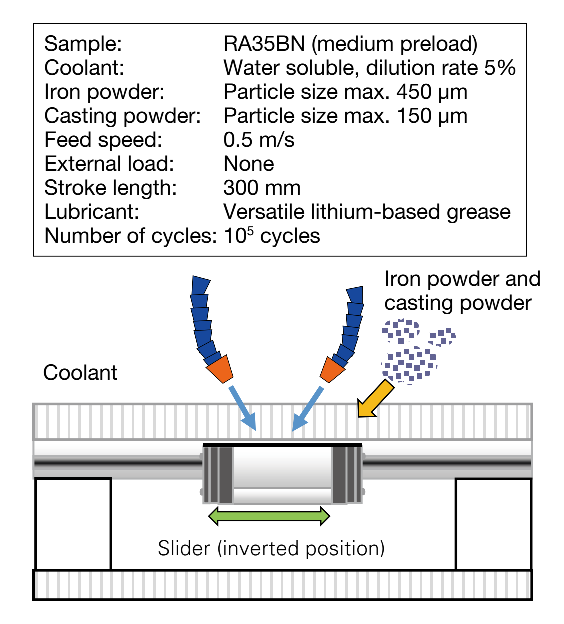
Sample: RA35BN (medium preload)
Coolant: Water soluble, dilution rate 5%
Iron powder: Particle size max. 450 μm
Casting powder: Particle size max. 150 μm
Feed speed: 0.5 m/s
External load: None
Stroke length: 300 mm
Lubricant: Versatile lithium-based grease
Number of cycles: 10^5 cycles

Fig. 14 Test conditions

With V1 bottom seal

Without V1 bottom seal

Photo. 5 Infiltration of foreign particles

6. Summary

This article introduces the advantages of the RA/RB Series, developed as roller guides for machine tools, as well as technology that improves reliability, used with the highly dust-resistant V1 seals and V1 bottom seals. At present, AI-based condition monitoring and life time estimation are also actively performed in machine tools. NSK is working on research and development of condition monitoring and life prediction technologies for rolling bearings as well as other elemental components. However, for linear guides that are relatively difficult to replace, NSK considers the reliability of the product itself in order to ensure its durability and stable motion accuracy throughout the product's life, as these aspects are of paramount importance. Looking ahead, NSK would like to contribute to the development of machine tools by promoting the research and development of condition monitoring and life time estimation technologies, and also by continuing to develop technologies for improving the reliability of the products themselves.

References

1) K. Nakano, "Improved reliability of Linear guides for Machine tools," *Machine Design 2019 Extra Edition*, 63-4 (2019), pp. 46–49.
2) "Precision Machine Components" No. E3162h AX-2 (2019), A259.
3) "NSK Linear Guide, Roller Guides with highly dustproof V1 seals and V1 bottom seals" No. E3334a X-8 (2018), pp. 1–4.
4) M. Aoki and H. Saito, "The Technical Trend of Machine Tool Components," *NSK Technical Journal Motion & Control* No. 30, C-6 (2019), pp. 28–38.

Kenta Nakano

Effect of Small Defect on the Flaking Strength of Rolling Bearings

(Part 1: FEM analyses of stress intensity factor K_{II} under rolling contact)

Sho Hashimoto, Hiroki Komata
Core Technology R&D Center, NSK Ltd.
Hisao Matsunaga
Kyushu Univ. Department of Mechanical Engineering
Kyushu Univ. Research Center for Hydrogen Industrial Use and Storage (HYDROGENIUS)
Kyushu Univ. International Institute for Carbon-Neutral Energy Research (I2CNER)

Abstract

It has been shown that a rolling contact fatigue (RCF) test using a specimen having a small drilled hole is a useful method for evaluating the effect of a small defect on the flaking strength of steel. In this study, RCF tests of rolling bearings having a small drilled hole were carried out. The flaking failure was considered as a problem of shear-mode fatigue crack emanating from the small defect. As a first step to quantify the crack-growth threshold on the basis of fracture mechanics, mode II stress intensity factor range, ΔK_{II}, of a ring-shaped crack emanated around the edge of a drilled hole under the passing of a rolling element was analyzed by using the finite element method. Then the obtained values were correlated with the ΔK_{II} values of penny-shaped cracks in an infinite body under uniform shear through the intermediary of a correlation factor, f_{drill}. The stress intensity factor of the ring-shaped crack was uniformly correlated with that of the penny-shaped crack by the single factor f_{drill} irrespective of hole diameter, d, depth of hole edge, h', and maximum contact pressure, q_{max}, within the ranges: d = 0.05 ~ 0.2 mm, h' = 0.05 ~ 0.345 mm and q_{max} = 2.0 ~ 3.0 GPa. The obtained results will be applied for the quantification of the RCF test results shown in the subsequent paper.

Translated and reprinted from the Journal of the *Japan Society of Mechanical Engineers*, Vol. 83, No. 852 (2017) (in Japanese), with permission from the Japan Society of Mechanical Engineers.

1. Introduction

Flaking of a rolling bearing is a type of fatigue-fracture phenomena caused by repeated contact stress.

Flaking is known to have various mechanisms, one of which is a form caused by crack initiation and growth from non-metallic inclusions in the rolling bearing (Mitamura, 2008). Ensuring a high level of cleanliness is effective in order to suppress this sort of fracture and to extend the life of rolling bearings. On the other hand, the fatigue crack growth behavior generated from a small defect and the effect of the defect dimension on flaking strength have not been investigated quantitatively. The reasons behind the delay in quantitative understanding of the phenomenon include: (i) the minuteness of the defect at the starting point, (ii) the difficulty in direct observation of the fracture process because the fracture origin exists inside the material, and (iii) many unknown points in the growth feature of the shear-mode fatigue crack that governs the majority of flaking life.

There is no standard test method for shear-mode fatigue crack growth in steel with high-hardness material. Research is being carried out using various experimental methods; for example, a test method using a DC (Double Cantilever) type specimen by Murakami et al. (Murakami et al., 1994, 2002, Murakami et al., 2003, 2008), a test method using CT specimens by Otsuka et al. (Otsuka et al., 1994), and a method of repeatedly applying torsion while applying a static compressive load to round bar specimens by Matsunaga et al. (Matsunaga et al., 2009, Matsunaga et al., 2011, Okazaki et al., 2014, 2017, Endo et al., 2015). Moreover, attempts have been made to elucidate the growth and non-propagation behavior of shear-mode fatigue cracks by introducing small defects in the raceway of rolling contact fatigue (RCF) specimens and by limiting the locations where cracks occur in order to facilitate observation (Kida et al., 2004, 2006, Fujimatsu et al., 2015). The authors have also conducted RCF tests using a JIS-SUJ2 flat plate specimen with small drilled holes in the raceway to investigate the growth behavior of shear-mode fatigue cracks and have studied methods for evaluating flaking strength as a crack problem (Komata et al., 2012, 2013).

In this research, we aim to establish a fracture mechanics evaluation method of RCF strength by further developing the above-mentioned research and to perform a RCF test by introducing a drilled hole to the raceway of the inner ring of a deep groove ball bearing. This will elucidate the effect of the diameter and depth of the small defects on the flaking strength at the actual machine level. There is much that is unknown about the mechanical states and the growth behavior of cracks, which are generated and developed from non-metallic inclusions and artificial defects under rolling contacts. In order to quantify the RCF test results of rolling bearings having small drilled holes as a crack problem, the stress intensity factors of ring-shaped cracks generated from the edges of drilled holes with various diameters and dimensions under rolling contact are analyzed by FEM. It is then shown that the stress intensity factor of a crack generated from a drilled hole is nearly in a one-to-one relationship with the stress intensity factor of a penny-shaped crack subjected to shear in an infinite body through one correlation factor, which is within the scope of the load condition of a RCF test conducted in the following report and the drilled hole diameter/depth used in the experiments.

2. Mode II Stress Intensity Factor of Penny-Shaped Cracks under Rolling Contact

In this chapter, the stress intensity factors of a penny-shaped crack existing immediately below the rolling contact portion of the rolling element (steel ball) and raceway (inner ring) are obtained by FEM analysis.

2.1 Target for analysis

Figure 1 shows a rolling bearing (JIS-SUJ2 deep groove ball bearing) used in RCF tests. In this rolling bearing, rolling elements (diameter: 9.525 mm, JIS-SUJ2 steel balls) arranged at equal intervals between the inner ring and the outer ring roll on the inner ring raceway surface and the outer ring raceway surface while applying a load.

2.2 Shear stress distributions in the inner ring raceway for defect-free cases

Using versatile finite element analysis software MSC. Marc 2013r1, the stress field generated when the inner ring raceway makes Hertzian contact with a steel ball is obtained by elastic analysis. Figure 2 shows the analysis model. The analysis model is a 1/2 model with the *xz* plane as the symmetry plane. An external force in the z-axis direction was applied to the steel ball to bring it into contact with the raceway surface. The displacement constraint in the *y* direction is given to the nodal points existing in the *xz* plane by taking the symmetry into account. The inner ring had a Young's modulus of 208 GPa and a Poisson's ratio of 0.3. A 4-node tetrahedral element (TETRA 4) was used for the inner ring to be analyzed, and the minimum element size of the contact surface was 0.010 mm. The steel ball is assumed to be rigid in consideration of the computational costs. Furthermore, in order to simplify the analysis, these assumptions are made: the inner raceway surface is a plane, the equivalent radius of the curvature calculated from the raceway surface and the radius of the curvature of the steel ball is applied to the steel ball side, and the shape of the steel ball is barrel-shaped. The elliptical contact generated by the rolling bearing used in the experiment was reproduced. At this time, the dimensions of the steel ball were adjusted so that the contact ellipse dimension and the contact surface pressure were equal to those of the case where the steel ball was an elastic body. Table 1 shows the sizes of the steel ball (represented by the suffix e in Table 1) and the inner raceway surface (represented by the suffix w in Table 1). Table 2 shows the results of calculating the contact elliptical dimensions (minor radius s_b, major radius s_a) and the maximum contact surface pressure q_{max} when they are brought into contact by FEM analysis and Hertzian contact theory. As shown in Table 2, it can be seen that by using the sizes shown in Table 1, a result equivalent to the contact state between the elastic bodies can be obtained using a simpler FEM model. In this analysis, the friction due to the contact between the steel ball and the inner raceway surface is not considered.

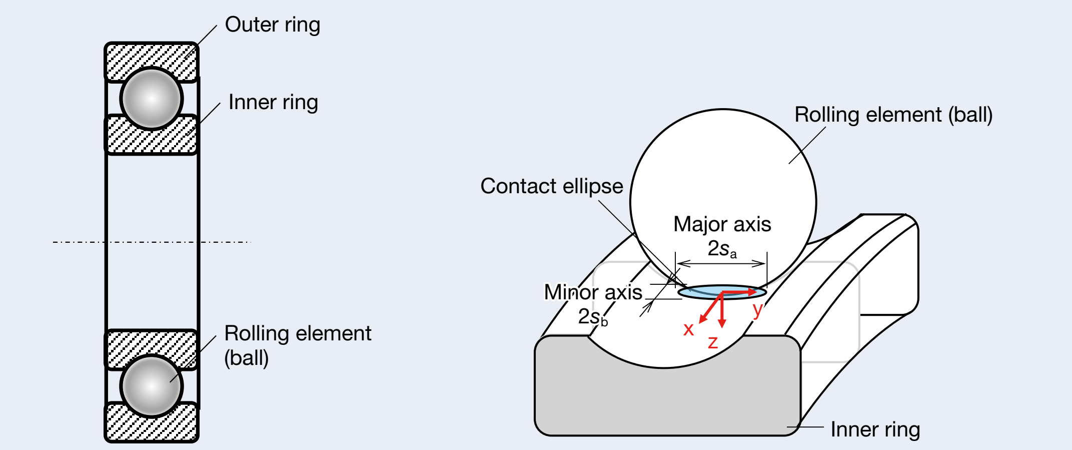

(a) Radial type rolling bearing

(b) Ellipse type contact area on rolling bearing

Fig. 1 Target of FEM analysis. Contact ellipse is generated between ball and ring.

Table 1 Sizes and material properties of contact bodies for evaluation.

	Actual size	Equivalent size	Used value in FEM analysis
Curvature radius 1 of rolling element, R_{e1} [mm]	9.525/2	3.787	7.574
Curvature radius 2 of rolling element, R_{e2} [mm]	9.525/2	399.2	800
Curvature radius 1 of raceway, R_{w1} [mm]	18.49	∞ : Flat	∞ : Flat
Curvature radius 2 of raceway, R_{w2} [mm]	−4.82	∞ : Flat	∞ : Flat
Young's modulus of rolling element, E_e [GPa]	208	208	∞ : Rigid
Young's modulus of raceway, E_w [GPa]	208	208	208
Poisson's ratio of rolling element, ν_e	0.3	0.3	− : Rigid
Poisson's ratio of raceway, ν_w	0.3	0.3	0.3

Table 2 Size of calculated contact area and maximum contact pressure.

	Rolling bearing (Hertz theory) Elastic ball / Elastic raceway	Flat plate (FEM analysis) Rigid element / Elastic plate
Applied load on rolling element, F [N]	4645.8	4645.8
Semi-major axis of contact area, s_a [mm]	3.722	3.625
Semi-minor axis of contact area, s_b [mm]	0.198	0.195
Maximum contact pressure, q_{max} [GPa]	3.00	3.03

Figure 3 shows an analysis result of the shear stress distribution τ_{xz} inside the inner ring when q_{max} = 3.0 GPa. At this time, the depth z_0 at which τ_{xz} becomes the maximum is z_0 = 0.099 mm in the exact solution of Lundberg (Lundberg and Palmgren, 1947), whereas z_0 = 0.100 mm in the present analysis, and both are almost the same. Figure 4 (a) shows the distribution of the shear stress τ_{xz} in the x direction at the depths z = 0.100 mm and z = 0.200 mm. Figure 4 (b) shows the distribution of the shear stress τ_{xz} in the z direction at x = 0.172 mm at which the shear stress τ_{xz} is maximized. When the steel ball moves on the inner ring raceway surface while applying the load, an alternating shear stress is generated inside the raceway surface. In Figs. 4 (a) and 4 (b), the exact solution of the shear stress distribution obtained by the Lundberg equation is also shown by a solid line. The values of shear stress obtained by the present analysis almost agreed with the exact solution. That is, it was shown that the Hertzian contact between the steel ball and the inner ring raceway can be accurately reproduced by this analysis method.

2.3 Mode II stress intensity factor of a penny-shaped crack under uniform shear

In order to investigate the analysis method of the mode II stress intensity factor K_{II} by FEM, a penny-shaped

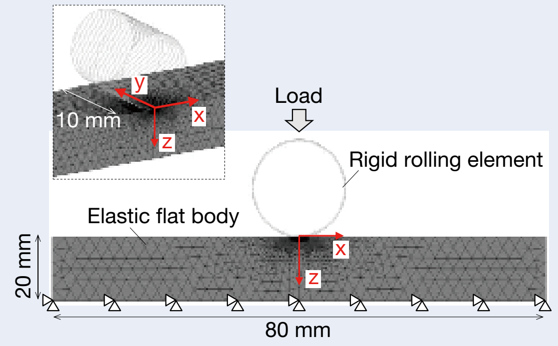

Fig. 2 FEM model of contact between rigid rolling element and elastic flat body. The ball is rigid barrel-shaped body and the raceway is elastic flat body.

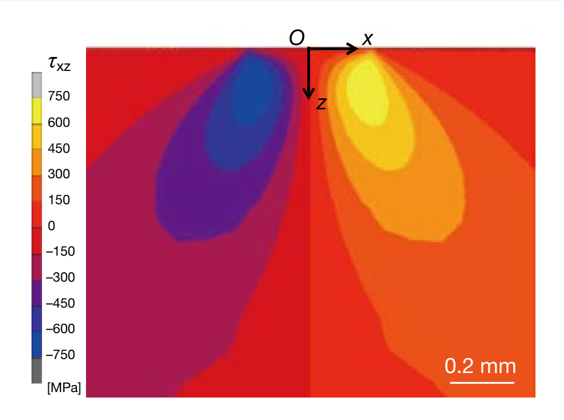

Fig. 3 Example of contour map of shear stress τ_{xz} in smooth specimen (q_{max} = 3.0 GPa).

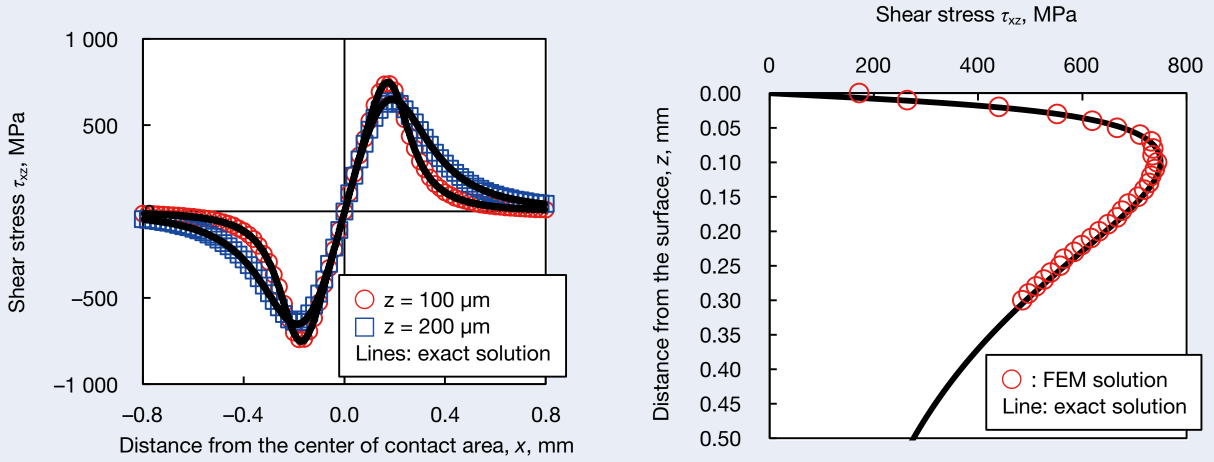

(a) τ_{xz} at z = 0.1 mm and z = 0.2 mm

(b) τ_{xz} at x = 0.172 mm

Fig. 4 Distribution of shear stress τ_{xz} in x direction (a) and z direction (b) in smooth specimen. The shear stress distribution obtained by FEM corresponded to the exact solution by Lundberg and Palmgren.

crack with a radius a as shown in Figure 5 was introduced inside the inner ring of the analysis model in Figure 2. Figure 6 shows, as an example, an analysis model in which a penny-shaped crack having a radius a = 0.010 mm is arranged at a depth of z = 0.100 mm. By applying an external force in the x-axis direction to the rigid body surface firmly in contact with the inner ring raceway surface, uniform shear stress τ_{xz0} was applied to the crack at the center of the analysis target. The friction coefficient of the crack surface was set to 0. Other boundary conditions are similar to the model in Figure 2. In a penny-shaped crack subjected to shearing, as shown in Figure 5, the deformation mode along the crack leading edge changes from mode II to mixed mode (mode II + mode III) to mode III, resulting in a pure mode II at point A in Figure 5. In this analysis, the K_{II} at point A was obtained for crack radii a = 0.005 mm, 0.010 mm, 0.020 mm, 0.050 mm, 0.100 mm, 0.200 mm, and 0.400 mm. In the vicinity of the crack tip which becomes the singularity of stress, the element was subdivided, and the distance between nodal points was made to be 0.0004 mm.

Figure 7 shows a contour map of τ_{xz} around the crack when τ_{xz0} = 750 MPa is applied to the model with a crack radius of a = 0.010 mm in Figure 6 as an example of analytical results. As shown in Figure 8, the distribution of τ_{xz} was obtained from the crack tip in the direction parallel to the x-axis, and the tentative stress intensity factor K_{II}^* obtained from each node was calculated using equation (1).

$$K_{\mathrm{II}}^* = \tau_{xz} \cdot \sqrt{2\pi r} \qquad \cdots\cdots\cdots\cdots (1)$$

Here, r is the distance between each node and the crack tip. Figure 9 shows an example of K_{II} obtained by the stress extrapolation method (Ishida, 1976). The stress extrapolation method plots K_{II}^* obtained from each node against the distance r from the crack tip and obtains K_{II}^*(= K_{II}) at r = 0 by extrapolation of an approximate straight line. As can be seen from Figure 9, the K_{II}^* values obtained from the nodal points near the crack tip deviate from the true values due to the insufficient fineness of the element for the singular stress field and therefore were excluded from the target data of the approximate straight line. Table 3 shows the calculated results of K_{II} when the crack radius a is varied from 0.005 mm to 0.400 mm.

On the other hand, the stress intensity factor for a penny-shaped crack with radius a, present in an infinite body subjected to shear stress τ (hereinafter referred to as K_{II0}), is obtained from the analytical solution of Kassir et al. (Kassir and Sih, 1966). K_{II0} at point A on the x-axis of a penny-shaped crack as shown in Figure 5 is given by the following equation:

$$K_{\mathrm{II0}} = \frac{4}{(2-\nu)\pi}\,\tau\sqrt{\pi a} \qquad \cdots\cdots\cdots\cdots (2)$$

Where ν is Poisson's ratio. Table 3 shows the values of K_{II} obtained from FEM analysis and equation (2). Since both methods are nearly identical, it can be said that this FEM analysis method has sufficient accuracy for the analysis of K_{II}.

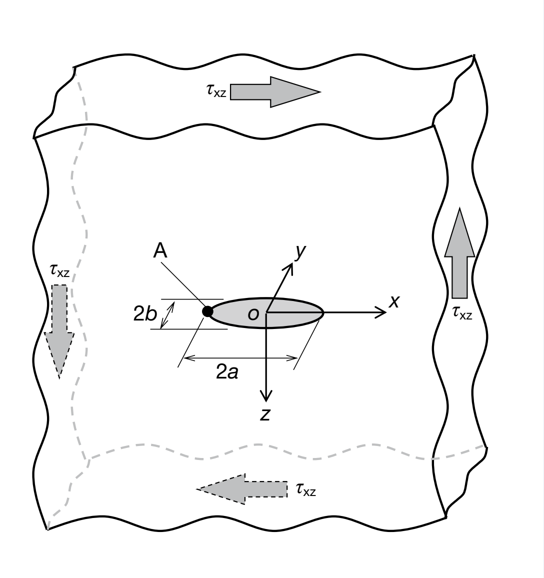

Fig. 5 Penny-shaped crack in an infinite elastic body. The crack is deformed by pure mode II at point A.

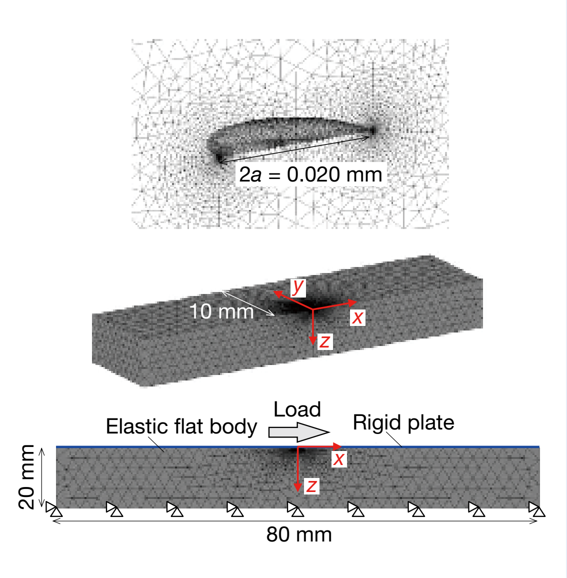

Fig. 6 FEM model of elastic body under shear including a penny-shaped crack.

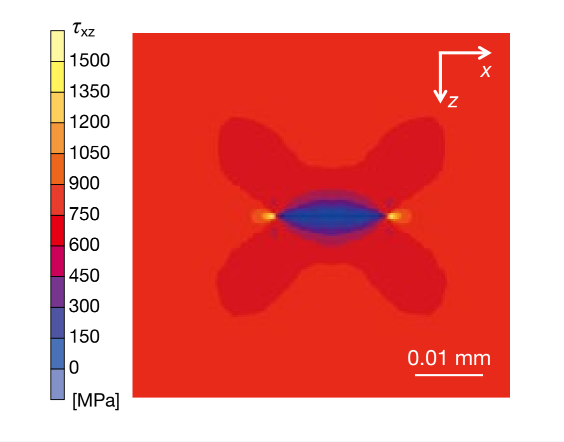

Fig. 7 Example of contour map of shear stress τ_{xz} around penny-shaped crack.

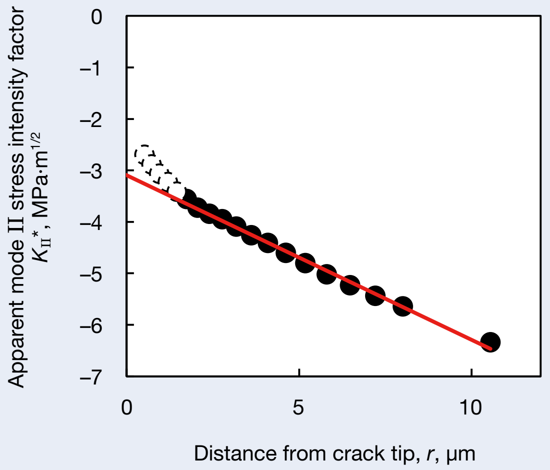

Fig. 9 Stress extrapolation method for calculating stress intensity factor K_{II}. The data at points close to the crack tip were used for the extrapolation as shown by red line.

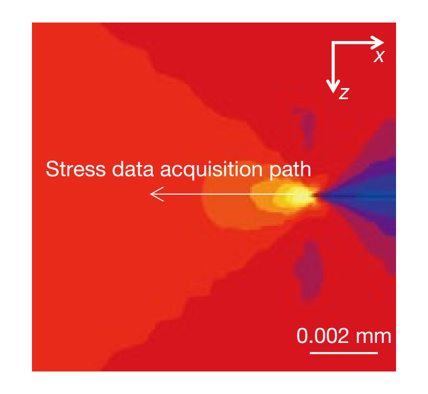

Fig. 8 Path of stress data acquisition near crack tip for which K_{II} was calculated.

Table 3 Comparison in stress intensity factors between FEM solution and exact solution.

Radius of crack a [mm]	Mode II stress intensity factor K_{II} [MPa·m$^{1/2}$]		FEM solution / Exact solution [%]
	FEM solution	Exact solution by Kassir & Sih	
0.005	2.19	2.23	98.3
0.010	3.09	3.15	98.2
0.020	4.44	4.45	99.8
0.050	6.86	7.04	97.4
0.100	9.82	9.96	98.7
0.200	13.91	14.08	98.8
0.400	19.83	19.91	99.6

2.4 Mode II stress intensity factor of a penny-shaped crack under rolling contact

In the rolling contact model shown in Figure 2, a penny-shaped crack with a radius of a was arranged as shown in Figure 6. The K_{II} of the penny-shaped crack existing in the rolling contact stress field was obtained by moving the steel ball in compressive contact. Figure 10 shows an analytical model for a penny-shaped crack with a radius of a = 0.010 mm, as an example, placed at a depth z = 0.100 mm from the raceway surface. In order to investigate the change in K_{II} at point B in Figure 11 due to the movement of the steel ball, the steel ball was positioned sufficiently away from the penny-shaped crack (x = −0.6 mm, with the crack center at x = 0), and moved to x = +0.6 mm while maintaining the contact state. In this analysis, penny-shaped cracks with a crack radius of 0.005 mm, 0.010 mm, 0.020 mm, 0.050 mm, 0.100 mm, 0.200 mm, and 0.400 mm were arranged at the position of depth z = 0.100 mm, similar to the analysis by the model of Figure 6. The load applied to the steel ball was adjusted so that the maximum contact surface pressure $q_{\max}$ was 3.0 GPa. When a load is applied to the rolling bearing model of this analysis so that the maximum contact surface pressure $q_{\max}$ becomes 3.0 GPa, τ_{xz} takes the maximum value at the position of the depth z = 0.100 mm. The depth of the penny-shaped crack was matched with the depth at which the maximum value of τ_{xz} occurred, and z = 0.100 mm. In this FEM analysis, K_{II} was obtained every time the steel ball moved by 0.020 mm.

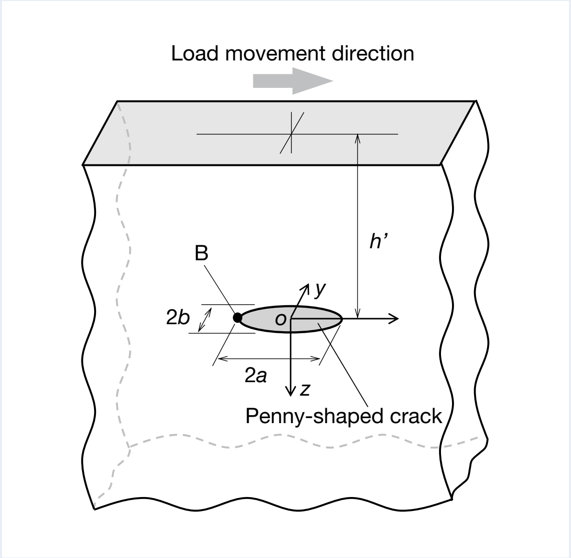

Fig. 11 Penny-shaped crack under rolling contact. The change in the value of K_{II} at point B was evaluated.

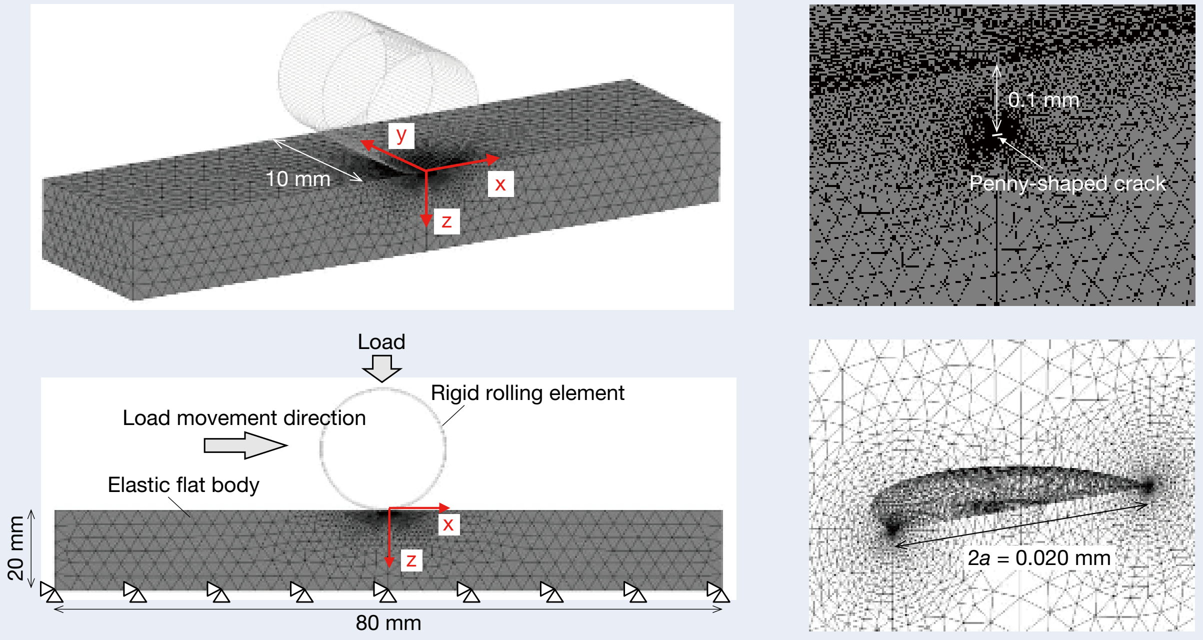

(a) FEM contact model

(b) Half model of penny-shaped crack

Fig. 10 FEM model of contact between rigid rolling element and elastic flat body having a penny-shaped crack.

Figure 12 shows the change in K_{II} when the steel ball moves on the raceway surface for the penny-shaped cracks having a radius a of 0.010 mm, 0.050 mm, and 0.100 mm. In each case, K_{II} changed from a negative peak to a positive peak with the movement of the steel ball. The difference between the positive and negative peaks at this time was calculated for each crack radius a, as the mode II stress intensity factor range ΔK_{II}. Figure 13 compares the FEM analysis results with the analytical solution of Kassir et al. given by the following equation for the relation between crack radii a and ΔK_{II}.

$$\Delta K_{\mathrm{II0}} = \frac{4}{(2-\nu)\pi}\,\Delta\tau\sqrt{\pi a} \qquad \cdots\cdots\cdots\cdots (3)$$

Here, $\Delta\tau$ is the shear stress range acting on an infinite body at a distance. In a rolling contact stress field, alternating shear stress acts, so when τ_{xz} at the depth of a penny-shaped crack is used as the nominal shear stress, $\Delta\tau$ is expressed by the following equation.

$$\Delta\tau = 2\tau_{xz} \qquad \cdots\cdots\cdots\cdots (4)$$

According to Lundberg's exact solution, under this analysis condition, τ_{xz} = 750 MPa at a depth z = 0.100 mm, so this value was used as the nominal shear stress. Figure 13 shows that ΔK_{II} of a penny-shaped crack in a rolling contact stress field coincides with ΔK_{II0} when the crack radius a is in the range of 0 to 0.1 mm. On the other hand, when a > 0.1 mm, the two diverged, and the ΔK_{II} of the crack under rolling contact was lower than ΔK_{II0}. In other words, even in the case where the steel ball and the inner ring raceway are in rolling contact, for a penny-shaped crack up to a radius of about 0.1 mm, τ_{xz} acting on the depth at which the crack exists is defined as the nominal shear stress, ΔK_{II} can be obtained with high accuracy by the equation (3).

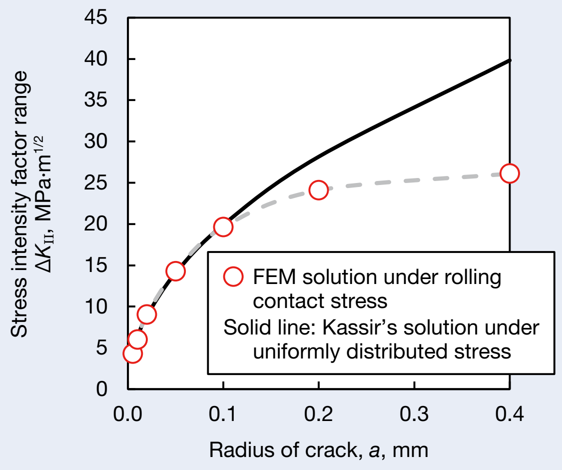

Fig. 13 Change in stress intensity factor range as a function of crack radius. ΔK_{II} corresponds to ΔK_{II0} within the range: a = 0 ~ 0.1 mm.

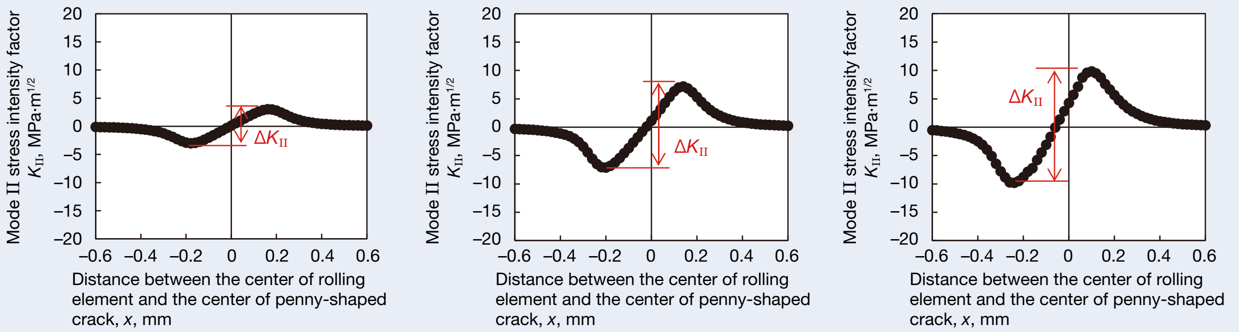

(a) a = 0.010 mm

(b) a = 0.050 mm

(c) a = 0.100 mm

Fig. 12 Change in stress intensity factor K_{II} at point B in Fig. 11 caused by the movement of ball under compressive contact. In all the cases, K_{II} varied from the negative peak to the positive peak.

3. Mode II Stress Intensity Factor at the Edge of a Small Drilled Hole under the Rolling Contact

In the previous chapter, it was shown that the mode II stress intensity factor range ΔK_{II} of a penny-shaped crack existing in a rolling contact stress field can be obtained with high accuracy by FEM analysis. In the rolling bearings analyzed in this study, it was found that ΔK_{II} can be evaluated as equivalent to a crack existing in a uniform shear stress field when the crack radius is as small as $a \leq 0.1$ mm. Subsequently, this chapter is directed to a case where a drilled hole, as shown in Figure 14, exists in the raceway of the inner ring. A ring-shaped crack generated from the edge of the drilled hole is analyzed using the same model as the penny-shaped crack shown in Figure 10.

Figure 15 shows a photograph of the cross-section of a drilled hole after a RCF test was conducted with stress cycles of $N = 2.6 \times 10^8$ cycles, under the condition that the maximum contact surface pressure $q_{\max} = 2.5$ GPa, using a deep groove ball bearing with a drilled hole having a diameter $d = 0.100$ mm and an edge depth $h' = 0.064$ mm applied to the inner ring. The details of the experimental method and results will be described in the next report. As shown in Figure 15, small cracks were observed at the edge of the drilled hole, which were considered to be in a non-propagation state. Such non-propagation cracks were also observed in other specimens having different diameters and depths of the drilled holes, and their sizes were approximately 0.01 mm. Similar cracks have been observed in un-flaked specimens in the RCF tests of bearing steel conducted by the authors in the past (Komata et al., 2013). In order to quantify the flaking limit of such a specimen as the non-propagating limit of fatigue crack, the above-mentioned ring-shaped small crack (crack length $a = 0.010$ mm) was introduced into the drilled hole edge and analyzed. Figure 16 shows, as an example, an analysis model including an inner ring having a drilled hole with a diameter $d = 0.100$ mm and an edge depth $h' = 0.100$ mm as well as a steel ball in compression contact with the inner ring.

In this analysis, the drilled hole diameter d was set to 0.050 mm, 0.075 mm, 0.100 mm, and 0.200 mm, and the edge depth h' was changed to 0.050 mm, 0.100 mm, 0.220 mm, and 0.345 mm for each diameter. In order to investigate the variation of K_{II} at point C in Figure 17 with the movement of the steel ball, as in the case of a penny-shaped crack shown in Figure 11, the steel ball was compressed and contacted at a position sufficiently far from the drilled hole (the position of $x = -0.6$ mm with the drilled hole center position as $x = 0$) and moved to $x = +0.6$ mm while maintaining the contact state. For the steel ball, a load equivalent to $q_{\max} = 3.0$ GPa, 2.5 GPa, and 2.0 GPa was applied. Table 4 summarizes the maximum contact surface pressure $q_{\max}$, the minor radius s_b of the contact ellipse, the maximum value of the shear stress τ_{xz}, the depth τ_{xz} works z_0, and the shear stress τ_{xz} acting on the drilled hole edge depth $z = h'$. Also, in this analysis, every time the steel ball moved 0.020 mm, the K_{II} of the crack at the edge of the drilled hole was obtained by the same method as for the penny-shaped crack.

Figure 18 shows a change in K_{II} at point C of the analysis model (drilled hole diameter $d = 0.100$ mm, edge depth $h' = 0.100$ mm) shown in Figure 16 as an example of the analysis result. In the crack at the edge of the drilled hole, K_{II} changed from a negative peak to a positive peak with the movement of the steel ball, as in the case of the penny-shaped crack. However, the ratio of the positive and negative peaks of the stress intensity factor, $K_{\mathrm{IImin}}/K_{\mathrm{IImax}}$, was −1 for the penny-shaped crack, while it was about −2.7 for the crack at the edge of a drilled hole. It is considered that this difference was caused by the absence of an elastic body which receives the stress in the drilled hole. The difference of the positive and negative peaks of K_{II}, ΔK_{II}, is calculated for various combinations of drilled hole diameters d depths h', and contact surface pressure conditions $q_{\max}$. Figure 19 shows their results as a relationship between the crack radius including the drilled hole $(d/2 + a')$ and ΔK_{II}. In Figure 19, the values of ΔK_{II} obtained by setting the crack radii to $a = (d/2 + a')$ and using the nominal shear stress ranges $\Delta\tau$ acting on the edge depth h', in equation (3), are also shown by solid lines. As shown in chapter 2, the ΔK_{II} of a penny-shaped crack in a rolling contact stress field almost coincides with the ΔK_{II0} obtained from the analytical solution of a crack in a uniform stress field when the crack radius a is smaller than 0.1 mm. On the other hand, the ΔK_{II} of the crack generated from the edge of the drilled hole was smaller than that of a penny-shaped crack even in the case of $(d/2 + a') \leq 0.1$ mm. This difference is also presumed to be due to the absence of an elastic body that receives stress in the drilled hole. In addition, the larger the drilled hole diameter, the greater the deviation between the two. These trends were similar, regardless of the maximum contact pressure, when $q_{\max}$ was within the range of 2.0 GPa to 3.0 GPa. Similar trends were also confirmed at various edge depths ($h' = 0.05$ mm, 0.100 mm, 0.220 mm, 0.345 mm).

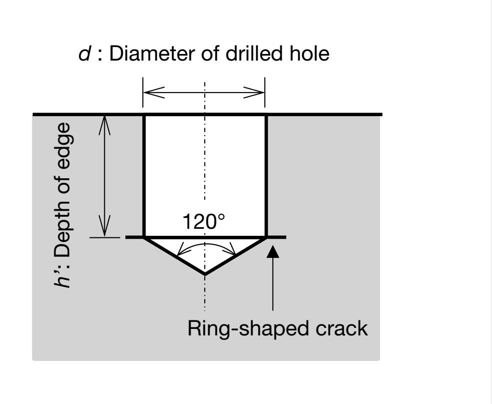

Fig. 14 Geometry of drilled hole. The drilled hole has a ring-shaped crack at the edge.

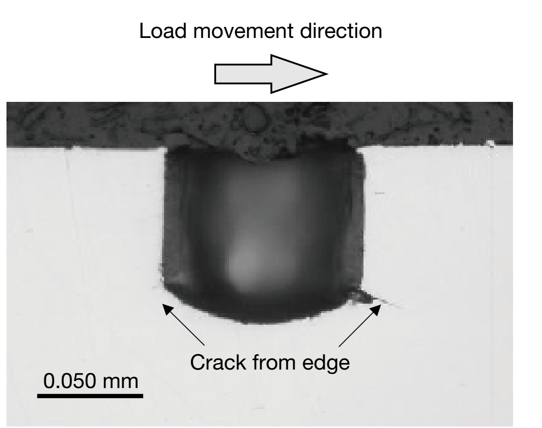

Fig. 15 Cross section of drilled hole after fatigue test. ($q_{\max} = 2.5$ GPa, $N = 2.6 \times 10^8$ cycle) Small cracks were observed at the hole edge.

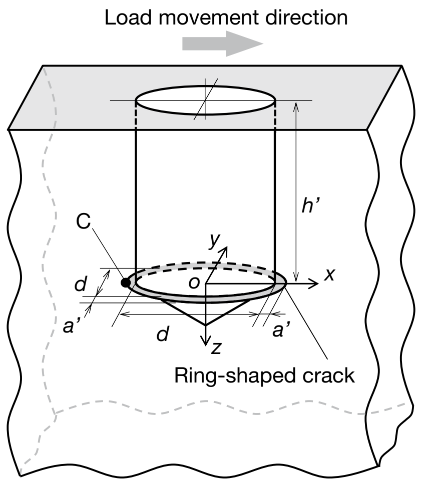

Fig. 17 Ring-shaped crack emanated from hole edge under rolling contact. The change in K_{II} at point C was evaluated.

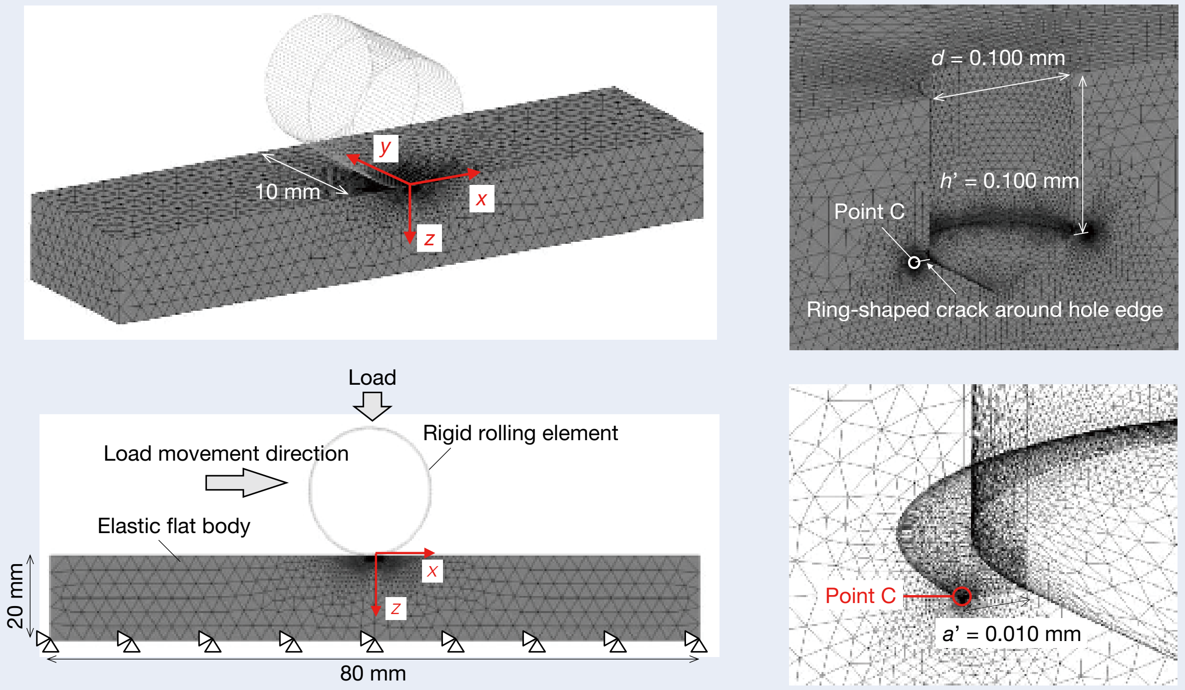

(a) FEM contact model

(b) Ring-shaped crack around hole edge

Fig. 16 FEM model of the contact between ball and flat plate having a small drilled hole. All the model has a ring-shaped crack at the edge of the drilled hole.

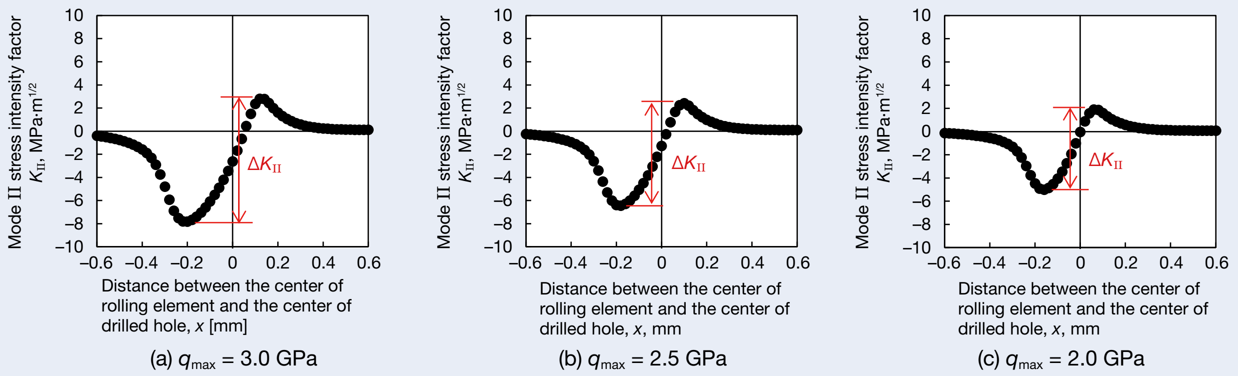

(a) q_{max} = 3.0 GPa (b) q_{max} = 2.5 GPa (c) q_{max} = 2.0 GPa

Fig. 18 Change in stress intensity factor K_{II} at point C in Fig.17 caused by the movement of ball under compressive contact : d = 0.100 mm, h' = 0.100 mm. In common with the cases of penny-shaped crack, K_{II} varied from the negative peak to the positive peak.

Table 4 Results of FEM analysis for different maximum contact pressures and hole depths

	Load case 1	Load case 2	Load case 3
Maximum contact pressure, q_{max} [GPa]	3.00	2.50	2.00
Applied load force to rolling element, F [N]	4645.8	2684.5	1375.4
Semi-major axis of contact area, s_a [mm]	3.722	3.100	2.480
Semi-minor axis of contact area, s_b [mm]	0.198	0.165	0.132
Maximum value of shear stress, τ_{xz} [MPa]	750	625	500
Depth that maximum shear stress works, z_0 [mm]	0.099	0.083	0.066
Shear stress τ_{xz} at z = 0.050 mm [MPa]	681	591	491
Shear stress τ_{xz} at z = 0.100 mm [MPa]	750	619	477
Shear stress τ_{xz} at z = 0.220 mm [MPa]	624	471	326
Shear stress τ_{xz} at z = 0.345 mm [MPa]	474	343	227

4. Derivation of Approximation Formula for Mode II Stress Intensity Factor Range of Small Drilled Hole Edges under Rolling Contact

In this chapter, mode II stress intensity factors are compared between a penny-shaped crack in an infinite body subjected to shear and a crack at the edge of a drilled hole. From the examination results in chapters 2 to 3, it was found that ΔK_{II} of a ring-shaped crack existing around the edge of a drilled hole in a rolling contact stress field (hereinafter referred to as $\Delta K_{II,drill}$) shows a certain tendency with respect to ΔK_{II0} calculated from the analytical solution of Kassir et al. (equation (3)) by assuming τ_{xz} generated at the edge depth h' as the nominal shear stress. Here, the relation between $\Delta K_{II,drill}$ and ΔK_{II0} is expressed as equation (5) using the correlation factor f_{drill}.

$$\Delta K_{II,drill} = f_{drill} \cdot \Delta K_{II0} = f_{drill} \cdot \frac{4}{(2-\nu)\pi} \Delta\tau \sqrt{\left(\frac{d}{2} + a'\right)} \quad \cdots\cdots (5)$$

Where $\Delta\tau$ is obtained by equation (4) using the nominal shear stress τ_{xz} acting on the drilled hole edge depth h'. When considering the effect of the defect size on f_{drill}, the effect of the drilled hole diameter d and the drilled hole edge depth h' must be taken into account for drilled holes, but the effect of the drilled hole depth h' is considered in the calculations of ΔK_{II} as shear stress τ_{xz}. Therefore, we evaluate the effect on the drilled hole diameter d here. Figure 20 shows the ratios of $\Delta K_{II,drill}$ to ΔK_{II0} (i.e., f_{drill}) based on the series of analysis results shown in Figure 19 for each q_{max}, each h', plotted against the drilled hole diameter d. $\Delta K_{II,drill}$ /ΔK_{II0} decreased linearly with increasing drilled hole diameter. This tendency was almost

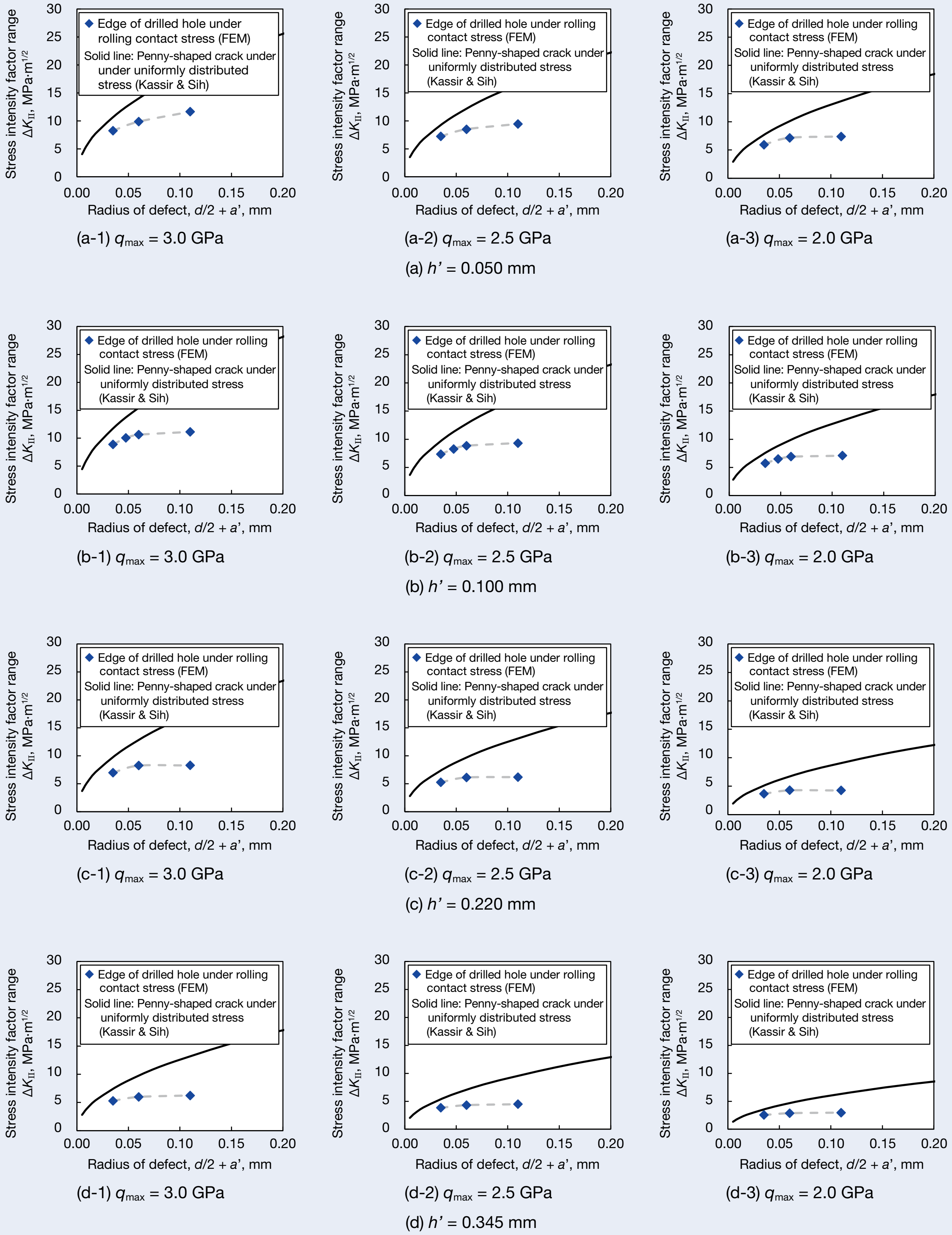

(a-1) q_{max} = 3.0 GPa (a-2) q_{max} = 2.5 GPa (a-3) q_{max} = 2.0 GPa

(a) h' = 0.050 mm

(b-1) q_{max} = 3.0 GPa (b-2) q_{max} = 2.5 GPa (b-3) q_{max} = 2.0 GPa

(b) h' = 0.100 mm

(c-1) q_{max} = 3.0 GPa (c-2) q_{max} = 2.5 GPa (c-3) q_{max} = 2.0 GPa

(c) h' = 0.220 mm

(d-1) q_{max} = 3.0 GPa (d-2) q_{max} = 2.5 GPa (d-3) q_{max} = 2.0 GPa

(d) h' = 0.345 mm

Fig. 19 Stress intensity factor range as a function of defect size at four different edge depths. ΔK_{II} values of the hole-edge cracks were smaller than those of the penny-shaped cracks.

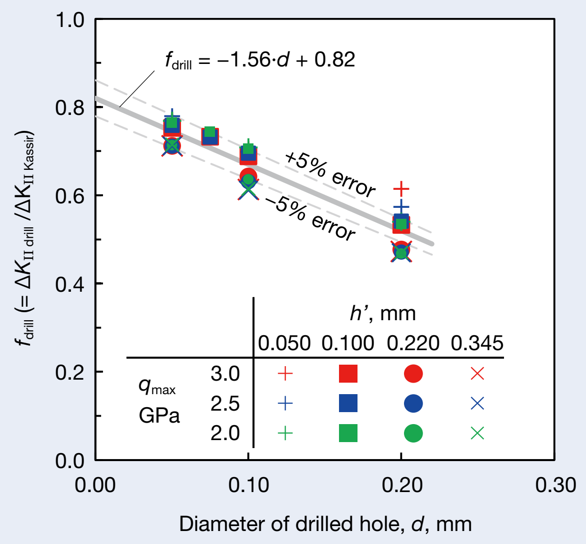

Fig. 20 f_{drill} as a function of d for various q_{max} and h'. The value of f_{drill} decreased linearly with an increase in the hole diameter. The slope was approximately constant irrespective of q_{max} and h'.

constant regardless of the maximum contact surface pressure q_{max} and the edge depth h'. Therefore, f_{drill} is expressed by the following equation as a function of the drilled hole diameter d.

$$f_{drill} = A \cdot d + B \quad \cdots\cdots\cdots\cdots (6)$$

Here, A and B are constant. Regression of the results shown in Figure 20 by the least-squares method yields $A = -1.56$ and $B = 0.82$. Therefore, $\Delta K_{II,drill}$ is expressed by the following equation.

$$\Delta K_{II,drill} = (-1.56 \cdot d + 0.82) \cdot \frac{4}{(2-\nu)\pi} \Delta\tau \sqrt{\pi\left(\frac{d}{2} + a'\right)} \quad \cdots\cdots (7)$$

Table 5 compares $\Delta K_{II,drill}$ calculated by FEM with $\Delta K_{II,drill}$ calculated by using equation (7) for each drilled hole size and load condition. When $d = 0.200$ mm and h' = 0.050 mm, i.e. h'/d is 0.25, for a condition that the edge depth is small compared to the drilled hole diameters, the prediction error becomes more than 10%. However, within the range of $0.5 \le h'/d \le 6.9$, the error was within approximately ± 5%. As described above, in the RCF test of the deep groove ball bearing in this study, ΔK_{II} of a crack generated from the drilled hole edge of the inner ring can be obtained relatively accurately by equation (7) under the conditions of 2.0 GPa $\le q_{max} \le$ 3.0 GPa, $d \le 0.2$ mm, $0.5 \le h'/d \le 6.9$, and $0.05 \le a'/d \le 0.2$. In this study, RCF tests are conducted by applying small drilled holes to the raceway of the rolling bearing. Most of these test conditions are within the range described above. In the following report, we discuss the quantitative evaluation of RCF strength on the basis of fracture mechanics by applying equation (7) to RCF test results.

5. Conclusion

In order to quantify the RCF test results of a deep groove ball bearing with a small drilled hole in the inner ring on the basis of the fracture mechanics, FEM stress analysis was used to calculate the mode II stress intensity factor range ΔK_{II} for a ring-shaped crack generated from the drilled hole edge. Using the obtained results and analytical solutions for penny-shaped cracks in an infinite body subjected to shear, an approximation formula is derived that can calculate the ΔK_{II} of ring-shaped cracks at the edges of drilled holes conveniently for various load conditions and drilled hole dimensions. In the process, the following findings were obtained.

(1) For combinations of JIS-SUJ2 steel balls with a diameter of 9.525 mm and raceway rings with a groove radius of curvature (R_{w1} = 18.49 mm, R_{w2} = –4.82 mm), ΔK_{II} of the penny-shaped cracks present under rolling contact stress with contact surface pressure q_{max} = 2.0–3.0 GPa was analyzed by FEM. As a result, it was found that ΔK_{II} can be predicted accurately by substituting the nominal stress at the crack depth into the analytical solution of a crack in a uniform stress field in the range of crack radius a up to about 0.1 mm. On the other hand, when a becomes larger than 0.1 mm, ΔK_{II} falls below the analytical solution, and the deviation between the two increases with increasing crack length.

(2) The ΔK_{II} of a ring-shaped crack at the edge of a drilled hole in a rolling contact stress field can be estimated with an error of about ±5% by multiplying ΔK_{II0} calculated from the analytical solution of a penny-shaped crack of the same size by correlation factor f_{drill} obtained as a function of only the drilled hole diameter.

Table 5 Mode II stress intensity factor range calculated by proposed formula

Diameter of drilled hole d [mm]	Depth of hole edge h' [mm]	h'/d	Maximum contact pressure q_{max} [GPa]	Mode II stress intensity factor range ΔK_{II} [MPa·m$^{1/2}$]		f_{drill} by eq. (6)	$\Delta K_{II,\ drill}$ by eq. (7)	Error in $\Delta K_{II,\ drill}$ (eq. (7) / FEM) [%]
				$\Delta K_{II,\ drill}$ (FEM solution of drilled hole edge under rolling contact stress)	$\Delta K_{II,\ Kassir}$ (Solution by Kassir & Sih at $\Delta\tau = 2\tau_{xz}$ under uniformly distributed stress)			
0.050	0.050	1.0	3.0	8.24	10.69	0.74	7.93	–3.7
			2.5	7.24	9.29	0.74	6.89	–4.8
			2.0	5.93	7.71	0.74	5.72	–3.5
0.100		0.5	3.0	9.85	14.00	0.66	9.29	–5.6
			2.5	8.49	12.16	0.66	8.08	–4.9
			2.0	7.15	10.10	0.66	6.71	–6.2
0.200		0.3	3.0	11.64	18.95	0.51	9.63	–17.3
			2.5	9.44	16.47	0.51	8.37	–11.4
			2.0	7.38	13.68	0.51	6.95	–5.9
0.050	0.100	2.0	3.0	8.87	11.78	0.74	8.74	–1.5
			2.5	7.37	9.72	0.74	7.21	–2.1
			2.0	5.72	7.48	0.74	5.55	–2.9
0.075		1.3	3.0	10.05	13.72	0.70	9.65	–4.0
			2.5	8.29	11.32	0.70	7.96	–4.0
			2.0	6.49	8.72	0.70	6.13	–5.5
0.100		1.0	3.0	10.62	15.42	0.66	10.24	–3.6
			2.5	8.85	12.73	0.66	8.45	–4.5
			2.0	6.91	9.80	0.66	6.51	–5.8
0.200		0.5	3.0	11.13	20.88	0.51	10.61	–4.7
			2.5	9.33	17.23	0.51	8.75	–6.2
			2.0	7.09	13.27	0.51	6.74	–4.9
0.050	0.220	4.4	3.0	6.97	9.80	0.74	7.27	4.3
			2.5	5.26	7.40	0.74	5.49	4.4
			2.0	3.65	5.12	0.74	3.80	4.0
0.100		2.2	3.0	8.24	12.83	0.66	8.52	3.4
			2.5	6.11	9.69	0.66	6.43	5.3
			2.0	4.26	6.70	0.66	4.45	4.4
0.200		1.1	3.0	8.28	17.37	0.51	8.82	6.6
			2.5	6.18	13.12	0.51	6.66	7.8
			2.0	4.24	9.07	0.51	4.61	8.7
0.050	0.345	6.9	3.0	5.30	7.45	0.74	5.53	4.3
			2.5	3.84	5.39	0.74	4.00	4.2
			2.0	2.55	3.57	0.74	2.65	3.9
0.100		3.5	3.0	5.98	9.75	0.66	6.47	8.3
			2.5	4.32	7.06	0.66	4.69	8.5
			2.0	2.87	4.67	0.66	3.10	8.1
0.200		1.7	3.0	6.24	13.20	0.51	6.71	7.5
			2.5	4.49	9.56	0.51	4.86	8.2
			2.0	2.97	6.33	0.51	3.21	8.2

References

1) Endo, M., Okazaki, S., Matsunaga, H., Moriyama, S., Munaoka, K., and Yanase, K., A new fatigue testing machine for investigating the behavior of small shear-mode fatigue cracks, Experimental Techniques, Vol. 40 (2015), pp. 1 065–1 073.
2) Fujimatsu, T., Nakamizo, T., Nakasaki, M., and Tsunekage, N., Crack initiation and propagation behavior around the defect in steel under rolling contact fatigue, ASTM International STP1580 Bearing Steel Technologies: 10th volume, Advances in Steel Technologies for Rolling Bearing (2015), pp. 147–172.
3) Ishida, M., Kiretsu no danseikaiseki to ouryokukakudaikeisuu, Second printing (1976), Baifukan (in Japanese).
4) Kassir, M. K. and Sih, G. C., Three-dimensional stress distribution around an elliptical crack under arbitrary loadings, *Journal of Applied Mechanics*, Vol. 33, issue 3 (1966), pp. 601–611.
5) Kida, K., Yamazaki, T., Shibata, M., Oguma, N., and Harada, H., Crack initiation from micro surface holes in bearings under rolling contact fatigue, *Fatigue & Fracture of Engineering Materials & Structures*, Vol. 27, No. 6 (2004), pp. 481–493.
6) Kida, K., Yoshidome, K., Yamakawa, K., Harada, H., and Oguma, N., Flaking failures originating from microholes of bearings under rolling contact fatigue, *Fatigue & Fracture of Engineering Materials & Structures*, Vol. 29, No. 12 (2006), pp. 1 021–1 030.
7) Komata, H., Yamabe, J., Fukushima, Y., and Matsuoka, S., Proposal of rolling contact fatigue crack growth test using a specimen with a small artificial hole, *Transactions of the Japan Society of Mechanical Engineers*, Series A, Vol. 78, No. 793 (2012), pp. 1 250–1 265 (in Japanese).
8) Komata, H., Yamabe, J., Matsunaga, H., Fukushima, Y., and Matsuoka, S., Effect of size and depth of small defect on the rolling contact fatigue strength of a bearing steel SUJ2, *Transactions of the Japan Society of Mechanical Engineers*, Series A, Vol. 79, No. 803 (2013), pp. 961–975 (in Japanese).
9) Lundberg, G. and Palmgren, A., Dynamic capacity of rolling bearings, *Acta Polytechnica Scandinavica-Mechanical Engineering Series*, Vol. 1, No. 3 (1947), pp. 5–50.
10) Matsunaga, H., Muramoto, S., Shomura, N., and Endo, M., Shear Mode Growth and Threshold of Small Fatigue Cracks in SUJ2 Bearing Steel, *Journal of the Society of Materials Science*, Vol. 58, No. 9 (2009), pp. 773–780 (in Japanese).
11) Matsunaga, H., Shomura, N., Muramoto, S., and Endo, M., Shear mode threshold for a small fatigue crack in a bearing steel, *Fatigue & Fracture of Engineering Materials & Structures*, Vol. 34 (2011), No. 1, pp. 72–82.
12) Mitamura, N., Rolling contact fatigue of rolling bearings and the research trend, *Journal of Japanese Society of Tribologists*, Vol. 53, No. 10 (2008), pp. 641–646 (in Japanese).
13) Murakami, Y., Hamada, S., Sugino, K., and Takao, K., New measurement method of mode II threshold stress intensity factor range ΔK_{rth} and its application, *Journal of the Society of Materials Science*, Vol. 43, No. 493 (1994), pp. 1 264–1 270 (in Japanese).
14) Murakami, Y., Fukuhara, T., and Hamada, S., Measurement of mode II threshold stress intensity factor range ΔK_{II}, *Journal of the Society of Materials Science*, Vol. 51, No. 8 (2002), pp. 918–925 (in Japanese).
15) Murakami, Y., Takahashi, K., and Kusumoto, R., Threshold and growth mechanism of fatigue cracks under mode II and III loadings, *Fatigue & Fracture of Engineering Materials & Structures*, Vol. 26 (2003), pp. 523–531.
16) Murakami, Y., Fukushima, Y., Toyama, K., and Matsuoka, S., Fatigue crack path and threshold in Mode II and Mode III loadings, *Engineering Fracture Mechanics*, Vol. 75 (2008), pp. 306–318.
17) Okazaki, S., Matsunaga, H., Ueda, T., Komata, H., and Endo, M., A practical expression for evaluating the small shear-mode fatigue crack threshold in bearing steel, *Theoretical and Applied Fracture Mechanics*, Vol. 73 (2014), pp. 161–169.
18) Okazaki, S., Wada, K., Matsunaga, H., and Endo, M., The influence of static crack-opening stress on the threshold level for shear-mode fatigue crack growth in bearing steels, *Engineering Fracture Mechanics*, Vol. 174 (2017), pp. 127–138.
19) Otsuka, A., Sugawara, H., Shomura, M., Aoyama, M., Yoo, S.K., and Shibata, M., Mechanism of rolling contact fatigue and mode II fatigue crack growth, *Journal of the Society of Materials Science*, Vol. 43, No. 484 (1994), pp. 55–61 (in Japanese).

Sho Hashimoto

Hiroki Komata

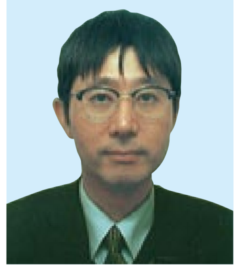

Hisao Matsunaga

Effect of Small Defect on the Flaking Strength of Rolling Bearings

(Part 2: Evaluation of the flaking strength of rolling bearing having a small drilled hole based on the stress intensity factor)

Sho Hashimoto, Hiroki Komata
Core Technology R&D Center, NSK Ltd.
Hisao Matsunaga
Kyushu Univ. Department of Mechanical Engineering
Kyushu Univ. Research Center for Hydrogen Industrial Use and Storage (HYDROGENIUS)
Kyushu Univ. International Institute for Carbon-Neutral Energy Research (I2CNER)

Abstract

Rolling contact fatigue (RCF) tests were conducted using rolling bearings with a micro-drilled hole on the raceway. In all the tests, fatigue crack initiated at the edge near the bottom of the hole and then propagated by shear mode. Even in the unbroken specimens tested up to $N = 1 \times 10^8$ cycles, a short fatigue crack was found at the edge. By using the stress intensity factor (SIF) range calculated for initial defect size, fatigue life data were uniformly gathered inside a small band irrespective of the diameter and depth of the hole. In addition, it was found that the crack size dependency of the threshold SIF range, which is well known for the mode I fatigue crack, also exists in the mode II fatigue crack emanating under the rolling contact. The values of threshold SIF ranges obtained by the RCF tests were in good agreement with those obtained in the torsional fatigue tests under static compression.

Keywords:

Rolling contact fatigue, Bearing steel, flaking, drilled hole, shear-mode crack, stress intensity factor

Translated and reprinted from the *Journal of the Japan Society of Mechanical Engineers*, Vol. 83, No. 852 (2017) (in Japanese), with permission from the Japan Society of Mechanical Engineers.

1. Introduction

The difficulty in predicting the position, dimensions, and shapes of the fracture origin and direct observations of the crack growth prevents elucidation of the phenomena of the subsurface originated flaking, where non-metallic defects are the fracture origin, located immediately below the raceway surface of the rolling bearing. In addition, much is unknown about the behavior of fatigue crack growth of the shear mode (modes II and III), which governs most of the damage process.

Various test methods have been used to investigate the growth behavior and lower limits of shear-mode fatigue cracks in high hardness steel by Murakami et al. (Murakami et al., 1994, 2002, Murakami et al., 2003, 2008), Otsuka et al. (Otsuka et al., 1994), and Matsunaga et al. (Matsunaga et al., 2011, Okazaki et al., 2014, 2017, Endo et al., 2015). However, these methods are incapable of reliably reproducing the stress field under rolling contact stress, and problems remain regarding its application to rolling contact fatigue (RCF) strength evaluation. On the other hand, there was an attempt to make it easier to observe cracks by limiting the crack initiation point by introducing micro-defects into the raceway of the RCF test piece and to quantify flaking strength by fracture mechanics (Kida et al., 2004, 2006, Fujimatsu et al., 2015). The authors (Komata et al., 2012, 2013) have also conducted RCF tests using a JIS-SUJ2 flat plate test piece with a micro-drilled hole as an artificial defect in the raceway and investigated the crack growth behavior and its influencing factors. Thus far, it has been shown that RCF tests with micro-drilled holes are useful for investigating the growth characteristics of shear-mode fatigue cracks and that the RCF limit as the lower limit of the growth of fatigue cracks can be quantitatively evaluated by considering the influencing factors such as micro-defect size and crack depth. However, in order to actually apply this evaluation method to the evaluation of the flaking strength of rolling bearings, it is required to investigate the mechanical condition of the crack generated from the drilled hole in more detail and clarify the difference with the mechanical condition of the crack generated from non-metallic inclusions. In addition to the RCF tests using a flat plate test piece, it is also essential to investigate the effectiveness and applicable range of the evaluation methods by conducting actual rolling bearing tests.

Therefore, in this study, RCF tests are conducted by applying drilled holes to raceway of the rings of radial-type, single-row deep groove ball bearings and thrust-type, single-row ball bearings. In this way, the effect of micro-defects on flaking strength is investigated at the actual machine level. In the first report (Hashimoto et al., 2017), in order to fracture-mechanically quantify the results of an RCF test of a deep groove ball bearing with micro-drilled holes in the inner ring, the mode II stress intensity factor range of the ring-shaped cracks generated from the edge of the drilled hole was analyzed by FEM. Using the obtained results and analytical solutions for penny-shaped cracks in an infinite body subject to shear, an approximate formula is derived that can calculate the stress intensity factor ranges of ring-shaped cracks at the edge of the drilled hole easily for various load conditions and drilled hole dimensions. In this report, we apply this approximate formula to fatigue test results and quantify the effect of micro-defects on the flaking strength as a crack problem.

2. Rolling Contact Fatigue Test of Rolling Bearings with Micro-Drilled Holes

2.1 Experimental procedures

Figure 1 shows a schematic diagram of a rolling bearing and fatigue test rigs used for an RCF test. The rolling bearings used in this test were a radial-type, single row deep groove ball bearing JIS-6206 and a thrust-type, single-row ball bearing JIS-51305, both made of JIS-SUJ2. The inner ring of JIS-6206 and the outer ring of JIS-51305 were evaluated. Table 1 shows the respective chemical compositions. The rolling elements are steel balls with a diameter of 9.525 mm. A heat treatment of hardening and tempering has been applied to the raceway rings and the steel balls. Grinding processing was applied to the raceway surface after heat treatment, and the roughness after processing was about 0.03–0.04 μmRa. The Vickers hardness was measured at two points with a test load of 9.8 N for each of five randomly selected raceways, for a total of 10 points. As a result, HV = 751 on average for the JIS-6206 inner ring and HV = 754 on average for JIS-51305 outer ring.

As shown in Figure. 2 (a), in the ball bearing, the contact area generated by the compressive contact between the steel ball and the raceway ring has an elliptical shape centered on the groove bottom of the raceway. At this time, the maximum contact surface pressure occurs at the center of the contact ellipse (that is, at the groove bottom of the raceway). In the center of the raceway, a micro-drilled hole as shown in Figure. 2 (b) was introduced as a crack-starter. As shown in Figure. 2 (c), the drilled hole diameter d was set at three levels of 0.05 mm, 0.08 mm, and 0.1 mm, and the edge depth h' was varied in the range of 0.05 mm to 0.175 mm. The maximum contact surface pressure q_{max} was also varied in the range of 2.5 GPa to 3.4 GPa. Lubricant used was industrial-use lubricating mineral oil of ISO-VG68 in all tests, forced circulation oil lubrication for JIS-6206, and oil bath lubrication for JIS-51305. The rotating speed was 3900 rpm for JIS-6206 and 1000 rpm for JIS-51305.

After the RCF test, cross sections of the drilled holes of all the raceways were observed regardless of whether they were broken or not. As shown in Figure 3, the observed cross section was a plane perpendicular to the raceway surface passing through the center of the raceway. Cracks were observed after the cross section where the center of the drilled holes appeared to be polished to a mirror surface. Figure 4 shows an example of observation of a raceway before and after an RCF test. The crack was initiated from the edge of the drilled hole and eventually reached the raceway surface, causing flaking. At the time, portions deeper than the edges had remained in the raceway. The number of cycles N (the number of times the rolling element passes over the drilled hole) at which flaking occurred in the RCF test is defined as the fatigue life N_f. If the flaking did not occur even when $N = 1 \times 10^8$, the fatigue test was terminated.

Table 1 Chemical composition of the tested bearing (mass %)

Element	C	Si	Mn	Cr	P	S	Ni	Cu	Mo
6206	0.98	0.23	0.36	1.43	0.014	0.004	0.02	0.004	0.01
51305	1.03	0.26	0.33	1.33	0.010	0.004	0.02	0.002	0.01

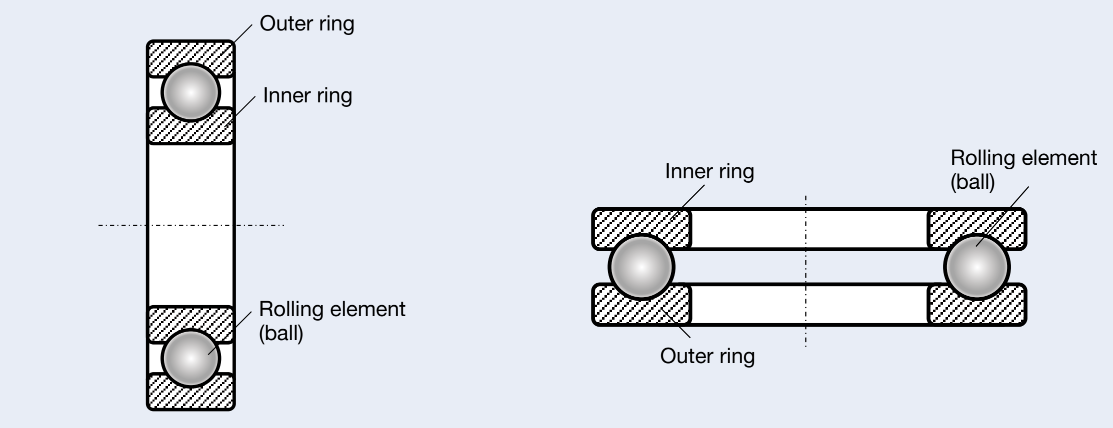

(a-1) Deep groove ball bearing

(a-2) Thrust ball bearing

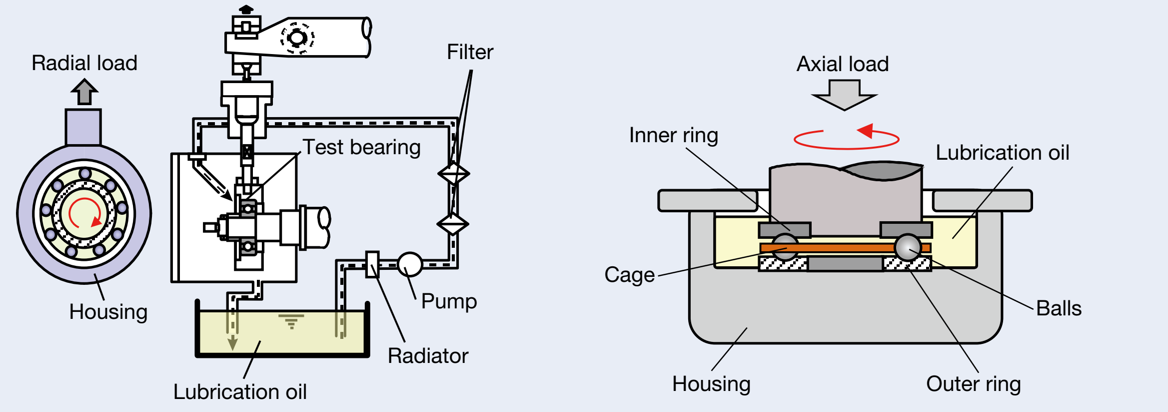

(b-1) Rigs for the fatigue test of deep groove ball bearing

(b-2) Rigs for the fatigue test of thrust ball bearing

Fig. 1 Schematic of the rolling bearings and rigs for the fatigue test.

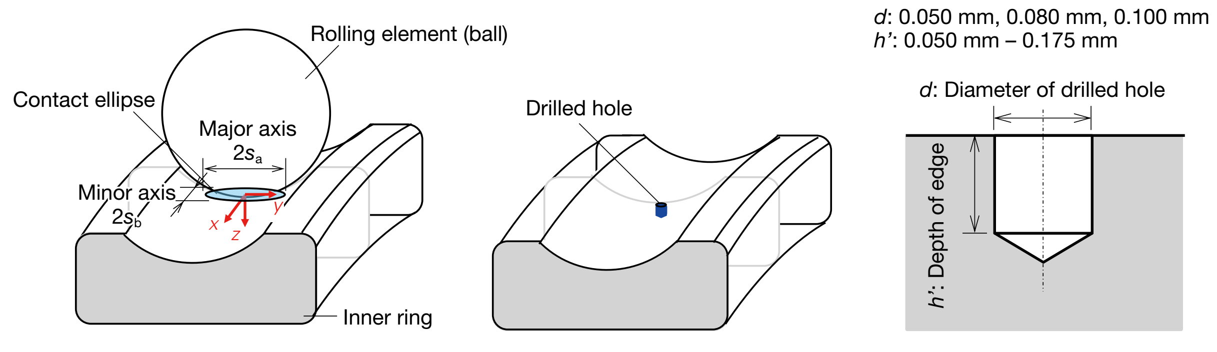

(a) Ellipse type contact area

(b) Position of drilled hole on raceway

(c) Geometry of drilled hole

Fig. 2 Contact between ball and raceway and drilled hole. A drilled hole was introduced onto the center of contact ellipse as a crack starter.

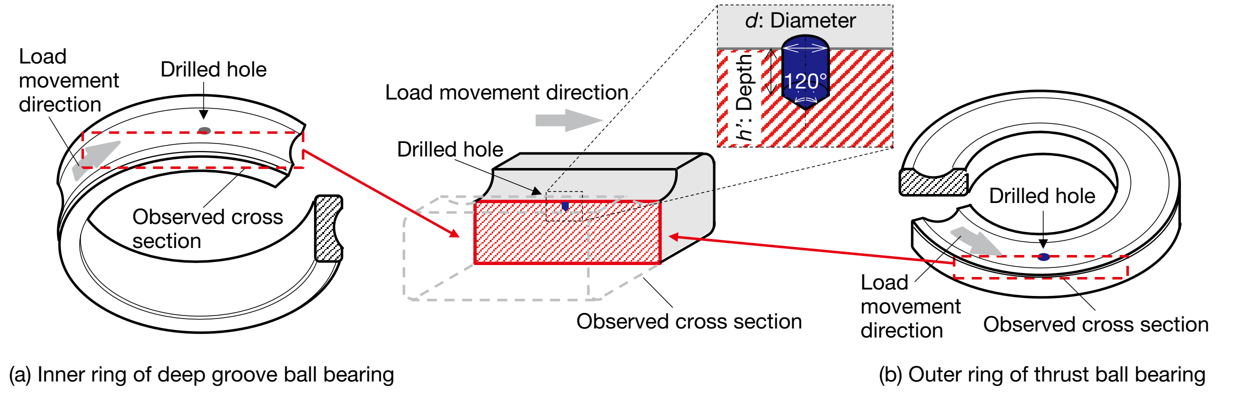

(a) Inner ring of deep groove ball bearing

(b) Outer ring of thrust ball bearing

Fig. 3 Observed cross section.

2.2 Experimental results

Figure 5 shows examples of cross section observations. In each of the test pieces, the cracks initiated from the edge of the drilled hole, propagated almost parallel to the surface, then bent upward and finally reached the surface. This fracture mode is similar to the previous test results (Komata et al., 2012, 2013) conducted by the authors using flat plate test pieces. That is to say, even in this experiment using an actual rolling bearing, it is considered that the crack propagated in the shear mode from the drilled hole edge. Figure 6 shows the relationship between the maximum contact surface pressure q_{max} and the fatigue life N_f. Figure 6 also shows the results of an RCF test performed by the authors in the past using flat plate test pieces (Komata et al., 2012, 2013). N_f increased with decreasing q_{max}, similar to the test results of the flat plate test pieces by Komata et al. However, test results of the rolling bearing and the flat plate test pieces do not coincide, and the life of the former is shorter than the life of the latter. The fatigue life also varies depending on the diameter and depth of the drilled hole.

As shown in the previous report, when a penny-shaped crack exists immediately below the rolling contact portion, the crack is considered to be sufficiently small in comparison with the rolling contact stress field if the crack diameter is 0.2 mm or less, and the stress intensity factor can be estimated by the analytical solution as the nominal shear stress for the stress at the crack depth relatively accurately. Furthermore, since the diameter of drilled holes used in this study is 0.05 mm – 0.1 mm, it is considered that the stress intensity factor for the crack generated from the drilled hole is also well correlated with the nominal shear stress at the edge depth h' in the early stage of the crack growth. Therefore, the fatigue test results are summarized by using the nominal shear stress amplitudes τ_a acting at the edge depth h' of each drilled hole. Figure 7 shows the relationship between τ_a and N_f. Here, an alternating shear stress acts on the inside of inner ring as the steel ball passes. From Figure 7 it can be seen that by using τ_a on the vertical axis of the fatigue life diagram, the variation in test results becomes smaller compared to Figure 6. In addition, the smaller the diameter of the drilled hole, the longer the fatigue life.

Komata et al. have shown in previous studies that cracks occur at cycles of 5% or less of the fatigue life in RCF tests with micro-drilled holes (Komata et al., 2013). In other words, most of the RCF life when the micro-drilled hole is the starting point is spent on crack growth. In the fatigue test results shown in Figure 7, the life is longer for the smaller diameter of the drilled hole, probably due to the difference in the mechanical conditions of the small cracks generated from the drilled hole edge. Hence, it is presumed that the smaller the drilled hole diameter, the smaller the stress intensity factor at the time of crack initiation and the longer the crack growth life, accordingly. In the next section, we attempt to quantify the RCF test results using the approximation formula for the mode II stress intensity factor range of ring-shaped cracks emanating around the edge of the drilled hole under rolling contact as proposed in the previous report.

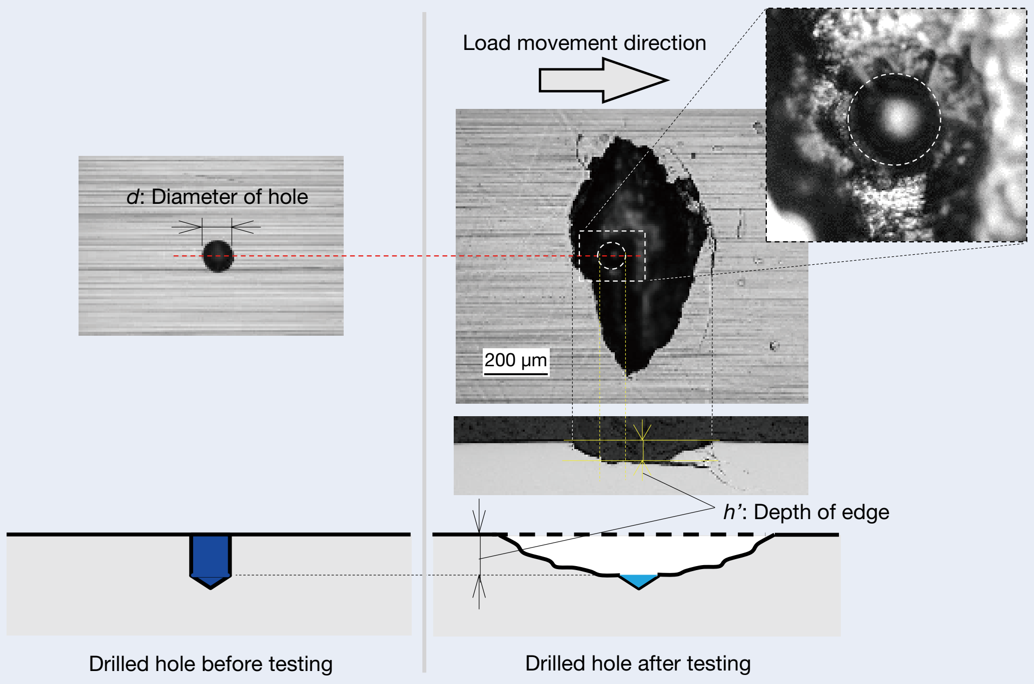

Fig. 4 Examples of the observation of cross section after RCF test (inner ring of JIS-6206, d = 0.100 mm, h' = 0.063 mm, q_{max} = 3.0 GPa, N_f = 2.8 × 10^7). The fatigue crack was initiated from the edge of drilled hole.

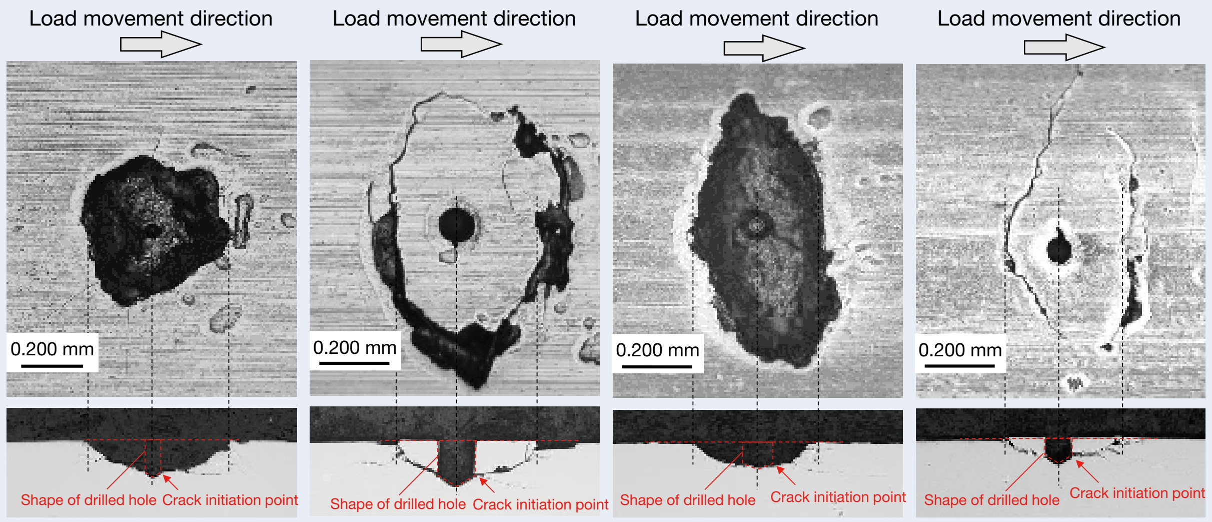

(a) Inner ring of JIS-6206
d = 0.05 mm,
h' = 0.111 mm,
q_{max} = 3.0 GPa,
N_f = 2.2 × 10^7 cycles

(b) Inner ring of JIS-6206
d = 0.1 mm,
h' = 0.122 mm,
q_{max} = 2.8 GPa,
N_f = 1.1 × 10^7 cycles

(c) Outer ring of JIS-51305
d = 0.1 mm,
h' = 0.072 mm,
q_{max} = 3.0 GPa,
N_f = 1.0 × 10^7 cycles

(d) Outer ring of JIS-51305
d = 0.08 mm,
h' = 0.070 mm,
q_{max} = 3.0 GPa,
N_f = 2.9 × 10^7 cycles

Fig. 5 Optical micrographs of flakings and cross sections containing the drilled hole. The crack was initiated at the edge of drilled hole, and then propagated parallel to the raceway.

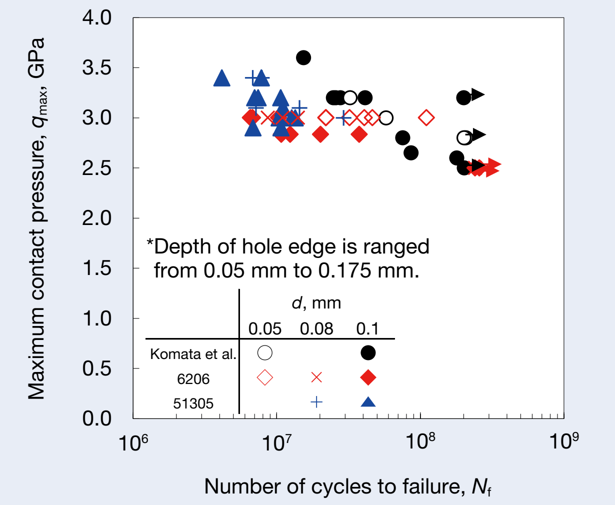

Fig. 6 Relationship between maximum contact pressure q_{max} and fatigue life N_f. The fatigue life was greatly varied depending on the diameter and depth of drilled hole.

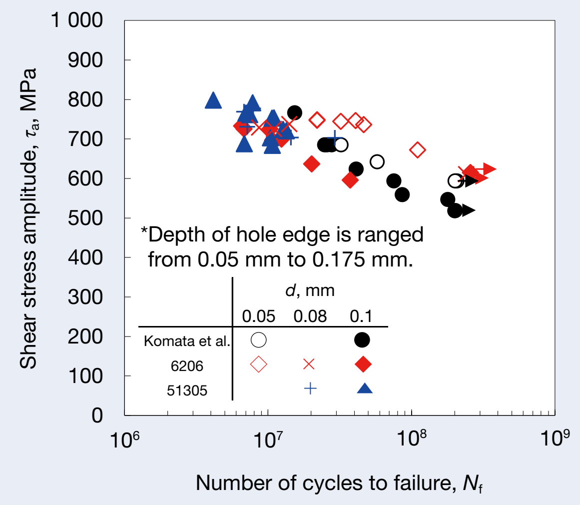

Fig. 7 Relationship between shear stress amplitude τ_a and fatigue life N_f. Smaller hole diameter led to longer fatigue life.

3. Quantitative evaluation of rolling contact fatigue strength based on stress intensity factor

When an elliptical crack is subjected to shear, the deformation mode of the crack changes from mode II to mixed mode (mode II + mode III) to mode III along the crack leading edge. For example, in an elliptical crack subjected to shear, as shown in Figure 8 (a), at points X_1 and X_2, which are the points of intersection of the crack leading edge and the x-axis, the deformation mode is pure mode II, K_{II} becomes maximum ($= K_{II\ max}$), and K_{III} becomes 0. In addition, at points Y_1 and Y_2, which are the points of intersection of the crack leading edge and y-axis, the deformation mode is pure mode III, K_{III} becomes maximum ($= K_{III\ max}$), and K_{II} becomes 0. Also, as shown in Figure 8 (b), K_{II} and K_{III} are maximized at similar positions for small cracks generated from the edges of the drilled holes, respectively.

Murakami et al. (Murakami et al., 2003, 2008) hypothesized that the shear stress distribution near the crack tip when $K_{II} = K_{III}$ is the same for mode II and mode III cracks, except that the directions of the shear stress differ by 90° and that they are $K_{IIth} = K_{IIIth}$ for the same materials. In addition, experimental results supporting the above hypothesis were obtained by a mode II fatigue crack growth test and a mode III fatigue crack growth test on carbon steel. Matsunaga et al. (Matsunaga et al., 2009) also obtained experimental results showing that the fatigue crack growth resistances of mode II and mode III are nearly equal for minute shear-mode fatigue cracks in bearing steel. In this experiment, when the lengths a' and b' of ring-shaped cracks emanating around the drilled hole are sufficiently small compared to the drilled hole diameter, the aspect ratio of the crack including the drilled hole can be regarded as $a / b \approx 1$, and the stress field becomes $K_{II\ max} > K_{III\ max}$ at this time. Therefore, if the crack growth resistances of mode II and mode III are equal, it is expected that the growth of mode II in the x direction becomes dominant in the initial stage of crack growth from the drilled hole. For the reason above, K_{II} at the point of intersection of the leading edge of the crack and the x-axis is used as an index to quantify the initial growth and non-propagation condition of cracks generated at the edge of the drilled hole.

In the first report, the mode II stress intensity factor K_{II} of the small cracks generated from the edges of the micro-drilled holes under the rolling contact were analyzed by FEM. A raceway of a rolling bearing with micro-drilled holes, as shown in Figure 8 (b), was modeled, and a simulated steel ball was passed over its surface while compressive contact, then $\Delta K_{II,\ drill}$ was obtained from the changes in K_{II}. At this time, it has also been confirmed that the contact stress conditions occurring in the ball bearing can be reproduced by FEM, equivalent to the exact solution of Lundberg (Lundberg and Palmgren, 1947). It was also revealed that $\Delta K_{II,\ drill}$ of small cracks generated from drilled-holes of various diameters and depths were correlated with ΔK_{II0} of cracks in an infinite body under uniform shear through the intermediary of a correlation factor, f_{drill}. The relationship between $\Delta K_{II,\ drill}$ and ΔK_{II0} is given by the following formula.

$$\Delta K_{II,drill} = f_{drill} \cdot \Delta K_{II0} = f_{drill} \cdot \frac{4}{(2-\nu)\pi}\,\Delta\tau\,\sqrt{\pi\left(\frac{d}{2}+a'\right)} \qquad \cdots\cdots (1)$$

Where ν is the Poisson's ratio, $\Delta\tau$ is the shear stress range ($\Delta\tau = 2\tau_a$), and a' is the length of the crack generated from the drilled hole edge. τ_a is the nominal shear stress amplitude acting on the drilled hole edge depth h'. f_{drill} is a function of the drilled hole diameter d, represented by the following equation:

$$f_{drill} = -1.56 \cdot d + 0.86 \qquad \cdots\cdots\cdots\cdots (2)$$

The applicable range of the equation (1) is the range of the analysis performed in the first report, i.e., $0 < d \leq 0.2$ mm, $0 < h' \leq 0.345$ mm, 2.0 GPa $\leq q_{max} \leq$ 3.0 GPa. In this range, $\Delta K_{II,drill}$ obtained by equation (1) falls within an error of approximately ± 5% with respect to the value obtained by FEM analysis.

As described in Section 2, in the RCF fracture process starting from the edge of the drilled hole, a crack occurs at cycles of 5% or less of the fatigue life, and most of the fatigue life is spent on the growth of the crack. Therefore, we use $\Delta K_{II,drill}$, which represents the dynamic state of such a crack, to organize fatigue life data. Figure 9 shows the relationship between $\Delta K_{II,drill}$ and N_f. Figure 9 does not include the data in which the size of the drilled hole is out of the application range of equation (1). It is noted that $\Delta K_{II,drill}$ was calculated for the initial defect size, i.e. the length of the ring-shaped crack, a', was assumed to be zero in Eq. (1). This approximation is reasonable because the fatigue strength is determined by propagation or non-propagation of a short crack, whose length a' is not predetermined but is substantially small compared to the hole diameter, d. In Figure 7 using τ_a as the vertical axis, the test results varied depending on the diameter of the drilled hole, but in Figure 9 using $\Delta K_{II,drill}$ as the vertical axis, all the fatigue life data were uniformly gathered inside a narrow band, irrespective of the diameter and depth of the hole.

Figure 10 shows the results of cross-sectional observation of the drilled holes of the un-flaked rolling bearing tested up to $N = 1 \times 10^8$ cycles. Small cracks were observed at the edge of the drilled hole. It was assumed that these cracks were non-propagation, or propagation at an extremely slow growth rate enough to be considered as non-propagation. Namely, it is considered that $\Delta K_{II,drill}$ obtained for an unbroken rolling bearing with $N = 1 \times$

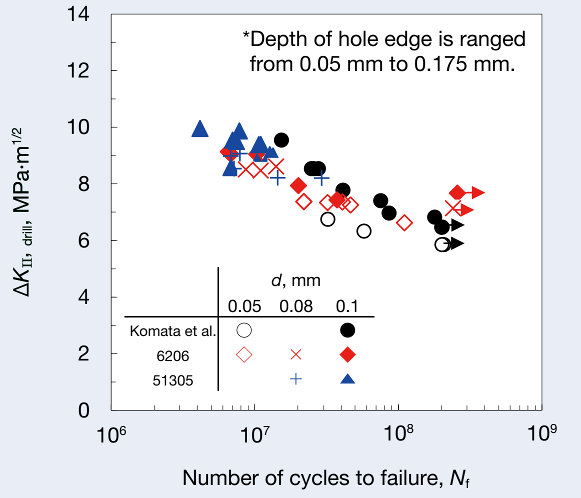

Fig. 9 Relationship between stress intensity factor range $\Delta K_{II,\ drill}$ and fatigue life N_f. By using $\Delta K_{II\ drill}$, fatigue life data were uniformly gathered inside a small band irrespective of the diameter and depth of the hole.

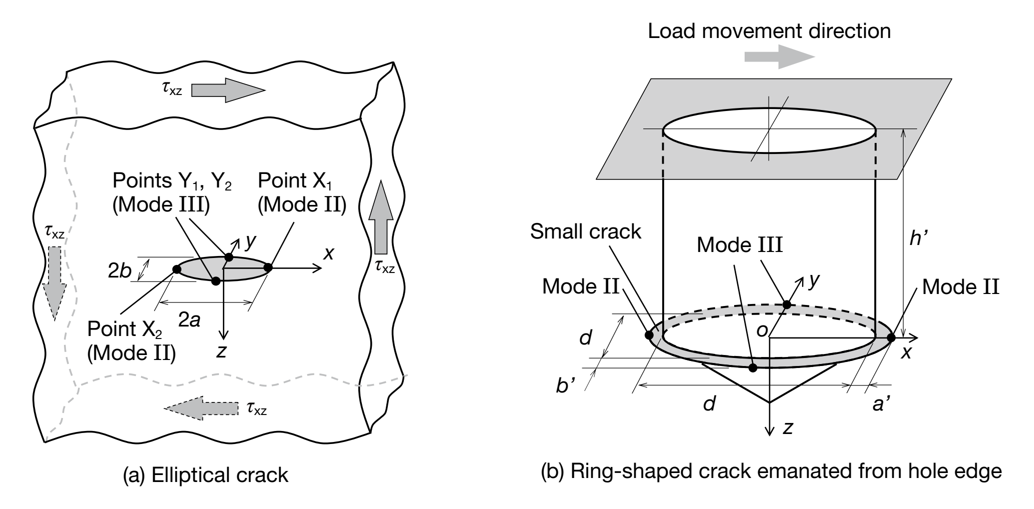

(a) Elliptical crack

(b) Ring-shaped crack emanated from hole edge

Fig. 8 Crack geometries under shear. The crack is deformed by pure mode II at the points X_1 and X_2, and is by pure mode III at the points Y_1 and Y_2.

10^8 cycles is almost equal to the lower limit of the growth of a crack generated from a drilled hole. Therefore, the $\Delta K_{\mathrm{II,\,drill}}$ obtained for these test conditions was treated as a Mode II threshold SIF range, ΔK_{IIth}. Figure 7 shows the relationship between ΔK_{IIth} and the diameter of the drilled hole d. ΔK_{IIth} increases with increasing drilled hole diameter.

Matsunaga et al. (Matsunaga et al., 2011, Okazaki et al., 2014) conducted a torsional fatigue test under static compressive stress by applying artificial small-defects as the origin of crack to the surface of a round bar test piece made of bearing steel SUJ2 similar to the test material used in this study. Then, the growth behavior of half elliptical shear-mode fatigue crack generated from defects was investigated, which revealed that the threshold stress intensity factor range of the small shear-mode fatigue crack, $\Delta K_{\tau\mathrm{th}}$, has a crack size dependency similar to that of the Mode I threshold in the crack size range of 1 mm or less in total length. Furthermore, Matsunaga et al. have shown that $\Delta K_{\tau\mathrm{th}}$ is proportional to the 1/3 power of the size of a crack and have obtained equation (3).

$$\Delta K_{\tau\mathrm{th}} = 1.26(f+1.33)(\sqrt{area})^{1/3} \qquad \text{............ (3)}$$

Here, $\sqrt{area}$ (μm) is the square root of the crack area including the artificial defect. f is the ratio of $area_{\mathrm{crack}}$ to the area of the entire crack ($area_{\mathrm{defect}} + area_{\mathrm{crack}}$) when the area of the crack part is taken as $area_{\mathrm{crack}}$ and the area of the artificial defect part as $area_{\mathrm{defect}}$ and is expressed by the following equation.

$$f = \frac{area_{\mathrm{crack}}}{area_{\mathrm{defect}} + area_{\mathrm{crack}}} \qquad \text{............ (4)}$$

Equation (3) and (4) were used to calculate $\Delta K_{\tau\mathrm{th}}$ for the dimensions of the respective drilled holes used in this study. As shown in Figure 10, the crack length observed at the edge of the drilled hole of unbroken bearing is sufficiently small with respect to the diameter of the drilled hole. Therefore, the size of the crack for calculation $\sqrt{area}$ is the square root of the area where the drilled hole is projected on the raceway surface. This is represented by equation (5).

$$\sqrt{area} = \sqrt{\pi d^2/4} \qquad \text{............ (5)}$$

Here, since the crack area $area_{\mathrm{crack}}$ << drilled hole area $area_{\mathrm{defect}}$, $f << 1$. Therefore, f is assumed to be zero in equation (3), and $\Delta K_{\tau\mathrm{th}}$ is evaluated as follows.

$$\Delta K_{\tau\mathrm{th}} = 1.61 \cdot d^{1/3} \qquad \text{............ (6)}$$

Figure 11 shows the result of calculating $\Delta K_{\tau\mathrm{th}}$ as a function of d using the equation (6) by a solid line. The $\Delta K_{\tau\mathrm{th}}$ (symbol: ●) obtained by equation (1) with the condition of the test that was unbroken at $N = 1 \times 10^8$ cycles and $\Delta K_{\tau\mathrm{th}}$ (solid line) obtained by equation (6) almost coincided. In other words, it was revealed that the $\Delta K_{\tau\mathrm{th}}$ of the micro fatigue crack generated from the drilled hole under rolling contact was also proportional to the 1/3 power of the initial defect size, similarly to the mode I fatigue crack and the shear-mode fatigue crack propagated in the torsional fatigue test under static compression. In addition, it was also shown that ΔK_{IIth} of a micro fatigue crack generated from a drilled hole was predictable using evaluation equation obtained from the results of torsional fatigue tests under static compression.

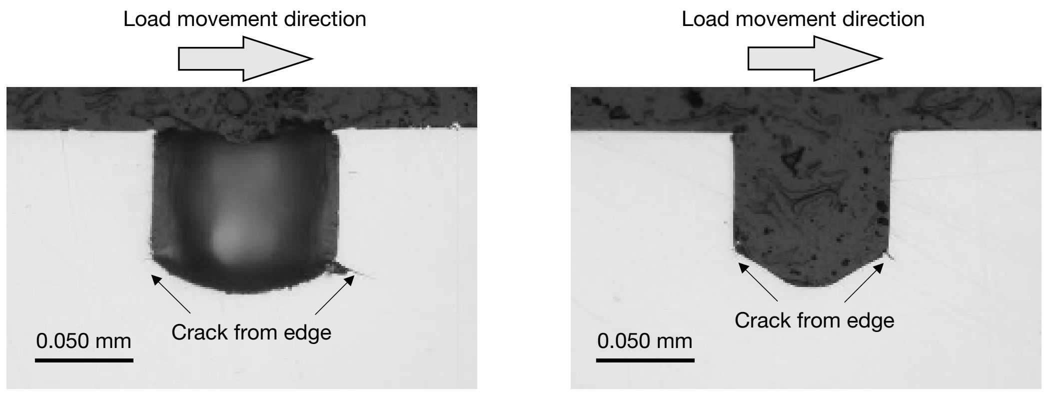

(a) Inner ring of JIS-6206
d = 0.100 mm, h' = 0.064 mm,
$q_{\max}$ = 2.5 GPa, $N = 2.6 \times 10^8$ cycles

(b) Inner ring of JIS-6206
d = 0.080 mm, h' = 0.060 mm,
$q_{\max}$ = 2.5 GPa, N = 2.4×10^8 cycles

Fig. 10 Optical micrographs of drilled holes with small cracks in unbroken bearings. Small cracks were observed at the edge.

From the results described above, it is expected that the threshold of the growth of a shear-mode fatigue crack is proportional to the 1/3 power of the defect size, even when small non-metallic inclusions in the material are the origins of the crack. However, as illustrated in Figure12, non-metallic inclusions as the origins of flaking failure in the rolling bearing vary in their shape. In order to realize highly accurate predictions of flaking strength, it is required to investigate the stress intensity factors of cracks initiated and propagated from small defects of various shapes and materials. A future objective of this research is thus to establish a means to evaluate flaking strength quantitatively when non-metallic inclusions are the origins of failure.

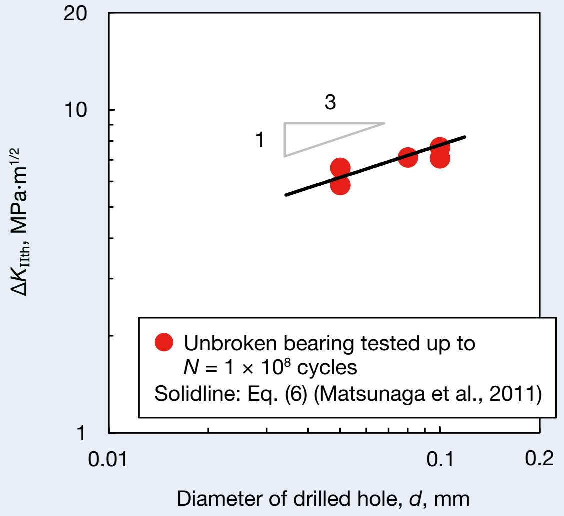

Fig. 11 Relationship between mode II threshold stress intensity factor range, ΔK_{IIth}, and the diameter of the drilled hole, d. The crack size dependency of threshold SIF range, which is well-known for mode I fatigue crack, also exists in mode II fatigue crack emanating under the rolling contact.

4. Conclusion

RCF tests were carried out by applying various micro-drilled holes with different diameters and depths to the raceways of JIS-6206 and JIS-51305 in order to quantitatively evaluate flaking strength of the subsurface-originated type of a rolling bearing. In the obtained test results, quantitative evaluation according to fracture mechanics principles was attempted using the mode II stress intensity factor range $\Delta K_{\mathrm{II,drill}}$ of the ring-shaped cracks, which emanated at the edges of the drilled holes. The conclusions can be summarized as follows.

(1) Even when a micro-drilled hole was applied to a rolling bearing, all the fatigue cracks initiated at the edges of the drilled holes, later propagating by shear-mode, as in the case of the flat plate test piece.
(2) The fatigue life data were uniformly gathered inside a narrow band, irrespective of the diameters and depths of the holes, by using the mode II stress intensity factor range of the ring-shaped cracks, which originated around the edges of drilled holes for the vertical axis.
(3) In the un-flaked rolling bearing tested up to $N = 1 \times 10^8$ cycles, short fatigue cracks were discovered at the edges of the drilled holes. This result indicates that the flaking limit of rolling bearings was not a crack initiation limit but rather a non-propagation limit of a fatigue crack.
(4) From the condition of the test in which the rolling bearing was un-flaked, the limit of the crack growth ΔK_{IIth} was calculated and plotted against the drilled hole diameter (i.e., crack diameter), and it was revealed

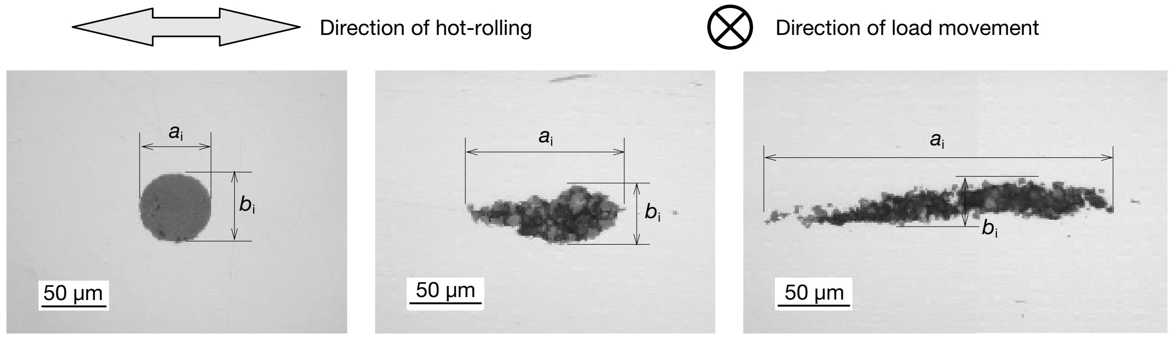

(a) Aspect ratio: 1
(b) Aspect ratio: 2.5
(c) Aspect ratio: 7

Fig. 12 Non-metallic inclusions observed in a bearing steel. (a_i: major axis of inclusions, b_i: minor axis of inclusions, aspect ratio: a_i / b_i)
The non-metallic inclusions have various shapes with different aspect ratios.

that ΔK_{IIth} was proportional to the 1/3 power of the drilled hole diameter d. In addition, the values of the ΔK_{IIth} obtained from the RCF tests were in good agreement with those obtained in the torsional fatigue tests under static compression.

References

1) Fujimatsu, T., Nakamizo, T., Nakasaki, M., and Tsunekage, N., Crack initiation and propagation behavior around the defect in steel under rolling contact fatigue, *ASTM International STP1580 Bearing Steel Technologies*: 10th Volume, Advances in Steel Technologies for Rolling Bearing (2015), pp. 147–172.
2) Kassir, M.K. and Sih, G.C., Three-dimensional stress distribution around an elliptical crack under arbitrary loadings, *Journal of Applied Mechanics*, Vol. 33, issue 3 (1966), pp. 601–611.
3) Kida, K., Yamazaki, T., Shibata, M., Oguma, N., and Harada, H., Crack initiation from micro surface holes in bearings under rolling contact fatigue, *Fatigue & Fracture of Engineering Materials & Structures*, Vol. 27, No. 6 (2004), pp. 481–493.
4) Kida, K., Yoshidome, K., Yamakawa, K., Harada, H., and Oguma, N., Flaking failures originating from microholes of bearings under rolling contact fatigue, *Fatigue & Fracture of Engineering Materials & Structures*, Vol. 29, No. 12 (2006), pp. 1 021–1 030.
5) Komata, H., Yamabe, J., Fukushima, Y., and Matsuoka, S., Proposal of rolling contact fatigue crack growth test using a specimen with a small artificial hole, Transactions of the Japan Society of Mechanical Engineers, Series A, Vol. 78, No. 793 (2012), pp. 1 250–1 265 (in Japanese).
6) Komata, H., Yamabe, J., Matsunaga, H., Fukushima, Y., and Matsuoka, S., Effect of size and depth of small defect on the rolling contact fatigue strength of a bearing steel SUJ2, *Transactions of the Japan Society of Mechanical Engineers*, Series A, Vol. 79, No. 803 (2013), pp. 961–975 (in Japanese).
7) Lundberg, G. and Palmgren, A., Dynamic capacity of rolling bearings, Acta Polytechnica Scandinavica-Mechanical Engineering Series, Vol. 1, No. 3 (1947), pp. 5–50.
8) Matsunaga, H., Muramoto, S., Shomura, N., and Endo, M., Shear mode growth and threshold of small fatigue cracks in SUJ2 bearing steel, *Journal of the Society of Materials Science*, Vol. 58, No. 9 (2009), pp. 773–780 (in Japanese).
9) Matsunaga, H., Shomura, N., Muramoto, S., and Endo, M., Shear mode threshold for a small fatigue crack in a bearing steel, *Fatigue & Fracture of Engineering Materials & Structures*, Vol. 34 (2011), No. 1, pp. 72–82.
10) Mitamura, N., Rolling contact fatigue of rolling bearings and the research trend, *Journal of Japanese Society of Tribologists*, Vol. 53, No. 10 (2008), pp. 641–646.
11) Murakami, Y., Hamada, S., Sugino, K., and Takao, K., New measurement method of mode II threshold stress intensity factor range $\Delta K_{\tau\mathrm{th}}$ and its application, *Journal of the society of materials science*, Vol. 43, No. 493 (1994), pp. 1 264–1 270 (in Japanese).
12) Murakami, Y., Fukuhara, T., and Hamada, S., Measurement of mode II threshold stress intensity factor range ΔK_{II}, *Journal of the Society of Materials Science*, Vol. 51, No. 8 (2002), pp. 918–925 (in Japanese).
13) Murakami, Y., Takahashi, K., and Kusumoto, R., Threshold and growth mechanism of fatigue cracks under mode II and III loadings, *Fatigue & Fracture of Engineering Materials & Structures*, Vol. 26 (2003), pp. 523–531.
14) Murakami, Y., Fukushima, Y., Toyama, K., and Matsuoka, S., Fatigue crack path and threshold in Mode II and Mode III loadings, *Engineering Fracture Mechanics*, Vol. 75 (2008), pp. 306–318.
15) Okazaki, S., Matsunaga, H., Ueda, T., Komata, H., and Endo, M., A practical expression for evaluating the small shear-mode fatigue crack threshold in bearing steel, *Theoretical and Applied Fracture Mechanics*, Vol. 73 (2014), pp. 161–169.
16) Okazaki, S., Wada, K., Matsunaga, H., and Endo, M., The influence of static crack-opening stress on the threshold level for shear-mode fatigue crack growth in bearing steels, *Engineering Fracture Mechanics*, Vol. 174 (2017), pp. 127–138.
17) Otsuka, A., Sugawara, H., Shomura, M., Aoyama, M., Yoo, S.K., and Shibata, M., Mechanism of rolling contact fatigue and mode II fatigue crack growth, *Journal of the Society of Materials Science*, Vol. 43, No. 484 (1994), pp. 55–61 (in Japanese).

Sho Hashimoto

Hiroki Komata

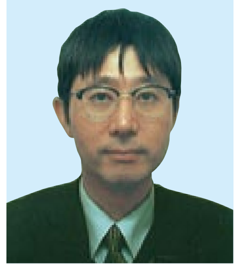

Hisao Matsunaga

X-Ray CT Imaging of Grease Behavior in Ball Bearing and Numerical Validation of Multi-Phase Flows Simulation

Takashi Noda[*]*, Kenichi Shibasaki*
Basic Technology Research Center, NSK Ltd.
Shinji Miyata
Development Department 1, Future Technology Development Center, NSK Ltd.
Masato Taniguchi
NSK Institute of Technology, NSK Ltd.

Abstract

In an effort to further extend bearing life, the authors have attempted to acquire greater knowledge regarding lubricating grease behavior in a bearing. While conducting experiments, some kinds of difficulties commonly arise when attempting to observe grease behavior directly from the bearing exterior without removing seals and shields. Making a breakthrough such a troubling aspect, X-ray computed tomography (CT), which is one of the non-destructive inspection techniques, was employed and resulted in visualizing remarkable details of grease distribution in a resin ball bearing. Hydrodynamic grease transition from churning to channeling state was well revealed by the mixture distribution of urea and barium-based greases which have different properties of X-ray absorption capability. Furthermore, the three dimensional unsteady liquid-gas multi-phase flows analysis was performed. Hydrodynamic feature of grease was regarded as a non-Newtonian fluid, which shows a highly non-linear flow curve, and the constitutive equation of modified Bingham plastic model proposed by Papanastasiou was applied to rheological property. Through these novel experimental and calculation approaches, several new insights about grease behavior inside a ball bearing were brought out.

Keywords

ball bearing, grease, X-ray CT, non-Newtonian fluid, Bingham plastic, computational fluid dynamics

Reprinting of this article was approved by the Japanese Society of Tribologists for publication in *Tribology Online*, Vol. 15, No. 1 (2020), pp. 36–44.

1. Introduction

Lubricants, such as oil and grease are used in rolling bearings to prevent metallic contact between rolling elements and the raceway surface. Approximately 80 % of ball-bearing applications involve the use of grease to leverage its sealing properties and high maintainability etc. [1]. There exists great interest in the use of grease, as regards the design of rolling bearings, and several studies [2, 3] have been published concerning grease behavior inside rolling bearings. Grease configuration in rolling bearings undergoes transition from a period over which it is stirred under rotational motion to that in which lubrication is performed by either the base oil separated from grease deposited on the cage/seal or small quantities of grease itself[3].

The former is a high-torque, high-heat generation churning state, the latter is a low-torque, low-heat generation state in which “clearance” occurs in the layers of grease separated from the rolling surface; the latter state is considered as a preferable operating environment for bearings. Although the channeling state corresponds to a period of steady bearing torque, it is difficult for grease—pushed to the sides owing to churning motion—to return to the rolling surface. This might result in early termination of its operating life, because the leftover grease separated from the rolling surface does not provide effective lubrication. If this leftover grease can be made to efficiently contribute to lubrication, bearing life can be further extended over that presently realized. To this end, the proposed study aims at obtaining greater knowledge concerning development of an efficient bearing design methodology by gaining further insights into grease behavior within bearings.

Conventionally, visual observation of grease behavior from the outside of a bearing is extremely difficult owing to existence of a seal—attached to prevent leakage and dispersion—which become an obstacle. Observation of

---

[*] Corresponding author: noda-t@nsk.com

grease surface, therefore, can only be made possible by removal of the seal. For cases wherein observation of grease configuration is of primary importance, the above technique is considered inappropriate, since seal removal may also cause some of the grease adhering to contact surfaces to be removed. Besides disassembly inspection, methods involving flow investigation by use of colored or radioactive grease [4] as well as direct observation sans seal attachment [5] have been previously proposed. However, the former is limited to attainment of information concerning the grease volume moved while the latter only facilitates inspection of the surface shape of grease exposed to ambient air. There presently, therefore, exists no definitive method using which grease behavior can be visually inspected without disassembling bearings. To address this concern, authors, in this study, performed X-ray based non-destructive inspection to rolling bearings that requires no disassembly. Furthermore, 3D-CAE (Computer Aided Engineering) was performed to predict grease behavior along with investigation of its operating states inside rolling bearings.

2. X-ray observation of grease behavior

2.1 X-ray CT equipment and the test bearing

In this study, an X-Ray CT (Computed Tomography) which can capture tomographic images of subjects was utilized. Equipment comprised a micro-CT scanner (TOSCANER30 000 μhd; spatial resolution: 5 μm) developed by Toshiba IT Control Systems. When X-rays pass through non-homogenous substances, their intensity I undergoes decay in accordance with the following equation [6].

$$I = I_0 \exp(-\mu_i x_i) \qquad \text{............ (1)}$$

Here, I_0, μ_i and x_i denote incident X-ray intensity, linear absorption coefficient for material i, and emission distance, respectively. Value of the linear absorption coefficient depends on the type of material (i.e., atomic numbers of its constituent elements), its density, and incident X-ray intensity. Because exposing metallic surfaces to high-intensity X-rays causes generation of metal artifacts that render CT images blurry [7], appropriate X-ray control and contrivance of exposed surfaces were considered necessary. High-corrosion-resistance resin ball bearings (grade 6001) were adopted as a bearing structure in this study, since X-rays can easily pass through them and which can suppress the occurrence of metal artifacts. These bearings comprised inner and outer rings made of a special fluororesin carbon fiber composite. The cage was made of fluororesin, whereas rolling elements comprised special glass spheres. Such bearings are normally used under special operating environments and were not equipped with seals. In the present case, however, acrylic plates were fitted to the outer ring with the aim of preventing grease leakage during the experiment. X-ray imaging was performed by having filled 53% of the bearing volume with urea grease. The X-ray controller was set to 55 kV tube voltage, 260 μA tube current, 37 μm spatial resolution, and 60 μm slice thickness. As depicted on the left in Fig. 1, position of the bearing cross-section can be defined using R-Z cylindrical coordinate frame, its origin (marked as 0 in the figure) coinciding with the bearing center. Additionally, points on the right and left ends of the outer ring of the bearing have been marked as 1. The right of Fig. 1 depicts the X-ray CT image of the bearing captured immediately after filling it with grease at the location Z = 0.36. Based on observed shading differences, the inner and outer rings, cage, grease and air can be easily distinguished in the figure. Therefore, the configuration of this test specimen and X-ray controller can be considered as an appropriate set for observing grease behavior.

2.2 Transition of the lubricant state

The bearing described in the previous subsection was rotated by the inner ring under an axial load of 10 N (along the positive Z-direction) at 600 rpm, and X-ray CT images of the grease state were captured after of 1 and 5 minutes. Figure 2 depicts CT images captured at locations Z = 0.29, 0.36, 0.44 and 0.63 at the beginning of rotation and after the elapse of 1 minute. From the CT images after 1 minute, it can be seen that while grease separates from the inner and outer rings as well as rolling elements through the “clearance,” it adheres to the cage throughout the period of rotation. In particular, at Z = 0.44 and 0.63, it can be confirmed that the shape of grease form between rolling elements is similar for each. This confirms that there exist no differences in phenomena occurring between adjacent rolling elements. Therefore, treating the results observed by fixing the subject of measurement between one adjacent rolling elements as representative of the grease flow of the bearing in its entirety can be considered as no issue.

Figures 3 (a), (b), and (c) depict CT images captured at the start and after the elapse of 1 and 5 minutes of bearing rotation, respectively, with focus on cross-sectional positions corresponding to Z = 0.29, 0.36, and 0.63 (from left to right). Figures 3 (a) and (b) demonstrate existence of the churning phase accompanied by stirring, since the shape of grease changes dramatically. On the other hand, Fig. 3 (c) depicts grease to maintain a shape nearly similar to that in Fig. 3 (b). Thus, the time elapsed between the capturing of Figs. 3 (b) and (c) can be considered as the period over which grease transitions to the channeling state, demonstrating stable behavior. Moreover, it can be inferred from Figs. 3 (b) and (c) that the lack of change in grease shape is due to the absence of a mechanism to make separated grease return to the rolling surface.

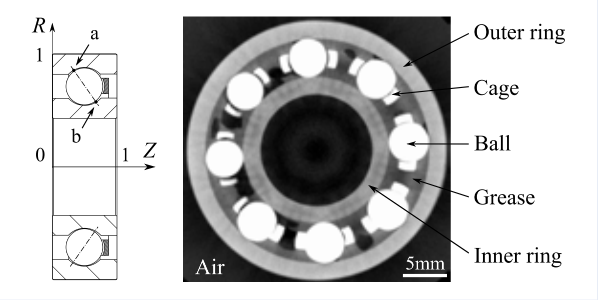

Fig. 1 Left: Definition of *R-Z* axis, right: X-ray CT image of the plastic bearing at the cross-section, Z = 0.36

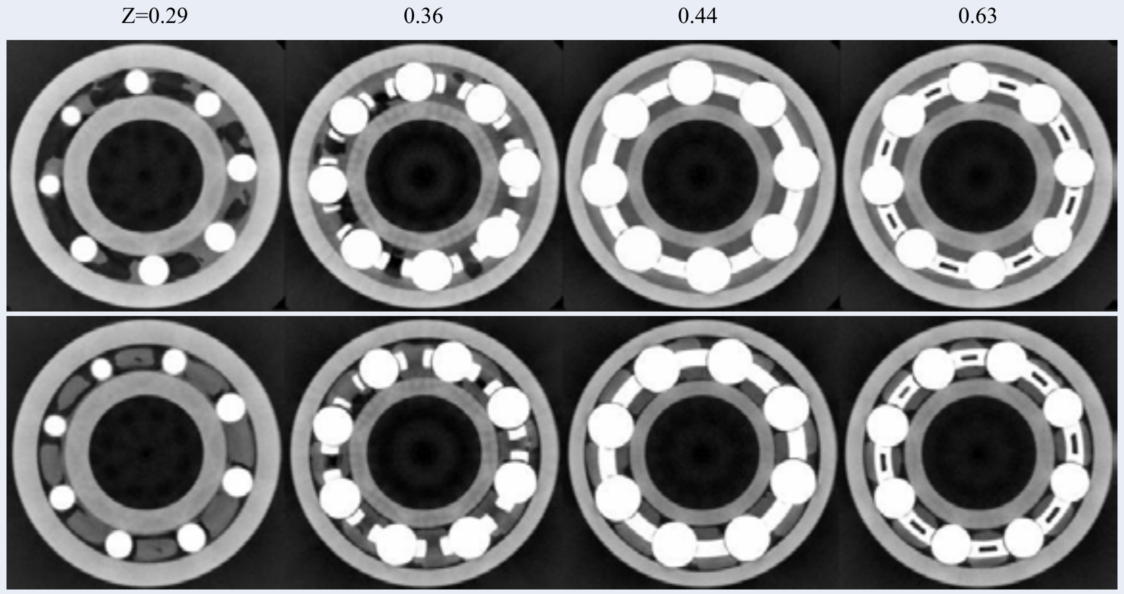

Fig. 2 X-ray CT images of the plastic ball bearing with urea grease at several slices (top: Initial grease distribution, bottom: grease distribution after approximately one-minute rotation)

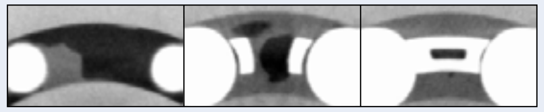

(a) Initial grease distribution

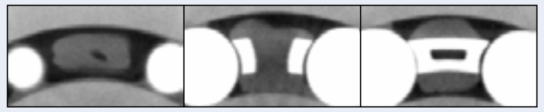

(b) Grease distribution after one-minute rotation

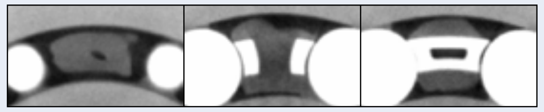

(c) Grease distribution after five-minute rotation

Fig. 3 Transition of grease lubrication from churning to channeling state observed from clipped CT images at three different times

2.3 X-ray absorption of grease

Defining grease behavior beyond the scale of phenomena around elastohydrodynamic lubrication regime as macroscopic flow, it can be classified as a mass grease movement with surface-layer deformation and its internal flow. The former can be described based on the shape of the surface interfacing with air, however, the latter is difficult to grasp without analysis of grease-flow streamlines over time. In order to observe flow states inside grease, X-ray CT imaging was conducted using urea-and barium-based greases with different X-ray-absorption rates. As when pouring milk into coffee, here the flow state within the grease is expected to appear in contrast in the CT image as a marble pattern. Table 1 lists the composition and properties of the two grease types. The left of Fig. 4 depicts CT images of the two greases placed side-by-side. Based on the difference in shading, the two grease types can be easily distinguished in CT images. Generally, the mass absorption coefficient of grease obtained by dividing the linear absorption coefficient by grease density demonstrates monotonic increase with atomic number [6]. Barium-based grease possesses Ba, which has a higher atomic number compared to C, H, N, and O that constitute the urea-based grease. Consequently, barium grease absorbs more X-rays compared to urea grease, and therefore, appears white in the CT image in Fig. 4. The right of Fig. 4 depicts a CT image captured immediately after filling of the plastic bearing with both barium and urea greases, and the results displaying the CT image spectrally across 256 gradations. The total grease volume inside the bearing comprised equal amounts of urea-and barium-based greases occupying roughly 40% of the bearing volume in combination. Imaging conditions were maintained identical to those already stated, with a tube voltage of 55 kV, tube current of 260 μA, spatial resolution of 36 μm and a slice thickness of 60 μm. Since subjects photographed

Table 1 Physical properties and composition of urea and barium greases

Lubricant	Thickener	Base Oil	Base Oil Kinetic Viscosity [mm^2/s] (40 degrees Celsius)	Density [g/cm^3]	Worked Penetration
Urea grease	Urea	POE	30.5	0.93	264
Barium grease	Barium Complex Soap	MO + Ester	23.0	0.99	280

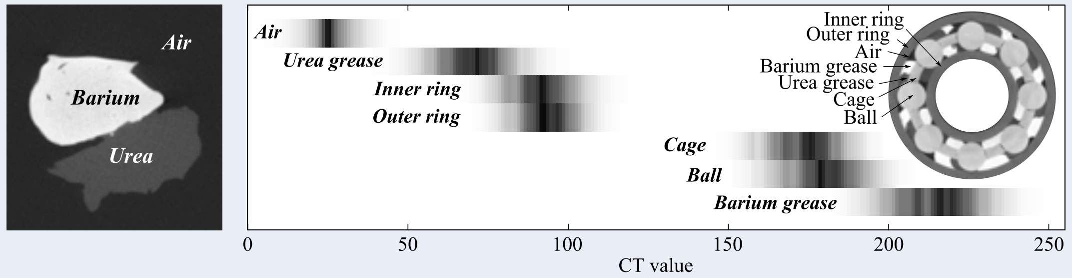

Fig. 4 Left: Grayscale comparison among urea, barium grease and air, right: 2D grayscale spectrum of the plastic bearing X-ray CT image including two different greases at one cross-section

in X-ray examinations as part of medical situation are fundamentally biological objects, medical diagnosis performed based on CT values [6] designates air and water with numbers–1 000 and 0, respectively. However, because in industrial applications subjects of imaging are not limited, no clear designations as above exist for industrial purpose. In this study, therefore, grayscale information obtained from CT images displayed at 256 gradations was termed as the CT value. From the spectrum on the right of Fig. 4, it can be realized that barium grease possesses the highest CT value in the specimen. The bearing used during experiments was identical to that depicted on the right of Fig. 1. However, relative changes are observed in the grayscale gradation of captured CT images owing to adding the higher CT value of barium grease. Because the areas in which materials with the highest X-ray absorption are defined as white, as a result other areas are wholly shifted toward black in appearance, based on their difference from the maximum CT value. The actual X-ray absorption properties of each material did not change.

(a) Initial grease distribution

(b) Grease distribution after one-minute rotation

(c) Grease distribution after five-minute rotation

Fig. 5 Grease internal flow observed from clipped CT images at three different times

2.4 Observation of internal flow

X-ray imaging was performed on the bearing shown previously under the same conditions as in Section 2.2. Figure 5 depicts CT images captured after of 1 and 5 minutes at locations given by $Z = 0.25$, 0.38, and 0.5. Detailed explanation of the experiment has been omitted here, since insights obtained concerning the surface shape of grease were identical to those described in Section 2.2. Instead, observations concerning the internal state of grease have been discussed in this section. As observed in Fig. 5 (b), the direction of bearing rotation on the raceway surface, as viewed from the cage, was clockwise and counterclockwise with respect to the inner and outer rings, respectively. The figure reveals that the inside of the grease is dragged along the raceway surface and as a whole deforms counterclockwise. This may be attributed to shear deformation occurring on the grease surface and subsequently transmitting to the inside of the bearing under the effect of molecular viscosity. Moreover, reference to Figs. 5 (b) and (c) reveals the presence of newly formed grease demonstrating an appearance between that of barium-and urea-based grease caused by mixing of the two types of grease. Value of the resulting linear absorption coefficient was considered equal to the average of values corresponding to those of urea-and barium-based greases during the stirring (churning) process. On the other hand, reference to the grease pattern formed demonstrates that since neither of the grease of the two types undergo any major change, no flow of the deposited grease occurs. In other words, the resulting grease behavior corresponds to that of deformation, and not flow, and that grease shape generated during churning remains fixed and maintained.

2.5 Analysis of the grease flow

Fig.6 depicts CT images for each point in time for $Z = 0.25$ as well as the relationship between the CT value (λ) of the constituent pixels and frequency. Although there exist differences between the initial and 1 minute plots, it can be seen that plots captured 1 minute and 5 minutes are almost the same. Figure 7 depicts the rate of change $\delta_{01}(\lambda)$, $\delta_{15}(\lambda)$ obtained by dividing the difference in frequency between the initial state and 1 minute and the difference between 1 minute and 5 minutes by the total frequency, for each λ with respect to each Z cross-section. Since CT-value frequencies of bearing's constituent materials are cancelled out when taking the difference between CT images, the only frequency value that remains includes air, barium-and urea-based greases, or a mixture of the two. Where there exists no flow and the CT image does not change, the CT value for each fluid is cancelled out in the same way. Based on Fig. 7, axial flow of the lubricant was analyzed by means of Eulerian method. Comparing entire images obtained for δ_{01} and δ_{15}, it can be understood that the observed change in δ_{01} is conspicuous across all cross sections, and that grease demonstrated active flow at the start of bearing rotation. Conversely, there exists no noticeable change in δ_{15}, indicating a gentle state of channeling. Focusing on each cross section of δ_{01}, the air ($\lambda \simeq 25$), urea grease ($\lambda \simeq 70$), and barium grease ($\lambda \simeq 220$) are decreasing at $Z = 0.25$, and it can be seen that the decrease increases centering around $\lambda \simeq 95$, 125 as mixed grease flows from the same or other cross sections. A similar tendency was observed at other cross sections; however, with regard to air, a positive trend was observed at $Z = 0.50$ and 0.63. This was thought to be a result of the transfer of initially filled grease to other cross sections under the influence of external factors, and its subsequent replacement by air. The reduction in air content at the same cross section demonstrates grease moving to the seal side at locations $Z = 0.25$, 0.38, and 0.75. Near locations corresponding to $Z = 0.25$ and 0.38, there exists a gap produced by the tab part of the snap cage. This is a location where grease separated from the raceway surface can easily accumulate. On the other hand, the location $Z = 0.75$ corresponds to the thinned side of the cage, and although mixed grease flows similarly, the rate of increase is small compared to that of the tab. Because the volume of grease transferred on the tab side and the thinned part of the cage, the direction of grease flow depends on cage shape. Especially in the snap-type cage employed in the bearing considered in this study, there exists a stable region on the tab compared to the thinned side wherein grease is readily deposited.

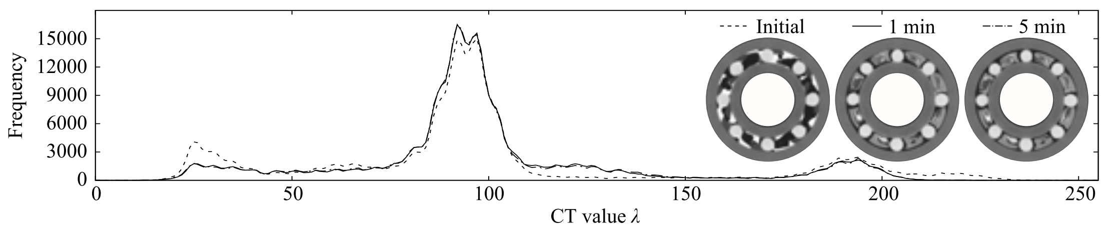

Fig. 6 Grayscale comparison of CT images of initial, after one and five-minute rotation of the plastic bearing at Z = 0.25

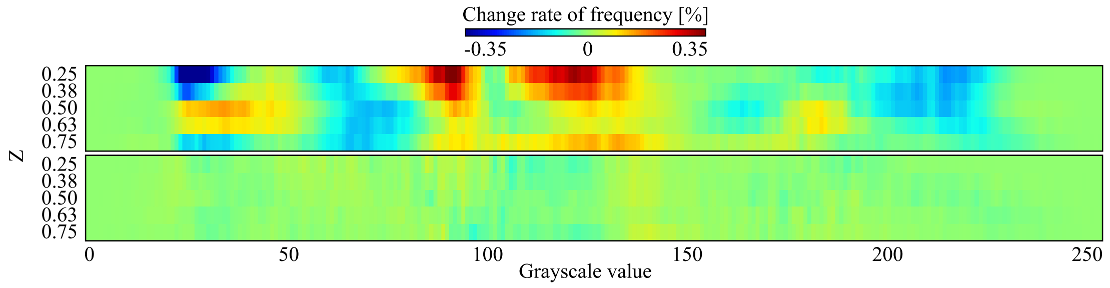

Fig. 7 Change rate of frequency of the plastic bearing X-ray CT images, top: grayscale change from initial to one minute (δ_{01}), bottom: grayscale change from one to five minutes (δ_{15})

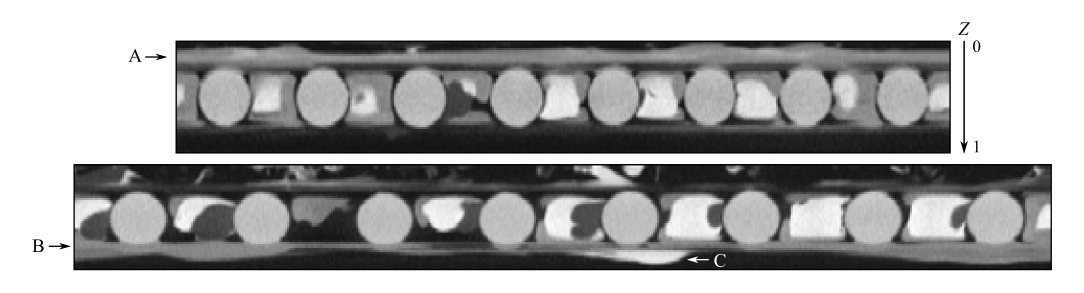

Fig. 8 X-ray CT images along the cylindrical cross-section, R = 0.62 (top: inner side), 0.84 (bottom: outer side)

2.6 Spatial non-uniformity of deposited grease

Figure 8 depicts CT images (after 5 minutes) of expanded cross sections around the Z-axis at locations R = 0.62 and 0.84. In both cases, bands of grease types A and B adhere to the surface around the rolling element, and in a part of the latter, in particular, it can be seen that unstirred barium grease, C, remains. Comparison of the different grease bands reveals that the band on the inner ring (A) is located upward on the page above the rolling elements, whereas that on the outer ring (B) is conversely located downward. Since an axial load is applied to the outer ring along the positive Z-axis, a void is created on the side opposite to the rolling element and the rolling element– groove contact point (Figs. 1 (a) and (b)). Because positions at which creation of the void occurs are different on the inner-and outer-ring sides, there exist corresponding differences between locations at which grease-band deposition occurs. It was understood that during the process which causes separation of grease from the raceway surface, grease tends to get transferred not to the side of the contact point with a narrow channel, but instead, to the side with availability of a wider space.

2.7 Shear phenomena between the greases

Figure 9 depicts CT images (from the top: at the start and at the elapse of 1 and 5 minutes after start of bearing rotation) at the location R = 0.62. As already described, only very slight change was observed in the state of grease between at the elapse of 1 and 5 minutes, and the surface shape of grease remains nearly constant. However, changes can be observed in the positional relationship between grease deposited on the cage (e.g. D1, D5) and grease-belt band (E1, E5) (Note the grease mass ▼ in the upper part of Fig. 9). The grease-belt band spanning the entire circumference adheres to the groove shoulder of the inner ring. Observed changes in the positional relationship between deposited grease and grease-belt band are caused by differences in the orbital speed of the cage and rotational speed of the inner ring. Furthermore, in some parts, grease bands were observed to come in contact with grease deposited on the cage and lateral surfaces of the rolling elements. Consequently, shearing occurs between grease deposited at locations D1, D5 and E1, E5, and this can be considered one of the sources of flow resistance. Moreover, due to its wettability, base oil bled from grease adhering to lateral surfaces of the rolling element was expected to flow across the surface and into the contact part. It was also thought that grease bands adhering to the groove shoulder become a reservoir for oil involved in oil-film formation.

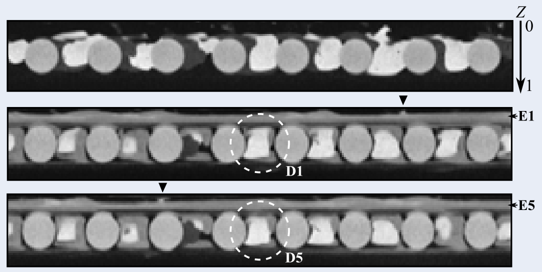

Fig. 9 X-ray CT images in a cylindrical cross-section, R = 0.62 (top: initial, middle: one-minute, bottom: five-minute rotation)

3. Numerical analysis of grease behavior

Grease is a semisolid substance mainly comprising a base oil and thickening agent. When subjected to shear forces, orientation of its molecular micelles changes and breakdown of its structure occurs and base oil retained within the thickener structure flows (microscopic flow) and functions as a lubricant. On the other hand, in the absence of shearing forces, grease demonstrates a solid-like behavior, thereby maintaining its shape and adhesion. Overall, grease is a complex fluid demonstrating characteristics of both solids and liquids along with rheological characteristics, such as shear-rate dependency, time dependence (thixotropy), and plasticity [8]. Perspectives of calculation cost, time dependency was not considered in this study and a homogenous substance demonstrating two types of rheological characteristics, shear-rate dependency and plasticity was assumed. Also microscopic physical and chemical phenomena, such as destruction and dispersal of the thickening agent as well as dyeing, bleeding, and oxidation of the base oil along with elastic-fluid lubrication on contact parts were not considered. Only macroscopic flow of grease and air was analyzed in this study.

3.1 Rheological equations

A mathematical model was first developed to simulate its flow characteristics to reproduce grease behavior. By subjecting grease to shear forces exceeding its yield value, the thickener structure breaks down and the state of grease changes from semisolid to liquid. A fluid that begins to flow due to shear between fluid layers when the shear stress exceeds its yield value is called a plastic fluid. Plastic fluids belong to non-Newtonian liquids, which has a nonlinear flow curve, and expressed in the following equation is called a Bingham fluid (ideal plasticity fluid).

$$\begin{cases} \tau_{\mathrm{ij}} = \tau_{\mathrm{y}} + \eta_{\mathrm{p}} \dot{\gamma}_{\mathrm{ij}} & for \ \left|\tau_{\mathrm{ij}}\right| > \tau_{\mathrm{y}} & \cdots\cdots\cdots\cdots (2) \\ \dot{\gamma}_{\mathrm{ij}} = 0 & for \ \left|\tau_{\mathrm{ij}}\right| \leq \tau_{\mathrm{y}} & \cdots\cdots\cdots\cdots (3) \end{cases}$$

Here, τ_{ij}, τ_y, η_p, and γ_{ij} correspond to the shear force, yield stress, plastic viscosity and shear rate, respectively. Plastic viscosity corresponds to the apparent viscosity of grease at point $\gamma_{ij} \to \infty$. Grease, in general, behaves similar to Bingham fluids. However, when estimating viscosity based on above equations, the observed deviation from experimental values becomes large in the low-speed range. In this study, therefore, the rheological equation was used in the following modified form proposed by Papanastasiou [9].

$$\tau_{\mathrm{ij}} = \left[\eta_{\mathrm{p}} + \frac{\tau_{\mathrm{y}}}{|\dot{\gamma}|} \left(1 - e^{-m|\dot{\gamma}|}\right) \right] \dot{\gamma}_{\mathrm{ij}} \qquad \cdots\cdots\cdots\cdots (4)$$

In equation (4), m is a constant with a time dimension called a stress growth exponent. Using m, a flow curve can be demonstrating rheological characteristics between Bingham and pseudo-plastic fluid. By appropriately setting values of τ_y, η_p, and m, a wide range of grease characteristics without stress-overshoot can be covered. Values of the yield stress, plastic viscosity, and stress growth exponent for urea-and barium-based greases are listed in Table 2, while Fig. 10 depicts a comparison between measured and calculated values of the apparent viscosity. Figure 10 reveals that calculated values well demonstrate the shear-rate dependency of grease.

3.2 Verification of method of analysis for non-newtonian fluids

Next verification of a method of non-Newtonian fluid analysis by applying Eq. (4) was conducted. The verification model was representative of a lid-driven cavity [10]. In a rectangular region (with coordinate origin set at the lower-left corner, x and y coordinates set along the horizontal and vertical directions, and comprising 50 × 50 grid points) with each side L = 1 m, the upper wall was moved at a velocity given by U = 1 m/s. Considering the fluid density to be given by ρ = 1 000 kg/ m^3 and plastic viscosity η = 10 Pas, static calculations were performed under the condition of Reynolds number Re = $\rho UL/\eta_p$ = 100. Figure 11 depicts flow velocity profiles obtained within the region. In the figure, Bn refers to a dimensionless quantity, called the Bingham number, defined as Bn = $L\tau_y/U\eta_p$. Since the results obtained for flow velocities u and v (the x component where the speed of x = 0.5 and the y component where y = 0.5 respectively) are nearly identical to those reported by Neofytou et al. [11], this method can be considered valid for analysis of non-Newtonian fluids.

Table 2 Rheological parameters of urea and barium greases

Grease	τ_y [Pa]	η_p [Pa·s]	m [s]
Urea	829	1.020	10
Barium	1314	0.276	10

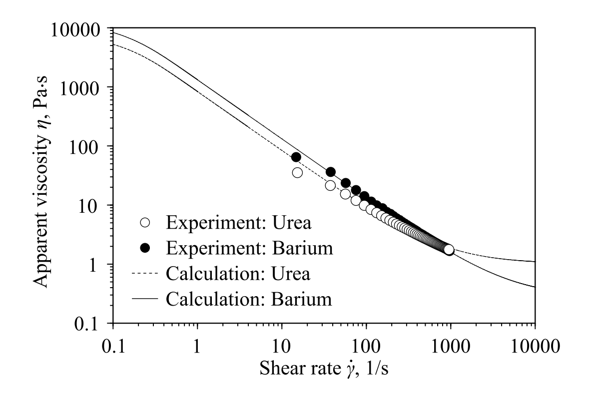

Fig. 10 Comparison the calculated apparent viscosity curve of two greases and experimental results

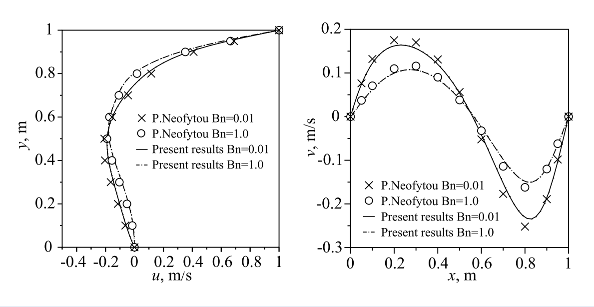

Fig. 11 Velocity u, v profile along the vertical and horizontal mid-plane at different Bingham number

3.3 Analysis of grease flow in ball bearings

The non-Newtonian fluid described above was taken to be grease, and its behavior within ball bearings was analyzed. The subject of analysis was a 6001 ball bearing, and the area of analysis comprised eight spaces obtained by dividing the closed flow path surrounded by the inner and outer rings, cage, rolling elements, and seal by the number of rolling elements. In order to create clearance close to the contact parts where it is difficult to generate the elements, a model ball with a diameter reduced by 3.4% was employed. Changes in clearance caused by the effects of rolling elements and inner/outer ring contact parts (the region of elastohydrodynamic lubrication) as well as axial loading and lubricant leakage were not considered. The analysis assumed lubrication to be performed under incompressible, unsteady, and isothermal laminar flow conditions. As a method of numerical analysis of flow including a free surface, the governing equation was discretized on an unstructured grid using the finite-volume approach with the VOF method (Volume of Fluid) which transfers the volume ratio and captures the shape of the interface. Operating conditions corresponded to an inner-ring rotational speed of 600 rpm. With regard to the lubricant, flow characteristics of urea-and barium-based greases described in Table 2 were given respectively. The quantities of both greases were added to the bearing to occupy approximately 40% of the available volume. Results obtained from unsteady calculations have been discussed in subsequent passages. Simultaneous to the beginning of the analysis, the grease was dragged across the sliding surface, and thereafter a churning period continued in which it was stirred while entangled. Within approximately 10 seconds of rotation, the "clearance" opened up between the sliding surface and grease, and its behavior shifted to a stable channeling state. No flow of grease deposited on the cage was confirmed at that period. Overall results reproduced by the above numerical analyses were qualitatively similar to those of the X-ray testing. Figure 12 depicts the results after the stabilization of behavior and X-ray CT images. The results of analysis are displayed with air in white, and grease in colored contours. Comparing results at each cross section, it can be seen that the surface shape and state of grease deformation demonstrate good agreement between experimental and calculated results.

3.4 Formation of a base-oil reservoir

In Fig. 13, parts (a) and (b) on the left depict CT images of rolling-element midsections at the radial location R = 0.73, whereas analytically obtained images on the right show depicts grease and viscosity distributions. It can be confirmed from Fig. 13 (a) that mound-shaped deposited grease F adhered to the inner-ring groove shoulder. The light-gray appearance of deposited grease indicates thorough mixing of the white-colored barium-and dark-colored urea-based greases. This result is consistent with the popular theory that the grease separated from rolling surfaces accumulates in the groove shoulder during the stirring process. Although the similar can also be said for the gray grease G deposited on the cage, since no change can be found in the barium-based grease H adhering to the cage from the beginning of bearing rotation. Thus, it was understood that effects of stirring did not extend within the grease. Figure 13 (b) depicts a part of the bearing cross-section in the vicinity of the tab portion of the cage. It can be seen that deposited grease I covers over grease J which is present from the beginning, to form a lid. Since there occurs no change in the shape of existing grease J before and after rotation, it is difficult for grease located within the tab part to directly provide lubrication. Therefore, this grease can be considered to function as a base-oil reservoir unless acted upon by any external factor. On the other hand, it was observed during analysis that stirred greases F', G', and I' are deposited on the inner-ring shoulder groove and cage. The deposited grease separated by air from the rolling surface and a thin film of grease adhering to it can be considered to have transitioned to a stable flowing state. In addition, no remarkable flow was confirmed within the grease, and the appearance of a maintained fixed shape as a solid-like state was reproduced. The right of Fig. 13 depicts viscosity distribution of fluids (grease–air mixture) in contact with the inner ring and cage surfaces. This figure demonstrates that viscosities of the inner-ring shoulder groove and cage snap section surfaces exceed that of the raceway surface. Therefore, the reason why it is difficult for grease to return to the rolling surface once separated is that the fluid adheres to surfaces while maintaining a high viscosity.

3.5 Relubrication

A possible lubricant function performed by the grease deposited in a stable position besides as a base oil reservoir is that of self-relubrication. In cases where bearings are subjected to sudden acceleration or deceleration or are required to operate in high-impact environments, external forces are expected to act on grease tend to knock it off from its deposited position. Figure 14 depicts CT images (left) captured for grease deposited on the cage along with corresponding analytical results (depicted on the right). As described above, no changes in grease behavior are observed during its separation from sliding parts by air. However, as depicted in Fig. 14 (b), when partially dispersed grease K adheres to deposited grease, the deposited grease accumulates causing narrowing of the "clearance," which in turn, results in a high probability of contact with the raceway surface. Soon growth and excitation (although unconsidered in this study) repeat, and therefore, lubrication occurs through contact with the raceway surface, as depicted in Fig. 14 (c). This can be thought to be one of the relubrication processes occurring in grease macroscopic flow.

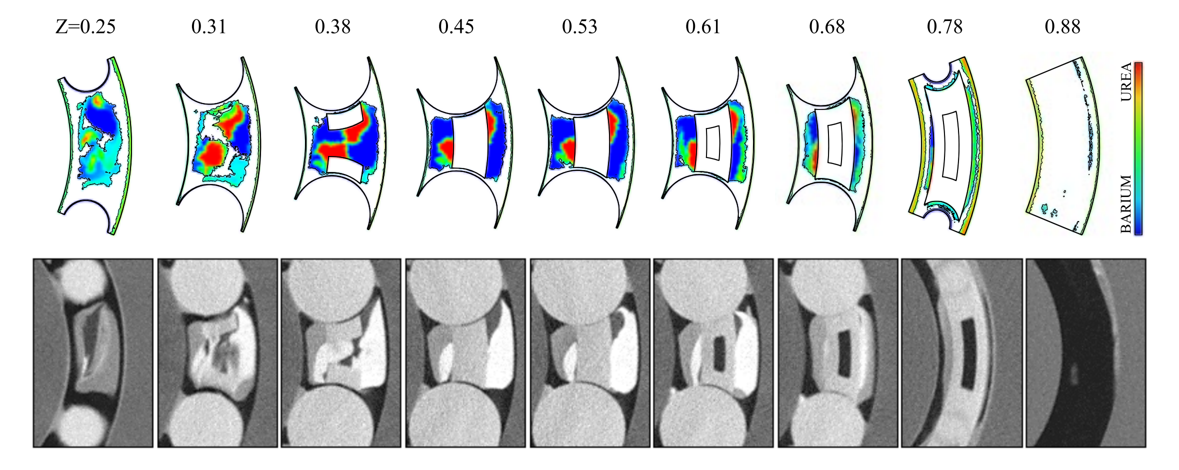

Fig. 12 Comparison calculated unsteady grease behavior and experimentally captured X-ray CT images of urea and barium greases in the plastic bearing at several axial slices

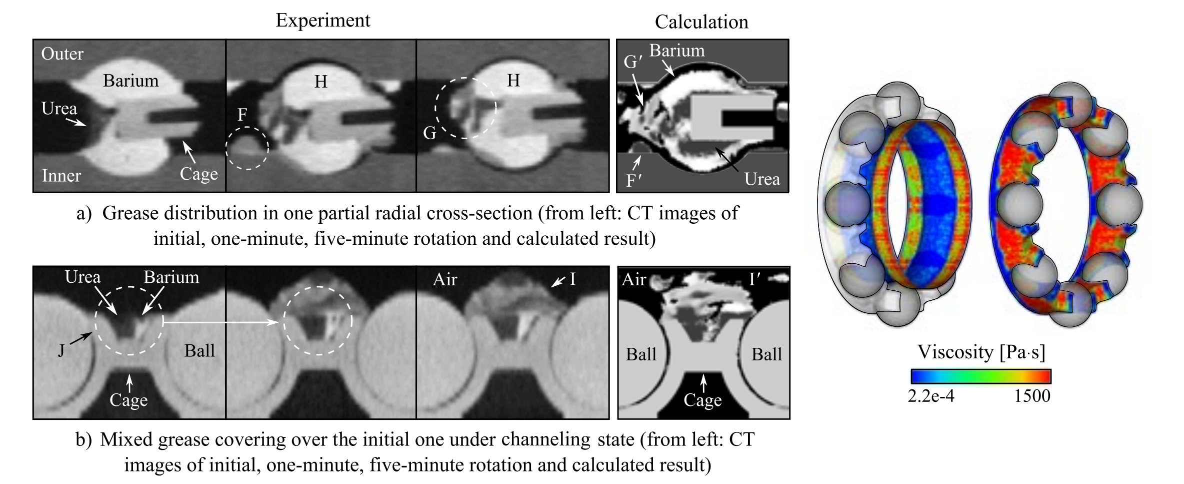

a) Grease distribution in one partial radial cross-section (from left: CT images of initial, one-minute, five-minute rotation and calculated result)

b) Mixed grease covering over the initial one under channeling state (from left: CT images of initial, one-minute, five-minute rotation and calculated result)

Fig. 13 Experimentally captured grease reservoir formation and calculated grease distribution

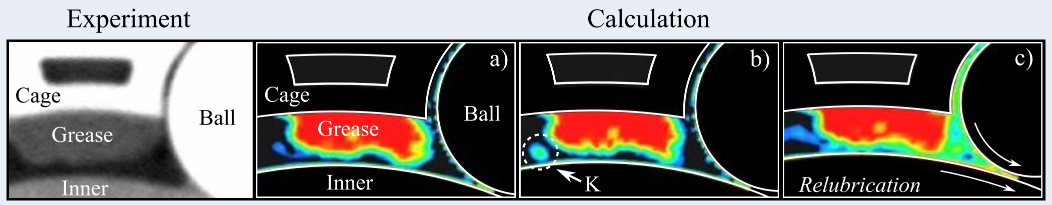

Fig. 14 X-ray CT image and calculated transient grease flows for indicating one of the grease relubrication processes

4. Conclusions

X-ray CT imaging and numerical analysis were performed on a plastic bearing with two kinds of grease. Key findings of and conclusions drawn from this study have been summarized below.

(1) By selecting appropriate materials with due consideration of their X-ray absorption properties, the shape of grease inside rotating bearings can be imaged using X-ray CT. In so doing, the distribution of grease during its churning and channeling states can be clearly visualized.

(2) Utilizing the differences between X-ray absorption characteristics of different grease types, flow states

inside grease were contrast radiographed within CT images. As observed, grease deposited in the channeling state demonstrated solid behavior without internal flow.

(3) Analysis of variations observed in CT images and values demonstrated that grease tends to accumulate in the open space within the tab part of the cage as well as on the side opposite to the contact point.

(4) By performing CFD (Computational Fluid Dynamics) simulations incorporating a rheological equation for grease, transient phenomena between the churning and channeling states of grease was numerically reproduced. Validity of the analysis technique was confirmed via comparison of results obtained against grease behavior investigated by capturing CT images. Reservoir formation and relubrication phenomena have also been qualitatively discussed.

It is to be noted that all findings reported in this paper are based on conditions corresponding to a limited rotational speed of 600 rpm. Since the d_n value (product of the rolling element pitch-circle diameter d_m and rotation number n), which represents the speed scale [3] for bearing rotation equaled 12,000, corresponding to extremely low-speed conditions (below 12,000 and less than 40,000) grease demonstrated such a behavior wherein gentle changes, mainly on the surface, were dominant. It is expected that different grease distributions would be obtained under high-speed conditions that cause vigorous stirring of the fluid such that the original shape would not be retained. This is a topic for the future.

Based on the discussion presented in Section 3.5, it can be considered necessary to develop a bearing-design methodology that enhances the probability of accumulated grease to come in contact with the raceway surface, thereby providing efficient lubrication and extending bearing life. That is to say, it is necessary to design the space in which fluid moves (mainly depending on the shape of the cage), develop grease that breaks up appropriately and can be easily dispersed, and comprehensive design of lubrication systems must be undertaken to incorporate the selection of grease that conforms to usage conditions.

References

1) Naka, M., “Grease Lubrication of Rolling Bearings at High Temperatures and High Speeds,” Lubrication, 32, 3, 1987, 165–170 (in Japanese).
2) Hoshino, M., “Flow Properties of Lubricating Greases and Torque in Rolling Bearings (Part 1),” Lubrication, 25, 8, 1980, 547–554 (in Japanese).
3) Lugt, P. M., “Grease Lubrication in Rolling Bearings,” John Wiley & Sons, Ltd., 2013, 6, 7, 149.
4) Shonozaki, T., Shigematsu, H. and Urai, T., “A Study on the Behaviors of Greases in the Ball Bearing,” Lubrication, 8, 4, 1963, 237–242 (in Japanese).
5) Lugt, P. M., Velickov, S. and Tripp, J. H., “On the Chaotic Behavior of Grease Lubrication in Rolling Bearings,” Tribology Transactions, 52, 5, 2009, 581–590.
6) “New Non-Destructive Inspection Handbook,” The Japanese Society for Non-Destructive Inspection, 1992, 55, 205, 819 (in Japanese).
7) Boas, F. E., “CT Artifacts: Causes and Reduction Techniques,” Imaging Med., 4, 2, 2012, 229–240.
8) Hoshino, M., “Theory of Grease Lubrication,” Tribologists, 47, 1, 2002, 8 (in Japanese).
9) Papanastasiou, T. C., “Flows of Materials with Yield,” Journal of Rheology, 31, 5, 1987, 385–404.
10) Fujita, M. and Ushijima, S., “Numerical Method to Predict Bingham Plastic Fluids Affected by Solid Particles,” Proceedings of the 19th Symposium on Computational Fluid Dynamics, B5–1, 2005, 1–5 (in Japanese).
11) Neofytou, P., “A 3rd Order Upwind Finite Volume Method for Generalised Newtonian Fluid Flows,” Advances in Engineering Software, 36, 10, 2005, 664–680.


Takashi Noda


Kenichi Shibasaki


Shinji Miyata


Masato Taniguchi

Rolling Bearing Diagnosis Based on Deep Learning Enhanced by Various Dataset Training

Osamu Yoshimatsu, Yoshihiro Satou, and Kenichi Shibasaki
NSK Ltd.

Abstract

In recent years, there has been an increasing interest in deep learning techniques for bearing flaking diagnosis, as it is possible to select vibration features and set diagnostic thresholds without domain knowledge of bearing diagnosis. The authors have previously proposed the CNN-LSTM model trained by using various datasets, which would be better generalization performance than that in studies ever reported, i.e., the model might be available for actual rotating machinery, in which the vibration feature is affected by the type of bearings, various operating conditions, and unknown disturbance. In this study, the model was analyzed by Grad-CAM, which was known as a visualization tool for a deep learning model for image data, to know how the model detects the flaking. The analysis of Grad-CAM has shown that periodic impulsive waveforms were detected when the test signals derived were of fault bearings as well as the expertized engineer will do. Furthermore, it has been proven that the extracted feature is still available even though the waveforms were contaminated with white noise. In addition, the analysis revealed the over-fitting situation of the trained model. Therefore, it was concluded that Grad-CAM analysis was capable of evaluating the trained deep learning models of bearing vibration diagnosis.

Keywords

Rolling bearing, diagnosis, deep learning, generalization performance, Grad-CAM

This article is reprinted from Yoshimatsu et al., “Rolling Bearing Diagnosis Based on Deep Learning Enhanced by Various Dataset Training,” *Hyouka Shindan Ni Kansuru Sinpojiumu Kouenronbunshu*, Vol. 2018.17, 2018 (Japanese).

1. Introduction

The condition monitoring of the rotating machinery used in many industrial fields is important for reducing operating costs and avoiding unexpected accidents. Above all, flaking damage in rolling bearings is a typical diagnostic target. In the diagnosis of flaking, a method using the measured vibration signal is generally used1). However, for high accuracy diagnosis, damage data must be accumulated, features must be selected, and diagnostic thresholds must be set for each unit of equipment to be diagnosed. In general, the availability of the data at the time of damage is low; therefore, it is difficult to expect a highly accurate diagnosis during a long period until the data at the time of damage of the equipment to be diagnosed is sufficiently accumulated. Therefore, a technique for diagnosing the bearing vibration characteristics at the time of flaking with high accuracy is desired even for mechanical equipment without sufficient damage data.

On the other hand, it is known that deep learning can automatically extract useful feature quantities from input data by using classification models trained with large amounts of data in tasks such as image classification2). In light of this fact, it is possible to construct a model to extract versatile features common to various data by using the vibration data of different types of bearings with flaking for training the deep learning model and to expect a generalization performance (effective for unknown data) that is effective even for unknown bearing diagnosis.

However, in recent years, reports on bearing diagnosis using deep learning rarely discuss the features extracted by the diagnostic model and the generalization performance of the model. Therefore, the authors constructed and used a dataset containing various flaking vibration acceleration data to construct a bearing flaking diagnostic model with high generalization performance, and evaluated the generalization performance of the diagnostic model trained by deep learning3). As a result, the generalization performance of the diagnostic model was improved by diversifying the measurement environment of the training data. However, since it is difficult to understand the process of the deep learning models, consideration of the factors that improved the generalization performance has been insufficient.

In this study, to examine the factor of generalization performance improvement for deep learning diagnostic models when the diversity of training data is increased, we verified the existence of periodic impact vibration detection, which is a versatile feature of flaking vibration, using a method to visualize the diagnostic process of deep learning.

2. Improvement of the Generalization Performance of Diagnostic Models through Deep Learning[3]

In order to improve the generalization performance of bearing diagnostic models through deep learning, the authors prepared the training data and test data using three vibration acceleration datasets with different measurement environments, then conducted training as well as tests of the diagnostic model. As a result, it was confirmed that the generalization performance improves with a diagnostic model trained using various data, including normal vibration acceleration data measured in a diagnosis target environment. This chapter gives an overview of the investigation.

2.1 Details of a deep learning diagnostic model

In this research, a model combining a CNN (convolutional neural network) and LSTM (long short-term memory) is applied as a target for the visualization of the diagnosis process. CNN is one type of deep learning that is mainly applied to image processing, and local features of image data are extracted by repeating the processing in the convolutional layer as well as the pooling layer[4]. LSTM is another type of deep learning, and it is mainly applied to time series data processing and natural language processing. Also, it can perform classification and regression in consideration of a context of the data[5].

Figure 1 shows a diagram of the model applied in this research. This model is a two-class classification (normal/damaged) model consisting of nine CNN layers, one LSTM layer, and one fully connected layer. The aim of the model is to extract general features of vibrations during flaking. When bearing flaking occurs, impact vibration occurs when a bearing component, such as a rolling element, passes through a flaking part. The interval of these impacts is determined by the location where the flaking occurs and the number of rotations of the shaft, usually occurring at regular intervals. CNN aimed at extracting impact vibration, and LSTM aimed to determine the presence or absence of periodicity.

2.2 Data set

Table 1 shows the details of the three datasets (A, B, and C) used for training and testing. Each dataset is composed of the measurement data of a vibration acceleration sensor installed in a different test rig. Bearing numbers, operating conditions, measurement conditions, sizes and positions of artificial defects machined on the bearings are also different; therefore, various vibration acceleration data is included.

Dataset A was constructed using bearing vibration data[6] published by Case Western Reserve University, and 12 types of ball bearings with artificial defects and normal ball bearings were used under four loading conditions.

Dataset B was constructed with vibration acceleration data when cylindrical roller bearings in which four types of artificial defects were applied and normal bearings were operated under nine types of operating conditions. Dataset C was composed of vibration acceleration data when a spherical roller bearing with five types of artificial defects and normal bearings were operated under 24 types of operating conditions. All tests on datasets B and C were conducted by the authors.

Each dataset has been composed of a large amount of vibration acceleration data. Each frame contains 8 192 points of vibration acceleration data and is normalized (average value = 0, standard deviation = 1). Figure 2 shows examples of the vibration acceleration waveform after the normalization of each dataset. It was confirmed that the periodic impact vibration was included in the vibration acceleration data at the time of flaking.

2.3 Training and evaluation methods

Training and testing of diagnostic models were performed using the three datasets. The training data consists of 5 000 frames of vibration acceleration waveform, and the ratio between normal and flaking is 1:1.

When mixing the vibration acceleration waveforms of multiple datasets, the ratio of the number of vibration acceleration waveforms for each dataset was made equal. On the other hand, every test data is composed of 2 000 frames of vibration acceleration waveform, and there is no overlap with the training data. All training of the diagnostic model was completed at the stage of 10 epochs.

One epoch represented one training cycle using 5 000 frames of waveform data. In addition, since the initial value of the weight coefficient used for the calculation in each layer of the diagnostic model and the arrangement of the training data was determined at random, the training results were not stable. Therefore, each training session and test was performed 100 times, and the evaluation was made on the basis of the average value of the test results.

The F-score was used as the evaluation index. The calculated F-score is in a range from 0 to 1.0, and the closer to 1.0, the higher the diagnostic accuracy. The F-score of the diagnostic model that failed to learn, so that all diagnostic results would be output identically, is 0.33 in this investigation[3]. Furthermore, assuming equipment diagnosis in an actual field, additional evaluations were performed using each trained diagnostic model in a state where noise was mixed in all test data.

All the datasets used for the learning this time were measured with a test machine in a clean environment; however, it is predicted that disturbance vibrations will occur due to various factors with actual field machinery and equipment. Therefore, Gaussian noise was added to the normalized vibration acceleration waveform of all test data. The standard deviation σ of Gaussian noise was in five types, 0.1, 0.2, 0.5, 1.0, and 2.0, and the average value was set to 0 in each case. Gaussian noise was generated by the numerical calculation library Numpy 1.14.2 and Python 3.5.4.

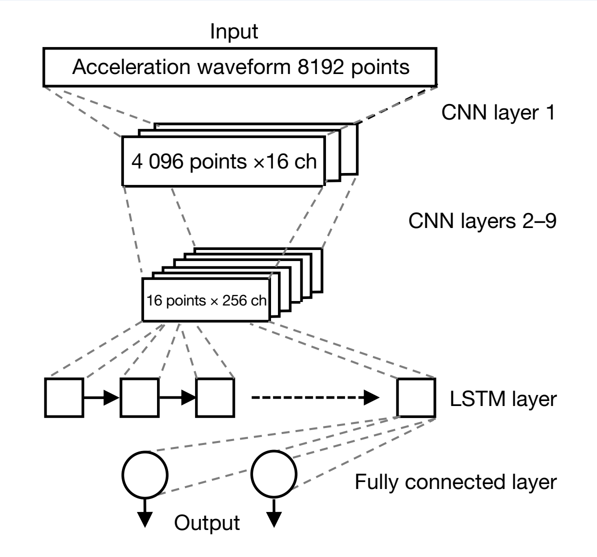

Fig. 1 Diagram of the applied CNN-LSTM model[3]

Table 1 Details of the Datasets[3]

Dataset name	A(CWRU data)		B		C	
Bearing type	Ball bearing		Cylindrical roller bearing		Spherical roller bearing	
Bearing number	6205-2RS JEM (SKF/NTN)		NU2228BMMA (NSK)		230/750CAME4 (NSK)	
Sampling rate [Hz]	48 000		48 000		800	
Rotational speed [min^{-1}]	1 730 to 1 797 (4 speeds)		1 200 to 1 750 (3 speeds)		8 to 20 (4 speeds)	
Load conditions	4 (Motor horse power)		3 (Radial)		6 (Radial + Axial)	
Types of artificial defect	Fault	Sizes	Fault	Sizes	Fault	Sizes
	None	1	None	1	None	1
	Inner race	4	Inner race	3	Inner race	1
	Outer race	4	Outer race	1	Outer race	4
	Ball	4				

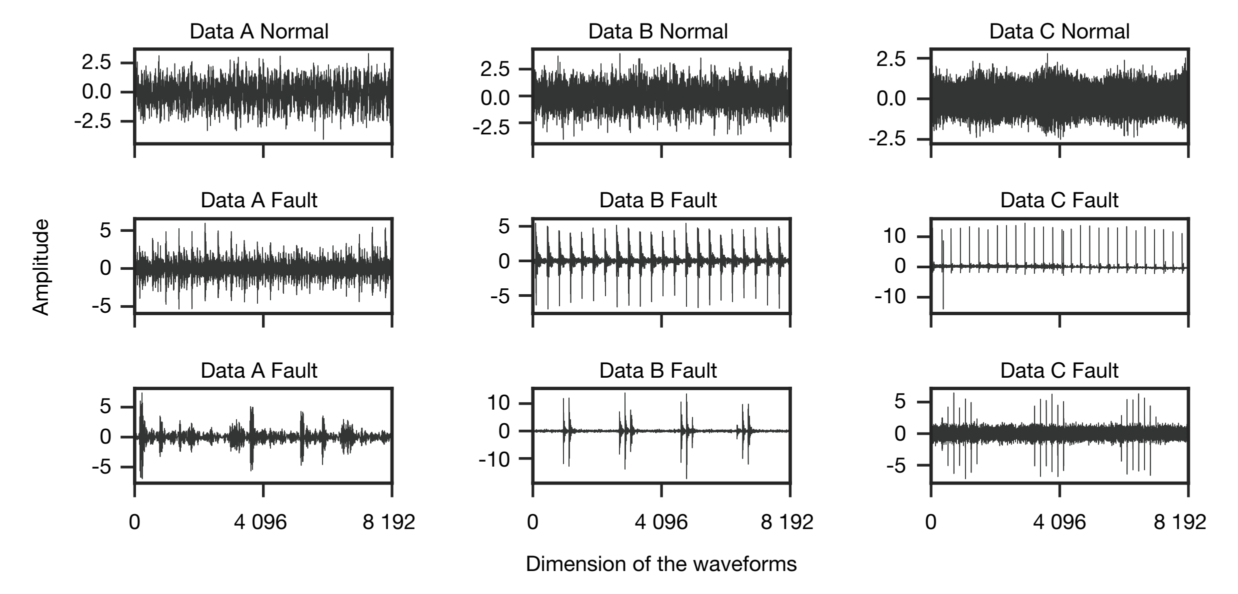

Fig. 2 Examples of normalized acceleration waveforms of Data A, B, and C[3]

2.4 Overview of evaluation results

The deep learning diagnostic model that uses bearing vibration acceleration data measured in various environments for training shows higher generalization performance than the diagnostic model trained with data in a single environment. Furthermore, the effect on the diagnostic accuracy when noise was mixed in the data was low. The tendency of the generalization performance of the deep learning diagnosis model will be described using representative evaluation results.

Figure 3 shows the diagnostic accuracy of the diagnostic model trained with various combinations of the test data in dataset B. Bn in the figure represents only the vibration acceleration data of dataset B in the normal state. Among the diagnostic models in the figure, the F-score of the diagnostic model trained with the dataset A + C + Bn was significantly higher compared to the models trained with other data.

As described above, the diagnostic model trained with data acquired under various conditions tends to improve generalization performance when compared to a case where the diagnostic model is trained with only data acquired in a single environment. Figure 4 shows the evaluation results of a diagnostic model trained with various combinations of data when noise was added to the test data of dataset C. Cn in the figure represents only the vibration acceleration data of dataset C at a normal time. With any diagnostic model, when the noise σ is 1.0 or more, the F-score decreases significantly. However, in the diagnostic model trained with the data of dataset A + B + Cn, the decrease of the F-score was lower compared to the diagnostic models trained using other data.

As described above, the diagnostic model trained with data acquired under various conditions tends to be less susceptible to noise as compared to the case where training was performed only with data acquired in a single environment.

3. Visualization of Diagnostic Model Processing

3.1 Visualization method of the diagnostic process

Grad-CAM was applied to a trained diagnostic model in order to confirm whether the presence or absence of periodic impact vibration in the input data contributed to the diagnostic results in the Grad-CAM bearing flaking diagnostic model. Grad-CAM is a method[7] for visualizing regions in input data that have strongly contributed to output results in a deep learning model and is used for the purpose of checking the classification grounds of an image classification model.

$$\alpha_k^c = \frac{1}{Z}\sum_{i=1}^{Z}\frac{\partial y^c}{\partial A_i^k} \qquad \text{............ (1)}$$

$$L_{Grad\text{-}CAM}^c = \sum_k \alpha_k^c A^k \qquad \text{............ (2)}$$

Equations (1) and (2) show the calculation formulas applied to the model in this report. In equation (1), the score y^c of the output class c at the time of inputting the vibration acceleration data is differentiated by the i-th output data A_i^k of the k-th channel in a specific layer, and the gradient $\partial y^c / \partial A_i^k$ of the differentiation result is averaged over all Z output points to obtain the weighted coefficient α_k^c of the k-th channel. In equation (2), the weighted sum of the output result A^k for the k-th channel is calculated as $L_{\text{Grad-CAM}}^c$ using the weighted coefficient α_k^c obtained in equation (1).

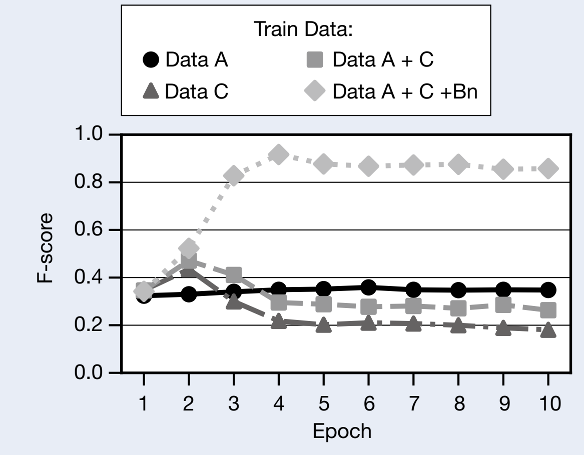

Fig. 3 Test results of the model for dataset B and trained without fault data of dataset B[3)]

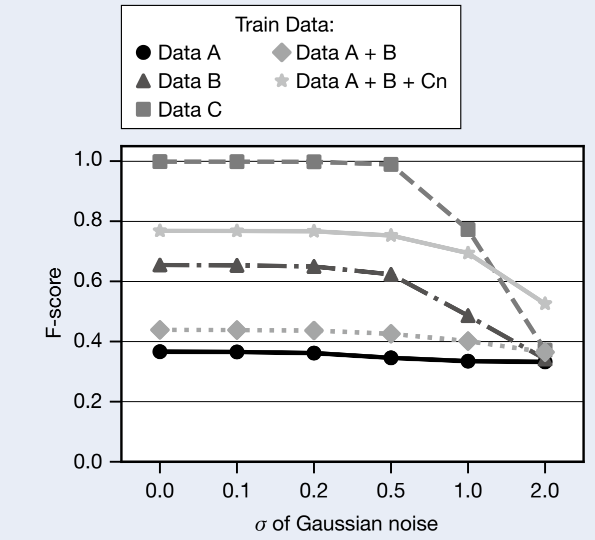

Fig. 4 Test results of the model for dataset C with noise component[3)]

In this investigation, Grad-CAM was applied to the output of the ninth CNN layer in the diagnostic model. The Grad-CAM results in this layer are the values of 16 points corresponding to 8 192 points of input data, and the input data corresponding to the position where this value is large is an important region that strongly contributes to the diagnosis results. Also, the input data corresponding to the location where the value is low means that the area strongly contributes to the output of the other class. In this report, Grad-CAM results were normalized to verify only the performance of detecting periodic impact vibration.

3.2 Visualization results of important region of input data by Grad-CAM

Representative examples of Grad-CAM results for specific diagnostic models in Figures 3 and 4 are shown in Figures 5 through 14. The upper part of each figure shows the vibration acceleration waveform input to the diagnostic model, and the lower part shows the important region, which is the Grad-CAM results, by 16 points from a to p.

Focusing on the model that showed high generalization performance in the evaluation of Figure 3, in order to confirm the features extracted by the high generalization performance model, Figures 5 and 6 show the results of applying Grad-CAM to the specific diagnostic model, trained with the data A + C + Bn and achieving an accuracy of 0.9 or higher for the F value.

Figure 5 also shows the results when the vibration acceleration data in a normal state is input, and the position p behind the input data is the important region. On the other hand, in Figure 6 the important region at the time of inputting the vibration acceleration data at the time of flaking is at the b, f, j, and m positions, which indicates that it is a periodic position corresponding to the impact vibration. As a result, it was confirmed that the applied diagnostic model extracted periodic impact vibration common to the vibration acceleration signals at flaking as a feature and that reasonable diagnosis similar to the conventional determination methods was performed.

Also, in the evaluation of Figure 4, noting that even

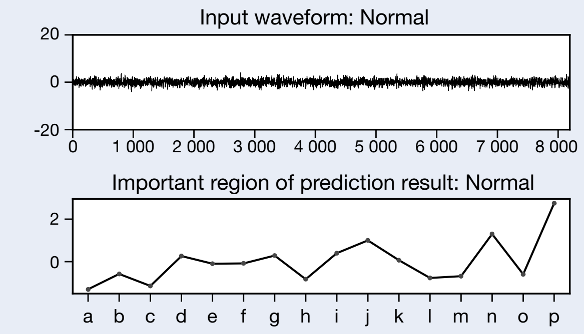

Fig. 5 Example of Grad-CAM result applied to high generalization performance model with normal waveform input

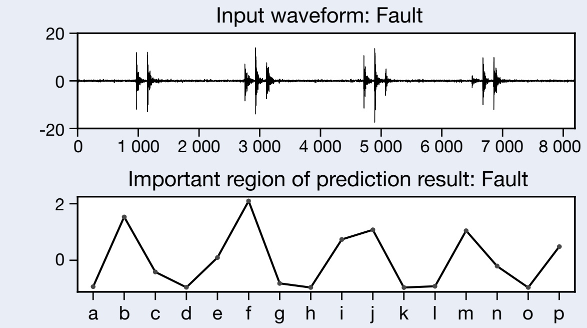

Fig. 6 Example of Grad-CAM result applied to high generalization performance model with fault waveform input

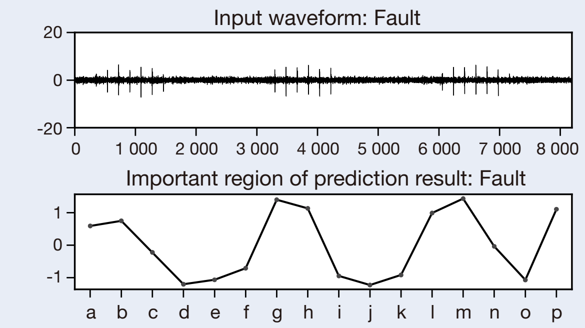

Fig. 7 Example of Grad-CAM result applied to high noise robustness model with fault waveform input added no noise

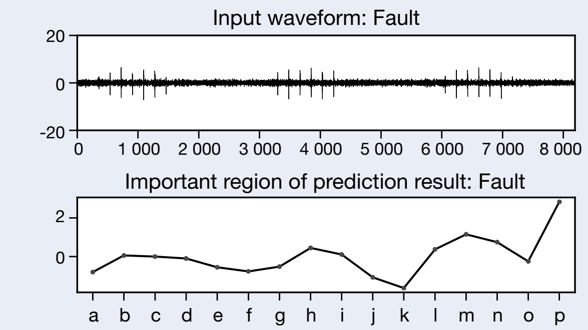

Fig. 8 Example of Grad-CAM result applied to low noise robustness model with fault waveform input added no noise

if the standard deviation σ of the Gaussian noise added to the input data increases, the F-score of the diagnostic model trained with the data A + C + Bn was difficult to decrease, and factors responsible for the noise robustness of the diagnostic model were considered.

The Grad-CAM results of the diagnostic model trained with data A + C + Bn are shown in Figures 7, 9, and 11, and the Grad-CAM results of the specific diagnostic model trained with data C only are shown in Figures 8, 10, and 12. In each case, Gaussian noise with σ increased to 0, 0.5, and 2.0 is input to the same data.

In Figures 7, 9, and 11, the values near positions b, g, and m corresponding to the impact vibration, were high even when σ increased, whereas in Figures 8, 10, and 12, when σ increased, the values near the positions c, h, and m corresponding to the impact vibration were low, and the position p irrelevant to the impact vibration was the important region. From these results, it was confirmed that in the diagnostic model with high noise robustness, periodic impact vibrations in the input data could be extracted even when noise was mixed in the data. Furthermore, focusing on the fact that the F-score decreased as the training after Epoch 5 progressed in the diagnostic model trained with the data A + C + Bn in Figure 3, in order to verify the cause, Grad-CAM was applied to the same diagnostic model at the Epoch 4 and Epoch 10 time points.

Figures 13 and 14 show the results when the same data was input to each model. While the positions c, g, k, and n corresponding to impact vibration are important regions at the time of Epoch 4 in Figure 13, at the time of Epoch 10 in Figure 14, the values of Grad-CAM results at positions d, g, k, and n differ greatly depending on impact vibration, indicating that misdiagnosis can occur. As a result, a phenomenon called “over fitting,” in which the extracted feature quantity is too specialized for the training data and the generalization performance of the model is reduced, has been confirmed.

In order to construct a diagnostic model with high generalization performance, it is necessary to confirm whether general-purpose features have been extracted by confirming the training status using a method such as Grad-CAM.

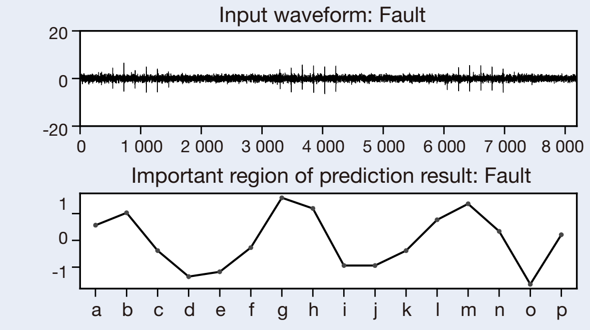

Fig. 9 Example of Grad-CAM result applied to high noise robustness model with fault waveform input added σ = 0.5 noise

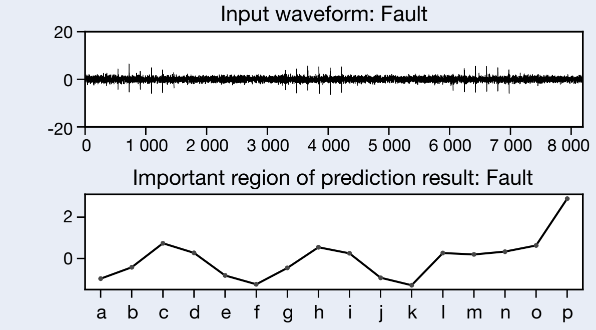

Fig. 10 Example of Grad-CAM result applied to low noise robustness model with fault waveform input added σ = 0.5 noise

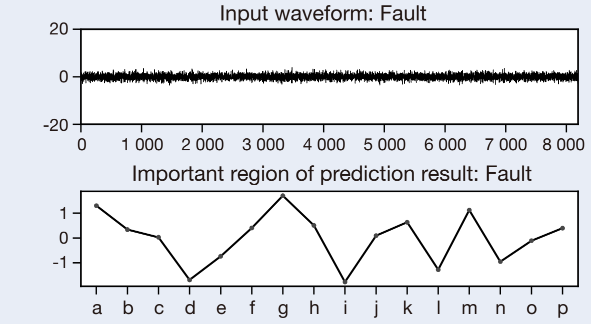

Fig. 11 Example of Grad-CAM result applied to high noise robustness model with fault waveform input added σ = 2.0 noise

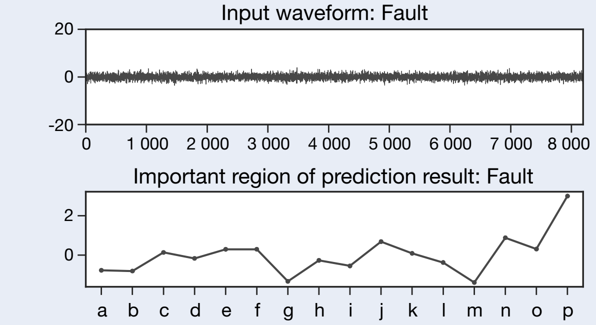

Fig. 12 Example of Grad-CAM result applied to low noise robustness model with fault waveform input added σ = 2.0 noise

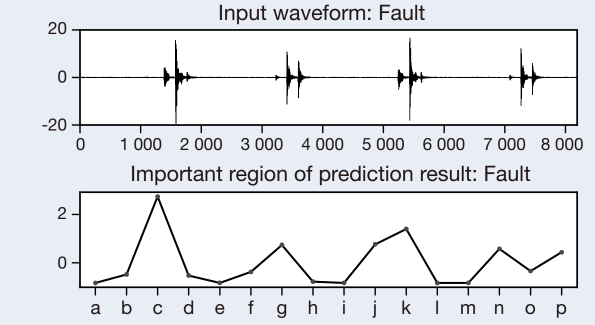

Fig. 13 Example of Grad-CAM result applied to high generalization performance model at epoch 4 with fault waveform input

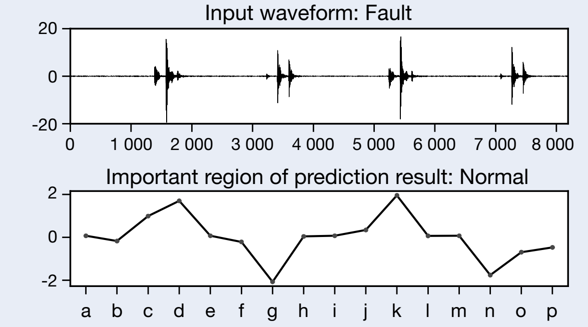

Fig. 14 Example of Grad-CAM result applied to high generalization performance model at epoch 10 with fault waveform input

4. Summary

Using Grad-CAM, the features extracted by the diagnostic model show high generalization performance in the deep learning model that diagnoses the presence or absence of flaking from the vibration acceleration data during normal and flaking of rolling bearings. As a result, it was confirmed that Grad-CAM can visualize the important region in the input data in the diagnostic model.

In addition, in the diagnostic model showing high generalization performance, periodic impact vibration, which is a feature common to flaking vibration, was extracted. Furthermore, it was confirmed that even when noise was added to the input data, periodic impact vibration was extracted. On the other hand, it was found that generalization performance could be degraded by over-fitting; however, it became clear that over-fitting could be determined through a method such as Grad-CAM.

In the future, we would like to formulate a method to verify the validity of the learning results and apply the method to the field data.

References

1) Randall, R. B. and Antoni, J., “Rolling element bearing diagnostics–A tutorial,” *Mechanical systems and signal processing*, Vol. 25, No. 2 (2011), pp. 485–520.

2) Le, Q. V., “Building high-level features using large scale unsupervised learning,” in IEEE international conference on acoustics, speech and signal processing, May 26–31 (2013), Vancouver, BC. doi:10.1109/ICASSP.2013.6639343

3) Yoshimatsu, O., Satou, Y., and Shibasaki, K., “Rolling bearing diagnosis based on CNN-LSTM and various condition dataset,” Proceedings of the Annual Conference of the PHM Society, Vol. 10, No. 1 (2018).

4) Krizhevsky, A., Sutskever, I., and Hinton, G. E., “ImageNet classification with deep convolutional neural networks,” in proceedings of the 2012 advances in neural Information processing systems, December 3–6 (2012), Lake Tahoe, NV. pp. 1,097–1,105.

5) Graves, A. and Schmidhuber, J., “Framewise phoneme classification with bidirectional LSTM and other neural network architectures,” *Neural networks*, Vol. 18, No. 5–6 (2005), pp. 602–610.

6) Laparo, K. A., “Case Western Reserve University Bearing Data Center” (2012).

7) Ramprasaath, R. S., Michael C., Abhishek D., Ramakrishna V., Devi P., and Dhruv B., “Grad-CAM: Visual Explanations from Deep Networks via Gradientbased Localization,” (2016), arXiv: 1610.02391

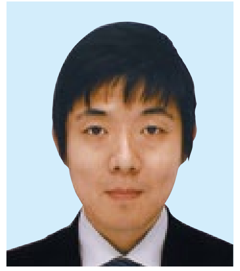
Osamu Yoshimatsu


Yoshihiro Satou


Kenichi Shibasaki

Long Life Material for Local Procurement (SHJ7)

To reduce the size and weight of a transmission (T/M) designed to improve the fuel efficiency and power consumption efficiency of automobiles, it is necessary to reduce the size and weight of its rolling bearings. However, with smaller bearings, durability decreases and damage is more likely to occur. The most common type of T/M bearing damage is the flaking caused by indentations formed by the ingress of foreign matter inside the lubricant. Bearings for T/Ms therefore need greater durability against indentation-originated flaking.

NSK has developed bearings with specifications for measures against this kind of flaking, but they require special time intensive heat treatment processes and NSK original materials. The problem of local production of long-life bearings has thus been difficult, while at the same time automobile production overseas has increased. To solve the problem, we developed materials that are easy to procure globally and have created technologies that can extend bearing life without the need for special heat treatment.

1. Features

1.1. Improvement of material availability

Since materials were developed using ISO standard steel, which can be easily procured globally, local procurement of the material is also easy.

1.2. Improvement of heat treatment efficiency

The required life is secured without the need for heat treatment technology in a special environment over a long period. With the establishment of this technology, it is now possible to reduce the energy used during production.

1.3. Longer service life

The service life limited by indentation-originated flaking is 1.5 times longer than that of standard bearings (Fig. 1). This allows for downsizing and weight reduction, leading to low friction. The weight of the bearing can be reduced by about 20% compared to the standard bearing (Fig. 2). Furthermore, the bearing has a longer life for other modes of flaking as well (Fig. 3).

Photo 1 Tapered roller bearing made of SHJ7 material

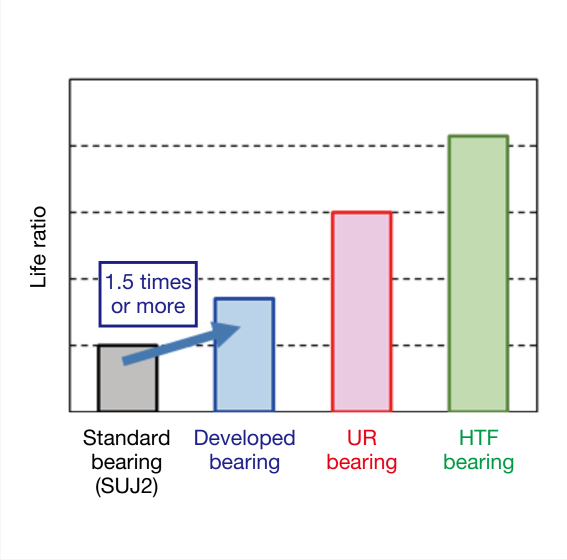

Fig. 1 Life test results under contaminated conditions

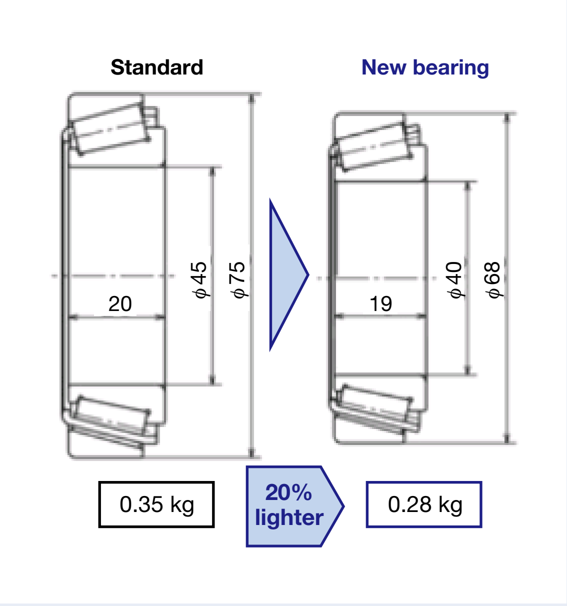

Fig. 2 Weight-saving effects of new product

2. Applications

The technology that makes possible the product's long service life, low torque, small size, and light weight can be applied to all types of T/Ms.

3. Summary

SHJ7 materials have bearing life extension effects even though they are procurable and do not require special heat treatment. They also contribute to the high reliability, low torque, compactness, and weight reduction of bearings for T/Ms.

NSK will actively continue to develop and propose products that meet the needs of the rapidly changing automobile market.

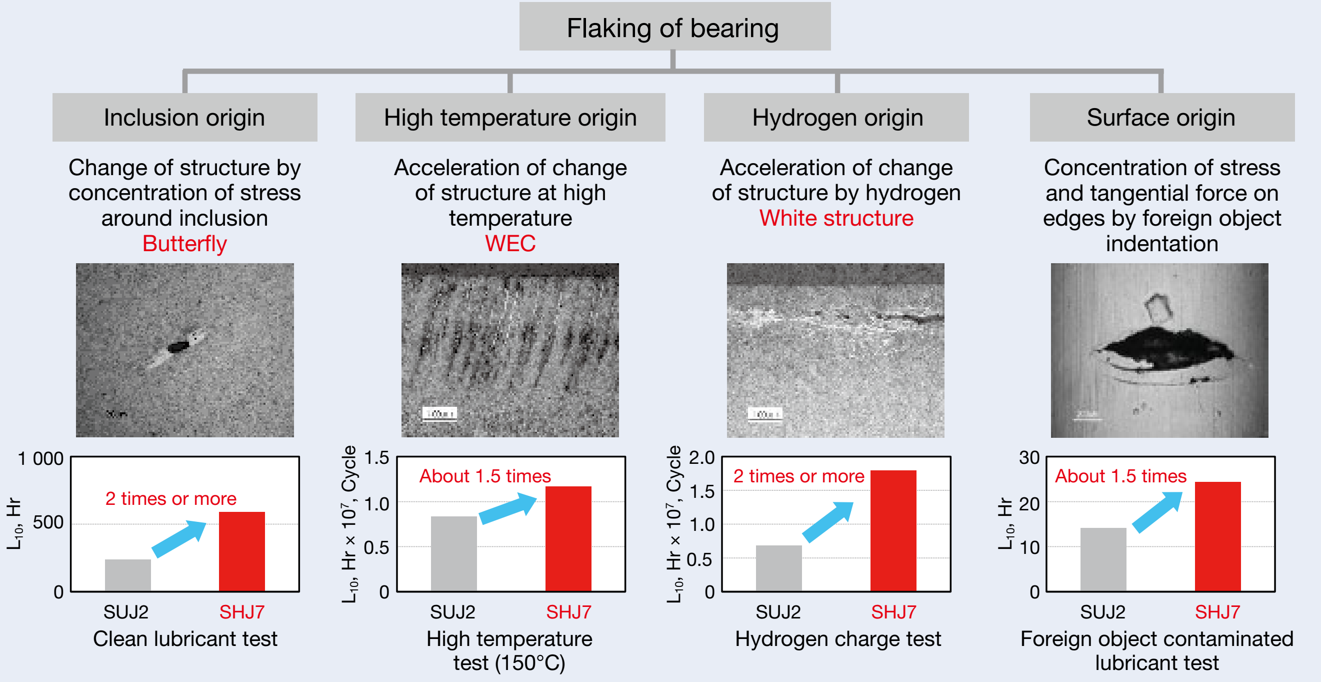

Fig. 3 Bearing life characteristics of SHJ7

High-Performance Tapered Roller Hub Unit Bearings for Automobiles

Hub unit bearings are key components at the center of automobile wheels. Their structure consists of rolling bearings that support the wheels and the suspension peripheral components, such as the hub shaft, as a unit. Hub unit bearings are progressing forward with the adoption of unitization technology while still incorporating peripheral components from generation 1 (HUB 1) to generation 3 (HUB 3) technologies.

Pickup trucks, large SUVs, and commercial vehicles often use tapered roller hub unit bearings. This is due to tapered roller bearings having a longer service life and higher rigidity than ball bearings of the same size. On the other hand, ball bearings, which are widely used for passenger cars, are widely applied up to generation 3 (integrated hub shaft), while many tapered roller bearings are limited to single-row, two-piece use or use with generations 1 and 2 due to manufacturing constraints.

Subsequently, a hub shaft must be assembled when replacing a hub bearing for car manufacturers and markets, and press-fit defects as well as excessive or insufficient tightening force lead to market failures such as the occurrence of abnormal noise. Against this background, the need for generation 2.5 (hub shaft assembly) and generation 3 technologies are increasing.

In addition, environment regulations and fuel efficiency standards have been strengthened in various countries, while efforts to improve fuel efficiency have been expanding beyond just passenger cars. In this context, reducing friction in tapered roller hub unit bearings is a key issue.

NSK has developed high-performance tapered roller hub unit bearings, which contribute to improved reliability as well as fuel efficiency reduction of automobiles through promoting the application of unitization and low-friction technologies to meet these needs.

Photo 1 High-performance tapered roller hub unit bearing

1. Advantages

1.1 Improvement in reliability through unitization

Generation 2.5 was developed with a pre-assembled hub shaft for the current generation 2 tapered roller hub unit bearings. In addition, the generation 3 system that integrates the hub shaft and inner ring is also under development.

NSK contributes to improvements in reliability in the marketplace through implementing hub shaft assembly and preload control to prevent improper assembly such as the creation of defects when the hub shaft is press-fitted with either excessive or insufficient tightening force.

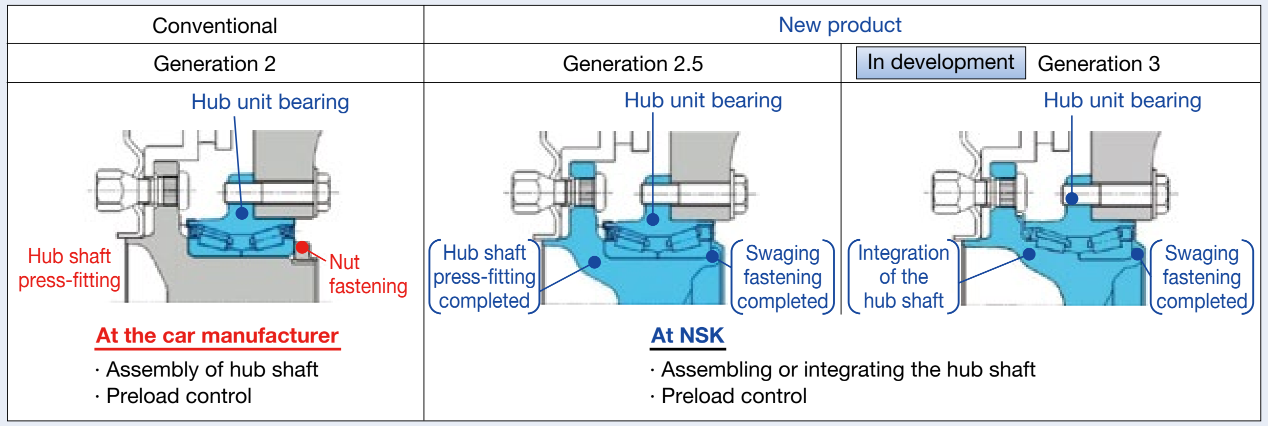

Fig. 1 Tapered roller hub unit bearing generation

1.2 Adoption of low-friction technologies

Low-friction technologies such as grease, seals, high sealing performance caps, which NSK has developed for ball bearings for passenger cars, have also been applied to tapered roller hub unit bearings.

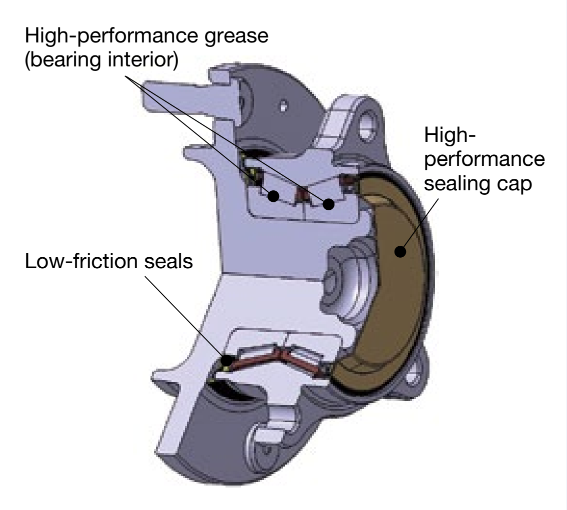

Fig. 2 Structure of the tapered roller hub unit bearing and low-friction seals

1.2.1 High-performance grease

Low-friction grease is applied to reduce friction inside the bearing. A grease has been developed that includes a base oil with low kinematic viscosity and demonstrates small changes in viscosity in relation to changes in temperature, thereby ensuring low friction and sufficient viscosity even in high temperatures and a high load range.

By adjusting the composition and type of the additive, the high-performance grease has a water-resistant effect of detoxifying water that has entered the bearing and can contribute to achieving high reliability.

1.2.2 Low-friction seals

In order to reduce friction with the seal, a reduction in the reaction force of the seal lip and low-friction seal grease are applied. The lip reaction force is reduced by optimizing the surface pressure distribution by FEM analysis to achieve both low friction and improved muddy water resistance.

For the seal grease, low-friction seal special grease is applied. It has a base oil that is low in kinematic viscosity and demonstrates small changes in viscosity in relation to changes in temperature while not affecting the functionality even when mixed with internal grease. Since there is little change in viscosity due to the temperature, a friction-reducing effect can be expected not only for dynamic torque at normal temperatures but also for torque at low temperatures.

1.2.3 High-performance sealing caps

Since the non-driven wheel does not contain a drive shaft inside the hub shaft, on the inboard side, it is possible to employ a high-performance sealing cap that does not cover the seal but rather the end face. Along with this, the seal on the inboard side is eliminated, and therefore friction due to seal sliding can be reduced to zero.

In addition, the high-performance sealing cap also possesses a high sealing property that protects against the infiltration of muddy water by vulcanizing and bonding rubber to a fitting portion with the outer ring, which can contribute to improvements in reliability as well.

The application of these low-friction technologies has reduced friction by roughly 20% to 35% (compared to generation 2 technologies). In addition, changing to generation 3 can further reduce friction by about 10%.

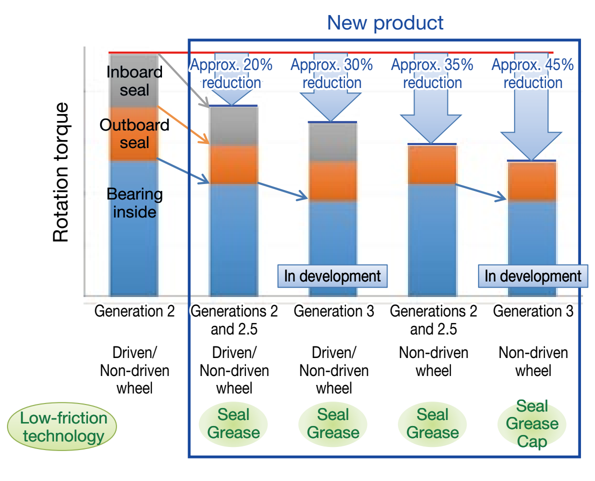

Fig. 3 Friction reduction calculation

2. Summary

We have developed high-performance tapered roller bearings for pickup trucks, large SUVs, and commercial vehicles. These achieve both improvements in reliability and lower friction through promoting the unitization of hub bearings as well as by applying low-friction technologies developed in a ball hub unit bearing such as grease, seals, and high-performance sealing caps.

We will continue contributing to improvements in the reliability of automobiles and reducing the burden placed upon the global environment through the development of these high-performance products for the market.

Low-Noise Thrust Needle Roller Bearing

In recent years, improving automobile fuel efficiency has become a critical issue for automobile manufacturers as they strive to address global environmental problems. Two technologies that help against this problem are the electric vehicle (hereinafter referred to as an EV) and the hybrid car (hereinafter referred to as an HEV), the numbers of which have been increasing in Japan, Europe, China, and other countries and regions, and their share of total automobile production has also increased.

Until now, the main functions required for bearings were miniaturization, weight reduction, and long life, but new problems such as noise are expected to emerge.

NSK has been conducting research and development in regard to these new issues and with a view toward the future. In this article, we will introduce the Low-Noise Thrust Needle Roller Bearing for EVs and HEVs.

Photo 1 Low-noise thrust needle roller bearing

1. Fields for Application

HEVs run on a motor when the vehicle starts or is moving at a low speed, at which times the engine is off. Furthermore, when decelerating, the engine is stopped, and the motor is driven by the inertia force to generate electric power.

When the engine is not running, it is quiet with low road noise, and it is assumed that operation noise is significant.

HEVs are equipped with an engine and a motor. In order to use both efficiently, normally the power transmissions after the output are unified and installed in the same place. For this reason, the transmission has been equipped in the same manner as before and could be applied to this transmission.

2. Noise Generation Factor (Conventional Structure)

The main cause of bearing noise is the contact between the components, rolling or sliding. With thrust needle bearings, the following are considered to be the sources of noise.

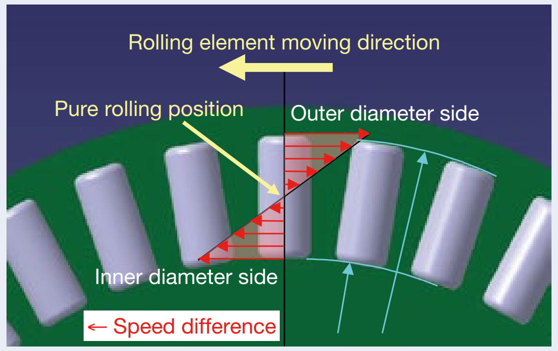

Fig. 1 Causes of rolling and sliding noise between the rollers and race

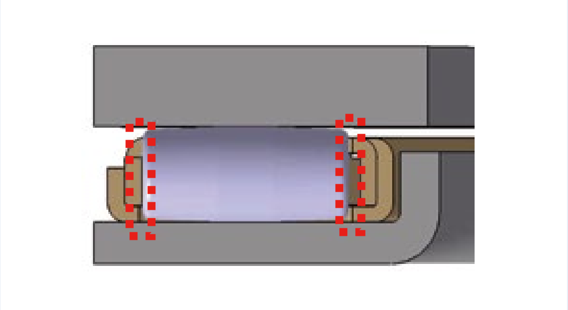

Fig. 2 Where sliding noise occurs between the cage and rollers

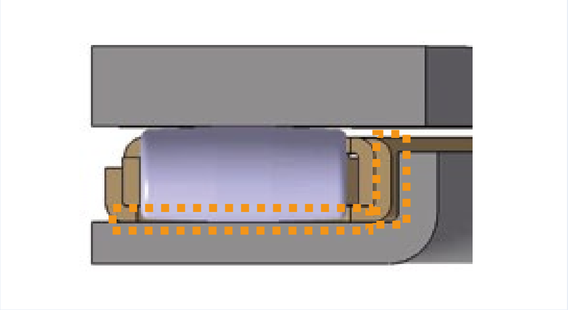

Fig. 3 Where sliding noise occurs between the cage and race

(1) Rolling and slipping noise of rollers and race

The rotation direction of the bearing does not coincide with that of rollers, and a speed difference from the race occurs on the outer diameter side and inner diameter side of the rollers. This speed difference generates rolling or slipping noise.

(2) Slipping noise of the cage and roller

The rollers rotate while pushing the cage, and they slide at the contact portion. This sliding generates slipping noise.

(3) Slipping noise of the cage and race

The rotating cage is unlikely to come into contact with the race due to lubricating oil or the like. However, the cage posture is stabilized by the support of the race, and slight sliding occurs. This sliding generates slipping noise.

3. Features

In regard to the cause of noise previous mentioned, this product has improved quietness by the following methods.

(1) Improved roundness of the roller crowning

(2) Optimization of the race shape

The aim is to reduce rolling and slipping noise of the rollers and race. (1) Rolling noise generated by the speed difference is suppressed by improved roundness accuracy of the crowning part, where the speed difference occurs most. (2) Slipping is suppressed by adopting a race shape that makes the speed difference unlikely to occur.

(3) Adoption of a resin cage

To reduce slipping noise between the cage and roller as well as the cage and race, a resin cage has been adopted, and its self-lubricating property has reduced slipping noise.

The new product has shown a noise reduction effect of approximately 10% compared to conventional products. Even if the rotation speed is changed, there is little change in the effect, and it is assumed that the new product can cope with the high rotation speed of the motor.

4. Summary

Road and wind noise are regarded as the main types of noise in cars. However, the noise sources of EVs and HEVs are mechanical in nature and occur when the car stops or runs at a low speed. This product is expected to become essential as travel by EV increases in the future.

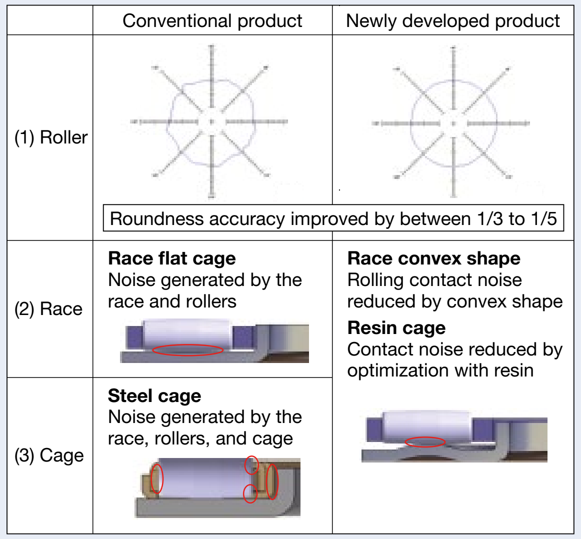

	Conventional product	Newly developed product
(1) Roller	Roundness accuracy improved by between 1/3 to 1/5	
(2) Race	**Race flat cage** Noise generated by the race and rollers	**Race convex shape** Rolling contact noise reduced by convex shape **Resin cage** Contact noise reduced by optimization with resin
(3) Cage	**Steel cage** Noise generated by the race, rollers, and cage	

Fig. 4 Comparison of conventional and newly developed products

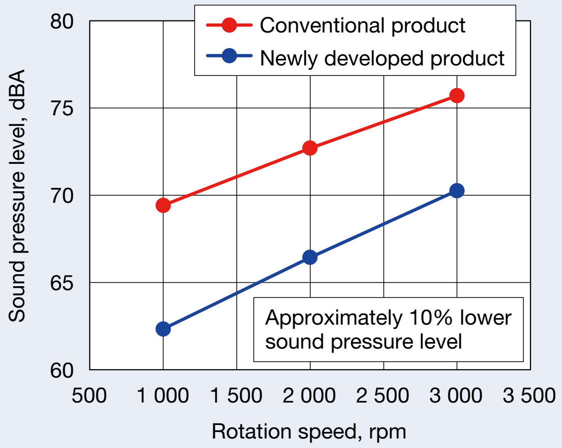

Fig. 5 Noise in conventional products vs. newly developed product

High-Performance Low-Friction Seal for Single-Row Deep Groove Ball Bearings

Motors for automobiles, home appliances, and the like may be used in an environment exposed to water droplets, dust, etc. In order to prevent external foreign substances from entering the bearing in such environments, a contact rubber seal having excellent sealing properties is used. Generally, the higher the sealing property, the greater the friction generated on the seal sliding surface. On the other hand, this friction has hindered high sealing in applications where high efficiency and high-speed rotation of rotating equipment are required.

NSK has generally offered two types of seals: high-sealing contact seals with an emphasis on sealing and low-friction contact seals with a focus on friction, and these are selected in accordance with the particular usage environment and applications.

Now we have introduced a contact seal (Photo 1) that achieves both sealing performance and low friction, with an optimized design for the seal structure and contact part to suit both application needs.

Photo 1 Single-row deep groove ball bearings with high-performance low-friction seal

1. Composition, Structure, and Specifications

As shown in Figure 1, both sealing performance and low friction were achieved by optimizing the shape of the contact portion between the seal lip and inner ring, and also by optimizing the design of the pressing force (lip reaction force) of the seal against the inner ring.

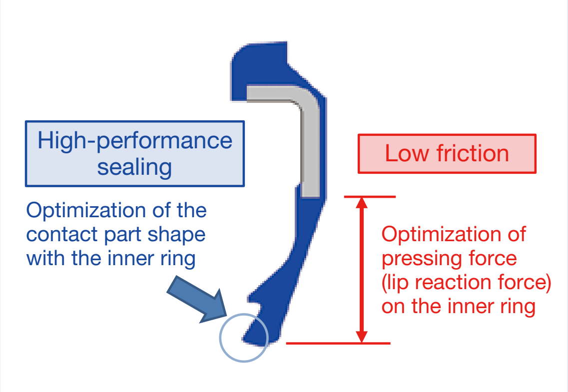

Fig. 1 Cross-section of a high-performance low friction seal

2. Advantages

- Sealing performance

By optimizing the shape of the contact area with the inner ring, the same sealing performance as the high-sealing contact seal is ensured. As shown in Figure 2, the results of a comparison of the amount of water penetration in the water injection test showed the sealing performance equivalent to the high-sealing contact seal.

- Low friction

By optimizing the seal structure, the force for pressing the seal lip against the inner ring has been reduced. Moreover, as shown in Figure 3, the friction has been significantly reduced compared to the low-friction contact seal.

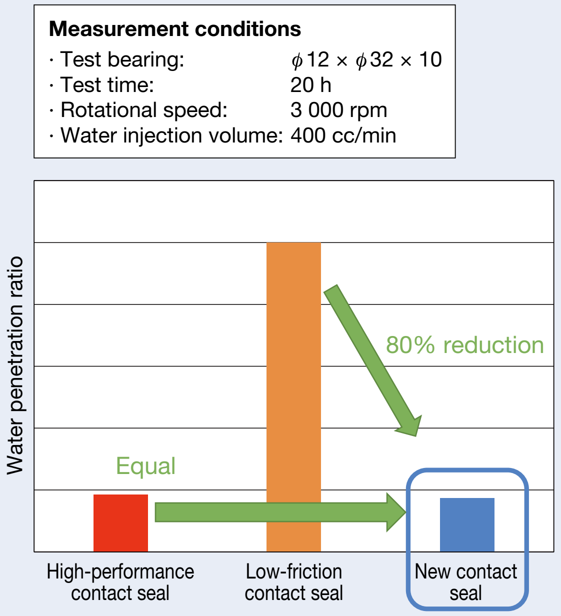

Measurement conditions
· Test bearing: $\phi 12 \times \phi 32 \times 10$
· Test time: 20 h
· Rotational speed: 3 000 rpm
· Water injection volume: 400 cc/min

Fig. 2 Results of the comparison of amounts of water penetration in the water injection test

3. Applications

Single-row deep groove ball bearings incorporating this product are suitable for automobile motors, motors for industrial machines, motors for home appliances, and more.

4. Summary

This high-performance seal is used for small-diameter and average-diameter single-row deep groove ball bearings, contributing to improved reliability and significant energy savings.

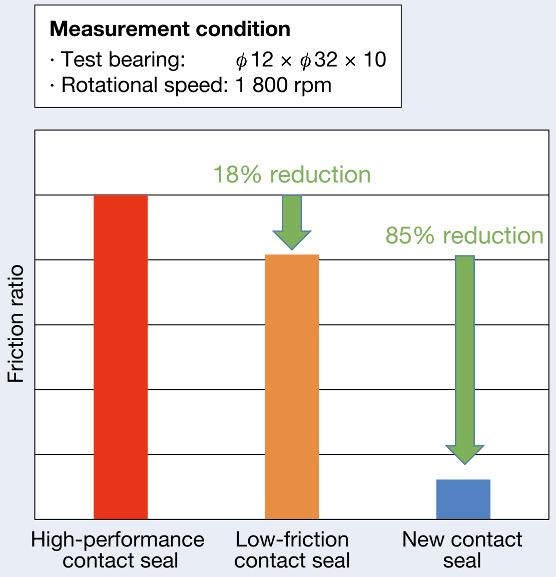

Measurement condition
· Test bearing: $\phi 12 \times \phi 32 \times 10$
· Rotational speed: 1 800 rpm

Fig. 3 Seal friction test results

Lightweight High-Performance Intermediate Shaft

The intermediate shaft is important because it has been given the responsibility of turning, which is among the car's three major functions: running, turning, and stopping. The following functions and performance are required, from vehicle assembly to long-term use.

- Light sliding force
- Comfortable steering and its durability
- High strength
- Fuse function (protection against excessive torque)
- Lightweight

NSK has recently developed an intermediate shaft, introduced below, that satisfies these functions at a high level of performance.

1. Composition, Structure, and Specifications

Photo 1 shows the intermediate shaft with the new structure. Photo 2 shows the main component shaft. Figure 1 is a cross-sectional view of the intermediate shaft that shows its structure, function, and performance.

The shaft and tube are fitted together with a spline that provides a sliding mechanism.

The shaft is made lighter with a hollow material. In addition, the thickness in the vicinity of the spline portion was made thinner, allowing for both light sliding force and a comfortable feeling while steering.

In addition, part of the shaft is a thinner fuse section. When excessive torque is input, the thin fuse section is twisted with the set torque, so it prevents a further increase of torque and protects other peripheral components.

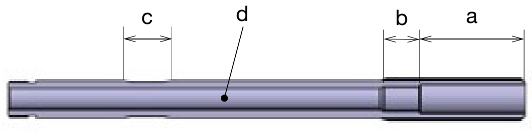

Portion	Structure	Function and Performance
a	Hollow and thin	Light sliding force Comfortable steering and its durability
b	Thick portion	High strength
c	Thin section	Fuse function
d	Hollow	Lightweight

Fig. 1 Structure of new hollow shaft for each function and Performance

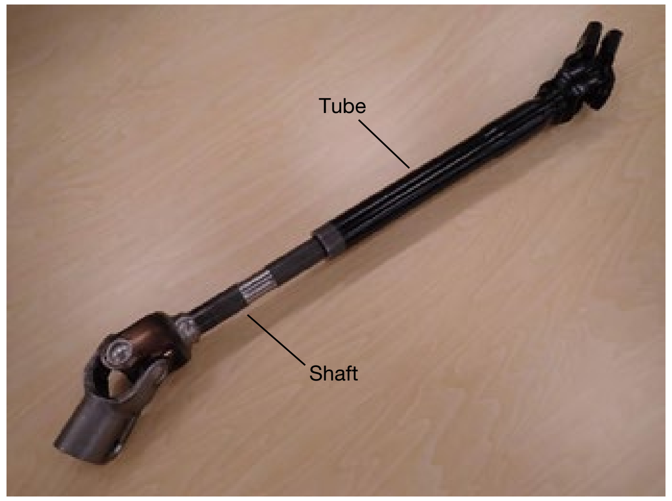

Photo 1 Intermediate shaft with new structure

Photo 2 New hollow structure shaft

2. Features

(1) Achieving both light sliding force and comfortable steering and ensuring high strength

The shaft side spline is coated with resin. When this resin is cut into a spline shape, the sliding force and steering feeling are balanced by adjusting the interference with the tube. Comfortable steering means that there is no backlash in the fitting portion, which is contrary to the light sliding force.

The balance range in the conventional solid shaft is narrow, and to allow for comfortable steering, the standard range of the sliding force must be widened, that is, the process capability cannot be established unless the sliding force is set slightly higher.

In the new mechanism, a hollow shaft is used, and the thickness of the spline section is made very thin to reduce sensitivity of the fitting section in relation to the interference. As a result, the balance range between the sliding force and steering comfort was widened, and as a result the sliding force could be reduced, even with the same level of comfort while steering. (a in Figure 1)

Moreover, high torque transmission strength is secured by limiting the range of the thin portion and leaving the thick portion. (b in Figure 1)

(2) Durability of comfortable steering

The spline sliding portion is worn or settled by long-term use, and when a gap finally forms, rattling can be felt in the steering.

In conventional products, the elasticity of the resin mainly compensates for wear and settling, thereby suppressing rattling. The new mechanism further improves its durability.

As described above, the new mechanism has a hollow shaft and further reduces the thickness of the spline portion, while the shaft itself is more elastic than those of conventional products. That is, in addition to the elasticity of the resin, the elasticity of the shaft compensates for wear and settling, thereby improving durability in terms of steering comfort. (a in Figure 1)

(3) Fuse function

The fuse is portion c in Figure 1 where the diameter is reduced, and it has been designed to be the weakest portion in the steering system. If an excessive external force is applied to the steering system due to an accident or the like, the fuse has the function of twisting earlier than other components with the set torque. Also, it has a sufficient twist angle and cannot be easily twisted off. The function of the fuse prevents damage to other components and suppresses sudden running failure.

If an abnormality occurs in which the fuse portion is twisted, the steering wheel center shifts, notifying the driver that the vehicle has been damaged.

Since the damage to other components is reduced, there is a possibility of repairing it by simply replacing the intermediate shaft.

(4) Lightweight

By using a hollow material, the shaft is about 40 % lighter than the conventional solid structure. Specifically, the weight of the intermediate shaft, which has recently been mass-produced, has been reduced by approximately 150 g. (d in Figure 1)

3. Applications

The new intermediate shaft satisfies the basic requirements of light sliding force, comfortable steering, and durability, and is strong and lightweight, with the expectation that it will be used in a wide range of vehicles. In addition, since the specifications of the fuse function can be adjusted according to the cutting shape, the shaft can accommodate the requirements for each vehicle.

4. Summary

The lightweight high-performance intermediate shaft introduced here has already been mass-produced, and its use will further expand in the future.

We will promote the development of this product to provide comfortable steering, improve vehicle mobility by reducing weight, and contribute to reducing impact on the environment.

Touchdown Bearings for the Superconducting Flywheel Power Storage System

The superconducting flywheel power storage system is a mechanical battery that converts electric power into kinetic energy by rotating the flywheel and stores the kinetic energy. It can convert the kinetic energy back to electric power as necessary and also smoothen unstable power affected by weather conditions such as solar and wind power.

The rotating shaft of the superconducting flywheel is supported by the superconducting magnetic bearing without any mechanical loss, as it levitates without any contact. However, in an emergency when the superconducting magnetic bearing loses function and its magnetic levitation force, rolling bearings (touchdown bearings) that can support the rotating shaft of a four-ton flywheel are required (Figure 1).

NSK has developed touchdown bearings for the superconducting flywheel that can support the rotating shaft of a four-ton flywheel from its maximum rotation speed of 3 000 rpm until a complete stop, even if the superconducting magnetic bearing loses function, as introduced below (Photo 1).

Photo 1 Touchdown bearing for superconducting flywheel energy storage systems

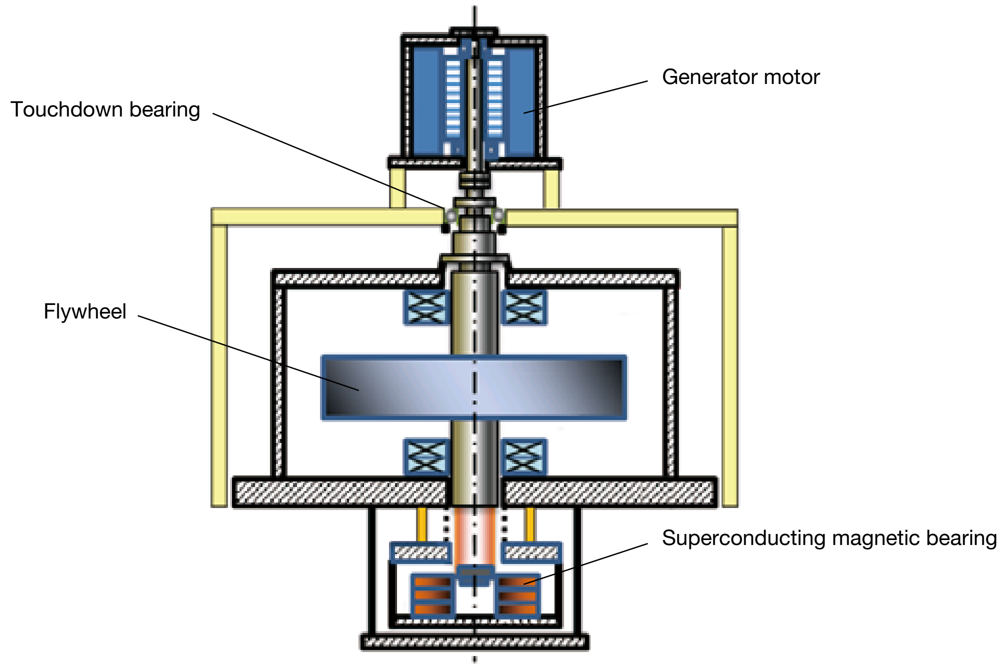

Fig. 1 Structure of the superconducting flywheel power storage system

1. Configuration, Structure, and Specifications

Touchdown bearings for the superconducting flywheel power storage system follow the design concept of the touchdown bearings for turbomolecular pumps, which have a proven track record, and prevent damage due to the rapid temperature rise during touchdown.

Reliability was improved by using heat-resistant bearing steel M50 for the outer and inner rings and silicon nitride ceramic for the balls.

2. Features

(1) Bearing Design

Since the touchdown bearings instantaneously rotate at high speeds in an emergency, the inner rings generate heat and expand ahead of the outer rings due to the internal friction of the bearings and slippage of the rotating shaft and inner rings. This raises the concern that abrasion, or burn-in, may occur due to the excessively small radial clearances. The damage due to excessively small radial clearances can be prevented with a design that reduces heat generation by reducing the diameter of the ball as well as a design that increases the heat capacity (volume) of the inner rings by increasing the diameter of the ball pitch (Figure 2) and suppressing the amount of expansion due to heat generation (Figure 3).

(2) Bearing Material

In consideration of rapid heat generation, M50 was adopted for the outer and inner rings. The material of the ball is a silicon nitride ceramic with excellent wear resistance, a small coefficient of linear expansion, and a reduced amount of radial clearance for the rising temperature. The inner ring is coated with a proprietary DLC (diamond-like carbon) coating to improve lubricity.

3. Applications

The touchdown bearings are being used in the superconducting flywheel power storage system demonstration test machines installed at the power storage technology research site of the Komekurayama Solar Power Plant in Yamanashi Prefecture. This is to verify the smoothing effect of the photovoltaic power and margin of the emergency braking function.

4. Summary

There are various applications for the superconducting flywheel power storage system such as in the regeneration lapse of electric railways, and we will continue to develop bearings suitable for these applications.

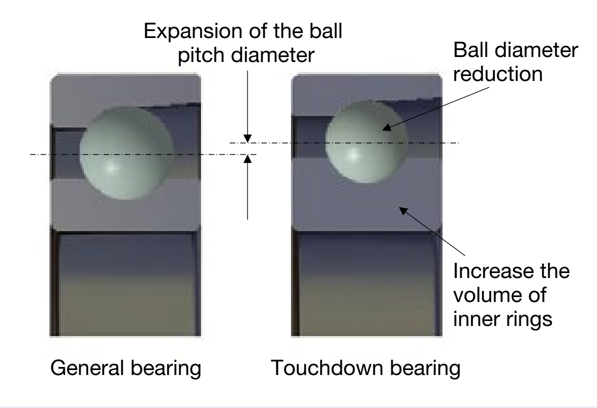

Fig. 2 Design specifications of the touchdown bearings

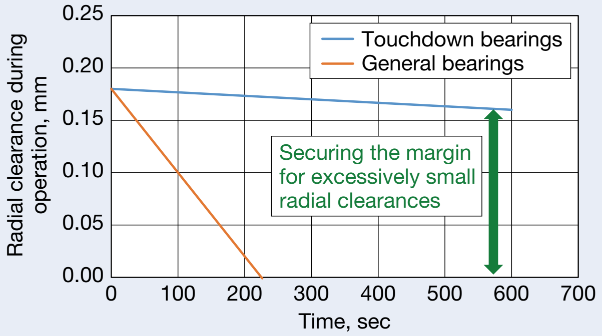

Fig. 3 Calculation results of the radial clearances during operation after touchdown

Reference

T. Yamashita, Y. Miyazaki, M. Ogata, K. Nagashima, Y. Shimazaki, M. Taniguchi, S. Harui, and K. Hara, "Key Technology of the Superconducting Flywheel Energy Storage Demonstration Machine," *RTRI Report*, Vol. 33, No. 5, May 2019, pp. 36–38.

NSK K1-L Lubrication Unit

Linear guides are used in machines, and lubrication is especially important for ensuring their long-term performance. The issue, however, is ensuring that the lubrication is maintained while also reducing work for the user, lowering the frequency of machine shutdowns, and increasing production efficiency.

NSK has developed the world's first lubrication unit NSK K1 and has contributed to long-term maintenance-free machines for more than 20 years since its launch in 1996. Furthermore, the clean lubrication system has greatly contributed to improvements in terms of protecting the environment.

In recent years, however, smart factory and automation technologies are being rapidly developed, and there is strong demand for improved machine reliability and extended maintenance intervals.

To address these issues, NSK developed the new lubrication unit NSK K1-L (Photo 1) with improved lubricant supply performance.

1. Structure and Specifications

NSK K1-L is made of a porous resin containing a large amount of lubricant and supplies lubricant to the linear guide over a long period as the internal lubricant gradually seeps out. As with conventional NSK K1, the lubricant is continuously supplied by attaching it to both ends of the slider and moving it while contacting the raceway surface of the rail (Figure 1).

Figure 1 shows NSK K1-L attached to both ends of the slider one by one, but increasing the number of attachments is possible if necessary.

NSK K1-L is available in three models: NH15, NH20, and NH25.

2. Features

(1) Extension of lubricant supply period

With the new oil-impregnated material, the lubricant supply period of NSK K1-L has been extended by approximately twice as long as conventional NSK K1.

Figure 2 shows the durability test results of the linear guides with the lubrication unit. These results reflect use of the lubricant supplied only from the lubrication unit without filling in grease or the like. The linear guide with NSK K1-L has significantly improved the travel distance compared to the conventional NSK K1.

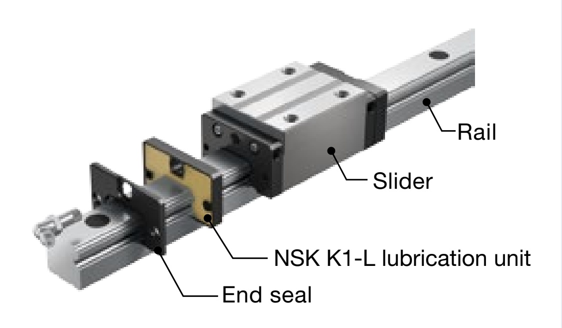

Fig. 1 Structure of the NSK K1-L lubrication unit

Photo 1 NSK K1-L lubrication unit

(2) Reduction of dynamic friction force

NSK K1-L has reduced the dynamic friction force when driving sliders by reviewing the contact structure with the rail.

Figure 3 shows the results of measuring the dynamic friction force of a linear guide with a lubrication unit. These are the results of measurements at different speeds in the range of 1 to 120 m/min. The linear guide with NSK K1-L significantly reduced dynamic friction force compared to the conventional NSK K1-equipped product.

3. Applications

By attaching NSK K1-L to the linear guides used in various transportation devices, it becomes possible to extend the maintenance interval compared to the conventional NSK K1. In addition, the dynamic friction force when driving the sliders is reduced, making it easier to use in terms of increasing speed and tact time and saving energy.

4. Summary

With a primary focus on its application in transportation systems, there are plans to roll out NSK K1-L for the NH Series and NS Series, which are general-purpose series of NSK linear guides.

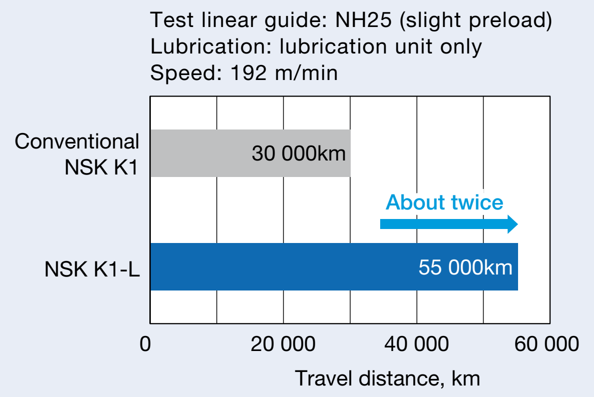

Fig. 2 Durability test results of the linear guide with the lubrication unit

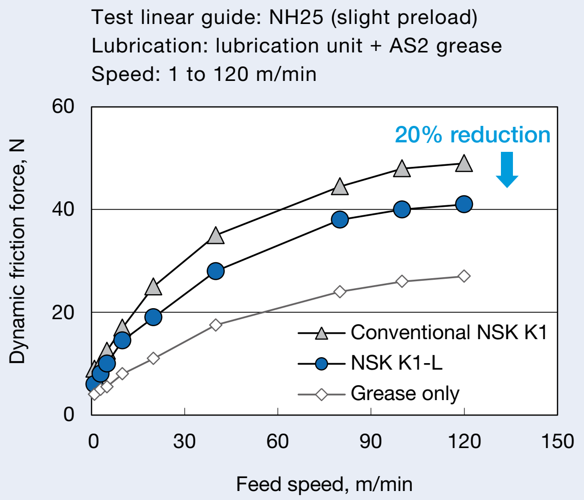

Fig. 3 Dynamic friction force test results of the linear guide with the lubrication unit

Worldwide Sales Offices

P: Phone F: Fax ☆: Head Office

NSK LTD.-HEADQUARTERS, TOKYO, JAPAN

Nissei Bldg., 1-6-3 Ohsaki, Shinagawa-ku, Tokyo 141-8560, Japan
INDUSTRIAL MACHINERY BUSINESS DIVISION-HEADQUARTERS
P: +81-3-3779-7227 F: +81-3-3779-7432
AUTOMOTIVE BUSINESS DIVISION-HEADQUARTERS
P: +81-3-3779-7189 F: +81-3-3779-7917

●Africa

South Africa:
NSK SOUTH AFRICA (PTY) LTD.
SANDTON 25 Galaxy Avenue, Linbro Business Park, Sandton 2146, South Africa
P: +27-011-458-3600 F: +27-011-458-3608

●Asia and Oceania

Australia:
NSK AUSTRALIA PTY. LTD.
MELBOURNE ☆ 100 Logis Boulevard, Dandenong South, Victoria, 3175, Australia
P: +61-3-9765-4400 F: +61-3-9765-4466
SYDNEY Suite A315, 20 Lexington Drive, Bella Vista, New South Wales, 2153, Australia
P: +61-2-9839-2300 F: +61-2-8824-5794
BRISBANE 1/69 Selhurst Street, Coopers Plains, Queensland 4108, Australia
P: +61-7-3347-2600 F: +61-7-3345-5376
PERTH Unit 1, 71 Tacoma Circuit, Canning Vale, Western Australia 6155, Australia
P: +61-8-9256-5000 F: +61-8-9256-1044

New Zealand:
NSK NEW ZEALAND LTD.
AUCKLAND Unit F, 70 Business Parade South, Highbrook, Business Park Auckland 2013, New Zealand
P: +64-9-276-4992 F: +64-9-276-4082

China:
NSK (SHANGHAI) TRADING CO., LTD.
JIANGSU No.8 NSK Rd., Huaqiao Economic Development Zone, Kunshan, Jiangsu, China (215332)
P: +86-512-5796-3000 F: +86-512-5796-3300

NSK (CHINA) INVESTMENT CO., LTD.
JIANGSU ☆ No.8 NSK Rd., Huaqiao Economic Development Zone, Kunshan, Jiangsu, China (215332)
P: +86-512-5796-3000 F: +86-512-5796-3300
BEIJING Room 1906, Beijing Fortune Bldg., No.5 Dong San Huan Bei Lu, Chao Yang District,
Beijing, China (100004)
P: +86-10-6590-8161 F: +86-10-6590-8166
TIAN JIN Unit 4604, 46/F., Metropolitan Tower, 183 Nanjing Road, Heping District,
Tianjin, China (300051)
P: +86-22-8319-5030 F: +86-22-8319-5033
CHANGCHUN Room 902-03, Changchun Hongwell International Plaza, No.3299 Renmin Street,
Changchun, Jilin, China (130061)
P: +86-431-8898-8682 F: +86-431-8898-8670
SHENYANG Room 1101, China Resources Building, No. 286 Qingnian Street,
Heping District, Shenyang Liaoning, China (110004)
P: +86-24-2334-2868 F: +86-24-2334-2058
DALIAN Room 1805 Xiwang Tower, No.136 Zhongshan Road,
Zhongshan District, Dalian, Liaoning, China (116001)
P: +86-411-8800-8168 F: +86-411-8800-8160
NANJING Room A1 22F, Golden Eagle International Plaza, No.89 Hanzhong Road, Nanjing,
Jiangsu, China (210029)
P: +86-25-8472-6671 F: +86-25-8472-6687
FUZHOU Room 1801-1811, B1#1A Class Office Building, Wanda Plaza, No.8 Aojiang Road,
Fuzhou, China (350009)
P: +86-591-8380-1030 F: +86-591-8380-1225
WUHAN Room 1512, No.198Yuncai Road, Office Building, Oceanwide City Square,
JiangHan, District, WuHan, China (400039)
P: +86-27-8556-9630 F: +86-27-8556-9615
QINGDAO Room 802, Farglory International Plaza, No.26 Xianggang Zhong Road, Shinan District,
Qingdao, Shandong, China (266071)
P: +86-532-5568-3877 F: +86-532-5568-3876
GUANGZHOU Room 1011-16, Yuexiu Financial Tower, No.28 Zhujiang Road East, Zhujiang
New Town, Guangzhou, Guangdong, China (510627)
P: +86-20-3817-7800 F: +86-20-3786-4501
CHANGSHA Room 3209, Huayuan International Center, No.36, Section 2, Xiangjiang Middle
Road, Tianxin District, Changsha, Hunan, China (410002)
P: +86-731-8571-3100 F: +86-731-8571-3255
LUOYANG Room 955, HUA-YANG PLAZA HOTEL, NO.88 Kaixuan W.Rd., Jian Xi District,
Luoyang,Henan Province, China (471003)
P: +86-379-6069-6188 F: +86-379-6069-6180
XI'AN Room 1007, B Changan Metropolls Center, No.88 Nanguanzheng Steet, Xi'an,
Shanxi, China (710068)
P: +86-29-8765-1896 F: +86-29-8765-1895
CHONGQING Room 612, Commercial Apartment, Athestel Hotel, No.288, Keyuan Rd.4,
Jiulongpo District, Chongqing, China (400039)
P: +86-23-6806-5310 F: +86-23-6806-5292
CHENGDU Room1117, Lippo Tower, No.62 North Kehua Road, Chengdu, Sichuan, China (610041)
P: +86-28-8528-3680 F: +86-28-8528-3690

NSK CHINA SALES CO., LTD.
JIANGSU No.8 NSK Rd., Huaqiao Economic Development Zone, Kunshan, Jiangsu, China (215332)
P: +86-512-5796-3000 F: +86-512-5796-3300

NSK HONG KONG LTD.
HONG KONG ☆ Suite 705, 7th Floor, South Tower, World Finance Centre, Harbour City, T.S.T,
Kowloon, Hong Kong, China
P: +852-2739-9933 F: +852-2739-9323
SHENZHEN Room 624-626, 6/F, Kerry Center, Renminnan Road, Shenzhen, Guangdong, China
P: +86-755-25904886 F: +86-755-25904883

Taiwan:
TAIWAN NSK PRECISION CO., LTD.
TAIPEI ☆ 10F-A6, No.168, Sec.3, Nanjing East Rd., Zhongshan Dist., Taipei City 104,
Taiwan
P: +886-2-2772-3355 F: +886-2-2772-3300
TAICHUNG 3F. -2, No. 540, Sec. 3, Taiwan Blvd., Xitun Dist., Taichung City 407, Taiwan
P: +886-4-2708-3393 F: +886-4-2708-3395
TAINAN Rm. A1, 9F., No.189, Sec. 1, Yongfu Rd., West Central Dist., Tainan City 700,
Taiwan
P: +886-6-215-6058 F: +886-6-215-5518

India:
NSK BEARINGS INDIA PRIVATE LTD.
CHENNAI ☆ TVH Beliciaa Towers, 2nd Floor, Block I, No.71/1, MRC Nagar Main Road, MRC
Nagar, Chennai-600 028,India
P: +91-44-2847-9600 F: +91-44-2847-9601
MUMBAI No.321, A Wing, Ahura Centre, 82, Mahakali Caves Road, Andheri (E),
Mumbai-400 093, India
P: +91-22-2838-7787
JAMSHEDPUR 13/A, 2nd Floor, Circuit House Area, North West Layout, Road No.12, (Near Sai
Baba Mandir), Sonari, Jamshedpur–831 011, Jharkhand, India
P: +91-657–2421144
GURGAON Unit No. 202, 2nd Floor, ‘A' Block, Iris Tech Park, Sector – 48 (Sohna Road),
Gurgaon–122018, India
P: +91-124-4838000

Indonesia:
PT. NSK INDONESIA
JAKARTA Summitmas II, 6th Floor, Jl. Jend Sudirman Kav. 61-62, Jakarta 12190, Indonesia
P: +62-21-252-3458 F: +62-21-252-3223

Korea:
NSK KOREA CO., LTD.
SEOUL Posco Center (West Wing) 9F, 440, Teheran-ro, Gangnam-gu,
Seoul, 06194, Korea
P: +82-2-3287-0300 F: +82-2-3287-0345

Malaysia:
NSK BEARINGS (MALAYSIA) SDN. BHD.
SHAH ALAM ☆ No. 2, Jalan Pemaju, U1/15, Seksyen U1, Hicom Glenmarie Industrial Park,
40150 Shah Alam, Selangor, Malaysia
P: +60-3-7803-8859 F: +60-3-7806-5982
PRAI No.24, Jalan kikik, Taman Inderawasih, 13600 Prai, Penang, Malaysia
P: +60-4-3902275 F: +60-4-3991830
JOHOR BAHRU 88 Jalan Ros Merah 2/17, Taman Johor Jaya, 81100 Johor Bahru, Johor, Malaysia
P: +60-7-3546290 F: +60-7-3546291
IPOH No.10&10A, Jalan Industri Paloh, Kawasan Perindustrian Ringan Paloh,
30200 Ipoh, Perak,Malaysia
P: +60-5-2555000 F: +60-5-2553373

Philippines:
NSK REPRESENTATIVE OFFICE
MANILA 8th Floor The Salcedo Towers 169 H.V. Dela Costa St.,Salcedo Villege Makati
City, Philippines 1227
P: +63-2-893-9543 F: +63-2-893-9173

Singapore:
NSK INTERNATIONAL (SINGAPORE) PTE LTD.
SINGAPORE 238A, Thomson Road, #24-01/05, Novena Square Tower A, Singapore 307684
P: +65-6496-8000 F: +65-6250-5845

NSK SINGAPORE (PRIVATE) LTD.
SINGAPORE 238A, Thomson Road, #24-01/05, Novena Square Tower A, Singapore 307684
P: +65-6496-8000 F: +65-6250-5845

Thailand:
NSK BEARINGS (THAILAND) CO.,LTD.
BANGKOK 26 Soi Onnuch 55/1 Pravet Subdistrict, Pravet District, Bangkok 10250, Thailand
P: +66-2320-2555 F: +66-2320-2826

Vietnam:
NSK VIETNAM CO., LTD.
HANOI Techno Center, Room 204-205, Thang Long Industrial Park, Dong Anh District,
Hanoi, Vietnam
P: +84-24-3955-0159 F: +84-24-3955-0158

NSK REPRESENTATIVE OFFICE
HO CHI MINH CITY Suite 307, Metropolitan Building, 235 Dong Khoi Street, District 1,HCMC, Vietnam
P: +84-28-3822-7907 F: +84-28-3822-7910

Worldwide Sales Offices

P: Phone F: Fax ☆: Head Office

●Europe

United Kingdom:
NSK EUROPE LTD. (EUROPEAN HEADQUARTERS)
MAIDENHEAD Belmont Place, Belmont Road, Maidenhead, Berkshire SL6 6TB, U.K.
P: +44-1628-509-800 F: +44-1628-509-808

NSK UK LTD.
NEWARK Northern Road, Newark, Nottinghamshire NG24 2JF, U.K.
P: +44-1636-605-123 F: +44-1636-605-000

France:
NSK FRANCE S.A.S.
PARIS Quartier de l’Europe, 2 Rue Georges Guynemer, 78283 Guyancourt, France
P: +33-1-30-57-39-39 F: +33-1-30-57-00-01

Germany:
NSK DEUTSCHLAND GMBH
DUSSELDORF ☆ Harkortstrasse 15, D-40880 Ratingen, Germany
P: +49-2102-4810 F: +49-2102-4812-290
STUTTGART Liebknechtstrasse 33, D-70565 Stuttgart-Vaihingen, Germany
P: +49-711-79082-0 F: +49-711-79082-289
WOLFSBURG Tischlerstrasse 3, D-38440 Wolfsburg, Germany
P: +49-5361-27647-10 F: +49-5361-27647-70

Italy:
NSK ITALIA S.P.A.
MILANO Via Garibaldi 215, Garbagnate Milanese (Milano) 20024, Italy
P: +39-299-5191 F: +39-299-025778

Netherlands:
NSK EUROPEAN DISTRIBUTION CENTRE B.V.
TILBURG Brakman 54, 5047 SW Tilburg, Netherlands
P: +31-13-4647647 F: +31-13-4641082

Poland:
NSK REPRESENTATIVE OFFICE
WARSAW Ul. Migdalowa 4/73, 02-796, Warsaw, Poland
P: +48-22-645-1525 F: +48-22-645-1529

Russia:
NSK POLSKA SP. Z O.O.
SAINT-PETERSBURG Office I 703, Bldg 29, 18th Line of Vasilievskiy Ostrov, Saint-Petersburg, Russia, 199178
P: +7-812-332-5071 F: +7-812-332-5072

Spain:
NSK SPAIN S.A.
BARCELONA C/Tarragona, 161 Cuerpo Bajo, 2a Planta, 08014, Barcelona, Spain
P: +34-93-289-2763 F: +34-93-433-5776

Turkey:
NSK RULMANLARI ORTA DOGU TIC. LTD. STI.
ISTANBUL Cevizli Mahallesi. D-100 Güney Yanyolu, Kuriş Kule İş Merkezi No:2 Kat:4, P.K.:
34846, Cevizli-Kartal-Istanbul, Turkey
P: +90-216-5000-675 F: +90-216-5000-676

United Arab Emirates:
NSK BEARINGS GULF TRADING CO.
DUBAI JAFZA View 19, Floor 24 Office LB192402/3, PO Box 262163, Downtown Jebel Ali,
Dubai, U.A.E
P: +971-(0)4-804-8200 F: +971-(0)4-884-7227

●North and South America

United States of America:
NSK AMERICAS, INC. (AMERICAN HEADQUARTERS)
ANN ARBOR 4200 Goss Road, Ann Arbor, Michigan 48105, U.S.A.
P: +1-734-913-7500 F: +1-734-913-7511

NSK CORPORATION
ANN ARBOR 4200 Goss Road, Ann Arbor, Michigan 48105, U.S.A.
P: +1-734-913-7500 F: +1-734-913-7511

NSK PRECISION AMERICA, INC.
FRANKLIN ☆ 3450 Bearing Drive, Franklin, Indiana 46131, U.S.A.
P: +1-317-738-5000 F: +1-317-738-5050
SAN JOSE 780 Montague Expressway, Suite 505, San Jose, California, 95131, U.S.A.
P: +1-408-944-9400 F: +1-408-944-9405

NSK LATIN AMERICA, INC.
MIAMI 11601 NW 107 Street, Suite 200, Miami Florida, 33178, U.S.A.
P: +1-305-477-0605 F: +1-305-477-0377

Canada:
NSK CANADA INC.
TORONTO ☆ 317 Rutherford Road South, Brampton, Ontario, L6W 3R5, Canada
P: +1-905-890-0740 F: +1-800-800-2788
MONTREAL 2150-32E Avenue Lachine, Quebec, Canada H8T 3H7
P: +1-514-633-1220 F: +1-800-800-2788

Argentina:
NSK ARGENTINA SRL
BUENOS AIRES Garcia del Rio 2477 Piso 7 Oficina "A" (1429) Buenos Aires-Argentina
P: +54-11-4704-5100 F: +54-11-4704-0033

Brazil:
NSK BRASIL LTDA.
SUZANO ☆ Av. Vereador Joao Batista Fitipaldi, 66, CEP 08685-000, Vila Maluf, Suzano, SP, Brazil
P: +55-11-4744-2500
JOINVILLE Rua Blumenau, 178-sala 910-Centro Joinville-SC, Brazil 89204-250
P: +55-47-3422-2239

Peru:
NSK PERU S.A.C.
LIMA Calle Teniente Enrique Palacios 360 Oficina 311 Miraflores, Lima, Peru
P: +51-493-4385

Mexico:
NSK RODAMIENTOS MEXICANA, S.A. DE C.V.
SILAO, GUANAJUATO Circuito Mexiamora Oriente No. 331, Parque Industrial Santa Fe I, Puerto
Interior. Silao, Guanajuato, Mexico. C.P. 36275
P: +52-472-103-9400 F: +52-472-103-9403

<As of December 2019>
For the latest information, please refer to the NSK website.
www.nsk.com

Motion & Control

No. 31 June 2020

Published by NSK Ltd.

Eco-awareness and reliability in motion

NSK

NSK used environmentally friendly printing methods for this publication.

CAT. No. ETJ-0031 2020 X-6 Printed in Japan